



THE UNIVERSITY *of* EDINBURGH

This thesis has been submitted in fulfilment of the requirements for a postgraduate degree (e.g. PhD, MPhil, DClinPsychol) at the University of Edinburgh. Please note the following terms and conditions of use:

- This work is protected by copyright and other intellectual property rights, which are retained by the thesis author, unless otherwise stated.
- A copy can be downloaded for personal non-commercial research or study, without prior permission or charge.
- This thesis cannot be reproduced or quoted extensively from without first obtaining permission in writing from the author.
- The content must not be changed in any way or sold commercially in any format or medium without the formal permission of the author.
- When referring to this work, full bibliographic details including the author, title, awarding institution and date of the thesis must be given.

Iterative Synthetic Aperture Radar Imaging Algorithms

Shaun I. Kelly

Doctor of Philosophy
University of Edinburgh
2014

Declaration

I declare that this thesis was composed by myself and that the work contained therein is my own, except where explicitly stated otherwise in the text. This work has not been submitted for any other degree or professional qualification.

The research on an iterative framework for synthetic aperture radar image formation in Chap. 3, was done in collaboration with Dr. Gabriel Rilling. This work forms part of the jointly-authored publication [80]. The research on autofocus algorithms for undersampled synthetic aperture radar in Chap. 4, was done in collaboration with Dr. Mehrdad Yaghoobi. This work also forms part of the jointly-authored publication [82].

(Shaun I. Kelly)

*Dedicated to my family and friends. In particular, my parents
(Hugh and Lisa) and Sarah.*

Abstract

Synthetic aperture radar is an important tool in a wide range of civilian and military imaging applications. This is primarily due to its ability to image in all weather conditions, during both the day and the night, unlike optical imaging systems. A synthetic aperture radar system contains a step which is not present in an optical imaging system, this is image formation. This is required because the acquired data from the radar sensor does not directly correspond to the image. Instead, to form an image, the system must solve an inverse problem. In conventional scenarios, this inverse problem is relatively straight forward and a matched filter based algorithm produces an image of suitable image quality. However, there are a number of interesting scenarios where this is not the case.

Scenarios where standard image formation algorithms are unsuitable include systems with data undersampling, errors in the system observation model and data that is corrupted by radio frequency interference. Image formation in these scenarios will form the topics of this thesis and a number of iterative algorithms are proposed to achieve image formation. The motivation for these proposed algorithms is primarily from the field of compressed sensing, which considers the recovery of signals with a low-dimensional structure.

The first contribution of this thesis is the development of fast algorithms for the system observation model and its adjoint. These algorithms are required by large-scale gradient based iterative algorithms for image formation. The proposed algorithms are based on existing fast back-projection algorithms, however, a new decimation strategy is proposed which is more suitable for some applications.

The second contribution is the development of a framework for iterative near-field image formation, which uses the proposed fast algorithms. It is shown that the framework can be used, in some scenarios, to improve the visual quality of images formed from fully sampled data and undersampled data, when compared to images formed using matched filter based algorithms.

The third contribution concerns errors in the system observation model. Algorithms that correct these errors are commonly referred to as autofocus algorithms. It is shown that conventional autofocus algorithms, which work as a post-processor on the formed image, are unsuitable for undersampled data. Instead an autofocus algorithm is proposed which corrects errors within the iterative image formation procedure. The proposed algorithm is provably stable and con-

vergent with a faster convergence rate than previous approaches.

The final contribution is an algorithm for ultra-wideband synthetic aperture radar image formation. Due to the large spectrum over which the ultra-wideband signal is transmitted, there is likely to be many other users operating within the same spectrum. These users can produce significant radio frequency interference which will corrupt the received data. The proposed algorithm uses knowledge of the RFI spectrum to minimise the effect of the RFI on the formed image.

Contents

Abstract	6
1 Introduction	23
1.1 Background	23
1.1.1 Synthetic Aperture Radar	24
1.1.2 Compressed Sensing and Sparse Reconstruction	28
1.2 Organisation	35
1.3 Contributions	35
1.4 Publications	36
2 Fast Synthetic Aperture Radar Image formation	39
2.1 Introduction	39
2.2 A Mathematical Model for Synthetic Aperture Radar	40
2.2.1 Propagation Model	41
2.2.2 Linear Frequency Modulated Chirped Radar	42
2.2.3 Dechirping	45
2.2.4 Deskewing	47
2.2.5 Continuous Observation Model	48
2.2.6 Phase History Sampling Requirements	50
2.2.7 Discrete Observation Model	52
2.3 Matched Filter based Image Formation	53
2.3.1 Back-projection Algorithm	54
2.3.2 Polar Format Algorithm	54
2.3.3 Fast Back-projection Algorithms	55
2.4 Summary	67
3 Iterative Image Formation	69
3.1 Introduction	69
3.2 Fast (Re/Back)-projection Algorithms	70
3.3 Pseudoinverse Image Formation	71

3.4	Sparsity based Iterative Image Formation	76
3.4.1	Image Properties	76
3.4.2	Image Model	77
3.4.3	Image Formation of Bright Image Elements	77
3.4.4	Image Formation of Background Image Elements	79
3.5	Experiments	79
3.6	Summary	82
4	Auto-focus	87
4.1	Introduction	87
4.2	Observation model with Phase Errors	88
4.3	Sparse Image Formation with Post-processing Autofocus	89
4.4	Uniqueness of Image Formation and Autofocus	91
4.5	Sparse Image Formation and Autofocus	92
4.5.1	Block Relaxation	93
4.6	Experimental Results	96
4.6.1	Quantitative Performance	96
4.6.2	Qualitative Performance	101
4.7	Summary	106
5	Ultra-Wideband Synthetic Aperture Radar	107
5.1	Introduction	107
5.2	Ultra-wideband Observational Model	108
5.2.1	Notched Linear Frequency Modulated Chirp on Transmit	108
5.2.2	Radio Frequency Interference	111
5.3	Linear Filter based RFI Suppression	113
5.4	RFI-aware Sparse Image Formation	114
5.5	Experiments	116
5.6	Summary	117
6	Conclusion and Future Work	121
6.1	Recommendations and Future Work	122
A	Synthetic Aperture Radar Simulator	125
A.1	Radio Frequency Transmission and Reception	125
A.2	Analogue Receiver	126
A.3	Timing Errors	127
A.4	Notched Linear Frequency Modulated Chirp	127
A.5	Radio Frequency Interference	128

A.6 Limitations of the Simulation	128
Bibliography	139

List of Figures

1.1	The main operational modes of SAR: (a) spotlight mode, (b) stripmap mode and (c) scan mode	26
2.1	RF wave propagation model: (a) incident field and (b) scattered field.	43
2.2	SAR antenna beam angles: (a) azimuth angles and (b) polar angles.	45
2.3	A time-frequency plot of a simulated received signal from three targets at the different stages of receiver processing. Where, $\omega_0/2\pi = 308$ MHz, $\alpha/\pi = 32.4$ MHz/ μ s and $T = 10$ μ s. (a) is the unprocessed received signal. (b) is the received signal after dechirping. (c) is the dechirped signal after deskewing.	49
2.4	Decomposition in the fast BP algorithms: (a) Decomposition in the decimation-in-phase-history algorithm and (b) Decomposition in the decimation-in-image algorithm.	55
2.5	Simulated phase history from four targets located at $[50, 50, 0]^T$ m, $[-50, 50, 0]^T$ m, $[50, -50, 0]^T$ m and $[-50, -50, 0]^T$ m (relative to the scene centre). The system parameter are: carrier frequency $\omega_0/2\pi = 308$ MHz, chirp rate $\alpha/\pi = 32.4$ MHz/ μ s, chirp period $T = 10$ μ s, synthetic aperture $[7, -3.5, 7]^T$ km to $[7, 3.5, 7]^T$ km (relative to the scene centre) and platform velocity 100 m/s. (a) is the phase history in the fast time and the slow time. (b) is the phase history in the fast time spectrum and the slow time. (c) is the phase history in the fast time and slow time spectrum. (d) is the phase history in fast time spectrum and slow time spectrum.	61

- 2.6 Simulated phase history from four targets located at $[25, 25, 0]^T$ m, $[-25, 25, 0]^T$ m, $[25, -25, 0]^T$ m and $[-25, -25, 0]^T$ m (relative to the scene centre). The system parameter are: carrier frequency $\omega_0/2\pi = 308$ MHz, chirp rate $\alpha/\pi = 32.4$ MHz/ μ s, chirp period $T = 10$ μ s, synthetic aperture $[7, -3.5, 7]^T$ km to $[7, 3.5, 7]^T$ km (relative to the scene centre) and platform velocity 100 m/s. (a) is the phase history in the fast time and the slow time. (b) is the phase history in the fast time spectrum and the slow time. (c) is the phase history in the fast time and slow time spectrum. (d) is the phase history in fast time spectrum and slow time spectrum. 62
- 2.7 Images formed using the BP algorithm from a simulated phase history which was generated using four targets located at $[25, 25, 0]^T$ m, $[-25, 25, 0]^T$ m, $[25, -25, 0]^T$ m and $[-25, -25, 0]^T$ m (relative to the scene centre). The system parameter are: carrier frequency $\omega_0/2\pi = 308$ MHz, chirp rate $\alpha/\pi = 32.4$ MHz/ μ s, chirp period $T = 10$ μ s, synthetic aperture $[7, -3.5, 7]^T$ km to $[7, 3.5, 7]^T$ km (relative to the scene centre) and platform velocity 100 m/s. (a) is the resulting image and (b) is its spectrum. (c), (d), (e) and (f) are the spectra of images formed using four evenly sized segments of the full phase history. 63
- 2.8 Images formed using the HH polarisation with angles $1 - 4^\circ$ of the eighth pass of the Gotcha data set. The images contain 768×768 pixels. The antenna beamwidths were limited to a 1.15° azimuth angle and a 0.57° polar angle. (a) was formed using the BP algorithm and (b) is its wavenumber spectrum. (c) was formed using the fast decimation-in-phase-history BP algorithm with one decomposition stage. (d) was formed using the fast decimation-in-image BP algorithm with one decomposition stage. (e) was formed using the fast decimation-in-phase-history BP algorithm with three decomposition stages. (f) was formed using the fast decimation-in-image BP algorithm with three decomposition stages. 65
- 2.9 Relative errors in the Fast BP algorithms with respect to the BP algorithm. (a) is the relative error in the image in Fig. 2.8(d). (b) is the relative error in the wavenumber spectrum of the image in Fig. 2.8(c). (c) is the relative error in the image in Fig. 2.8(f). (d) is the relative error in the wavenumber spectrum of the image in Fig. 2.8(e). 66

- 3.1 Images formed using a simulated phase history which was generated using four targets located at $[500, 500, 0]^T$ m, $[-500, 500, 0]^T$ m, $[500, -500, 0]^T$ m and $[-500, -500, 0]^T$ m (relative to the scene centre). The system parameter are: carrier frequency $\omega_0/2\pi = 308$ MHz, chirp rate $\alpha/\pi = 32.4$ MHz/ μ s, chirp period $T = 10$ μ s, synthetic aperture $[7, -3.5, 7]^T$ km to $[7, 3.5, 7]^T$ km (relative to the scene centre). (a) Image formed using the filtered BP Algorithm. (b) Image formed using the filtered PFA Algorithm. (c) Zoomed image in (a). (d) Zoomed image in (b). (e) wavenumber spectrum of image in (a). (f) wavenumber spectrum of image in (b). 72
- 3.2 Images formed using a simulated phase history which was generated using four targets located at $[25, 25, 91.16]^T$ m, $[-25, 25, 91.16]^T$ m, $[25, -25, 91.16]^T$ m and $[-25, -25, 91.16]^T$ m (relative to the scene centre). The system parameter are: carrier frequency $\omega_0/2\pi = 308$ MHz, chirp rate $\alpha/\pi = 32.4$ MHz/ μ s, chirp period $T = 10$ μ s, synthetic aperture $[7, -3.5, 7]^T$ km to $[7, 3.5, 7]^T$ km (relative to the scene centre). (b) Image formed using the filtered BP algorithm without elevation knowledge. (a) Image formed using the filtered BP algorithm with elevation knowledge. 73
- 3.3 Images formed using a simulated phase history which was generated using four targets located at $[25, 25, 0]^T$ m, $[-25, 25, 0]^T$ m, $[25, -25, 0]^T$ m and $[-25, -25, 0]^T$ m (relative to the scene centre). The system parameter are: carrier frequency $\omega_0/2\pi = 308$ MHz, chirp rate $\alpha/\pi = 32.4$ MHz/ μ s, chirp period $T = 10$ μ s, synthetic aperture $[7, -3.5, 7]^T$ km to $[7, 3.5, 7]^T$ km (relative to the scene centre). (a) Image formed using the BP algorithm. (b) Image formed using the filtered BP algorithm. 74
- 3.4 Images formed using a simulated phase history which was generated using four targets located at $[25, 25, 0]^T$ m, $[-25, 25, 0]^T$ m, $[25, -25, 0]^T$ m and $[-25, -25, 0]^T$ m (relative to the scene centre). The system parameter are: carrier frequency $\omega_0/2\pi = 10$ GHz, chirp rate $\alpha/\pi = 32.4$ MHz/ μ s, chirp period $T = 10$ μ s, synthetic aperture random locations between $[7, -0.3, 7]^T$ km to $[7, 0.3, 7]^T$ km (relative to the scene centre). (a) Image formed using the filtered BP algorithm (b) Image formed using the LSQR algorithm. 75

3.5	Images formed using a simulated phase history which was generated using four targets located at $[25, 25, 0]^T$ m, $[-25, 25, 0]^T$ m, $[25, -25, 0]^T$ m and $[-25, -25, 0]^T$ m (relative to the scene centre). The system parameter are: carrier frequency $\omega_0/2\pi = 308$ MHz, chirp rate $\alpha/\pi = 32.4$ MHz/ μ s, chirp period $T = 10$ μ s, synthetic aperture $[7, -3.5, 7]^T$ km to $[7, 3.5, 7]^T$ km (relative to the scene centre). Images were formed using the FISTA based sparse image formation. (a) Image with full spectral support. (b) Image with projected spectral support. (c) Zoomed image of (a). (d) Zoomed image of (b). (e) Wavenumber spectrum of image in (a). (f) Wavenumber spectrum of image in (b).	80
3.6	Image formed using the HH polarisation with the angles $1 - 4^\circ$ of the eighth pass of the Gotcha data set. The images contain 768×768 pixels. The antenna beamwidths were limited to a 1.15° azimuth angle and a 0.57° polar angle. Image was formed using the filtered BP algorithm	82
3.7	Images formed using the HH polarisation with the angles $1 - 4^\circ$ of the eighth pass of the Gotcha data set with cross-range undersampling. The images contain 768×768 pixels. The antenna beamwidths were limited to a 1.15° azimuth angle and a 0.57° polar angle. (b), (d) and (f) were formed using a random 75% subset of the phase history cross-range samples. (a), (c) and (e) were formed using a random 50% subset of the phase history cross-range samples. (b) and (a) were formed using the filtered BP algorithm. (d) and (c) were formed using the FISTA based sparse image formation. (f) and (e) were formed using the IHT based sparse image formation	83
3.8	Images formed using the HH polarisation with the angles $1 - 4^\circ$ of the eighth pass of the Gotcha data set with range undersampling. The images contain 768×768 pixels. The antenna beamwidths were limited to a 1.15° azimuth angle and a 0.57° polar angle. (b), (d) and (f) were formed using a random 75% subset of the phase history range samples. (a), (c) and (e) were formed using a random 50% subset of the phase history range samples. (b) and (a) were formed using the filtered BP algorithm. (d) and (c) were formed using the FISTA based sparse image formation. (f) and (e) were formed using the IHT based sparse image formation	84
4.1	Comparison of empirical convergence rates. (a) '□' Algorithm 3 and '×' Algorithm 4. (b) '□' Algorithm 4 with continuation and '×' Algorithm 4.	97
4.2	Phase error induced filters (the rows of Ψ for quadratic and random phase errors with different γ). Quadratic: (a) $\gamma = 0.1$ (c) $\gamma = 1$ (e) $\gamma = 10$. Random: (b) $\gamma = 0.1$ (d) $\gamma = 1$ (f) $\gamma = 10$	99

4.3	Image formation performance performance versus undersampling ratio: ‘o’ oracle image formation, ‘□’ Algorithm 4 and ‘×’ sparse image formation and post-processing autofocus with reference phase errors. Quadratic: (a) $\gamma = 0.1$ (c) $\gamma = 1$ (e) $\gamma = 10$. Random: (b) $\gamma = 0.1$ (d) $\gamma = 1$ (f) $\gamma = 10$	100
4.4	Power spectral density of notched linear frequency chirp.	102
4.5	UWB SAR image formations: (a) was formed using filtered BP algorithm, (c) was formed using an ℓ_1 -norm SPG method and (e) was formed using Algorithm 4. (b), (d) and (f) are a zoomed in view of (a), (c) and (e) around the origin, respectively.	104
4.6	Multifunction SAR image formations: (a) was formed using filtered BP algorithm, (c) was formed using an ℓ_1 -norm SPG method and (e) was formed using Algorithm 4. (b), (d) and (f) are a zoomed in view of (a), (c) and (e) around the origin, respectively.	105
5.1	Transmitter notching of LFM chirp.	109
5.2	Spectrum and range ambiguity function of LFM and notched LFM chirp. The parameter for the LFM chirp are: centre frequency is 308 MHz, the chirp bandwidth is 324 MHz, the chirp period is 10 μ s. The parameters for the notches are: the notch centre frequencies of the notches are 175, 330, 389, 416 and 448 MHz, the notch bandwidths are 15, 7, 13, 20 and 10 MHz. (a) is the spectrum of the LFM chirp signal. (b) is the range ambiguity function of the LFM chirp signal. (c) is the spectrum of the notch LFM chirp signal. (d) is the range ambiguity function of the notched LFM chirp signal.	110
5.3	Range returns from three targets with a notched LFM chirp before and after dechirping and deskewing. The parameter for the LFM chirp are: centre frequency is 308 MHz, the chirp bandwidth is 324 MHz, the chirp period is 10 μ s. The parameters for the notches are: the notch centre frequencies of the notches are 175, 330, 389, 416 and 448 MHz, the notch bandwidths are 15, 7, 13, 20 and 10 MHz. Targets are located at 0, +400 and -400 m (relative to the centre of the scene). (a) is a spectrogram of the received signal before dechirping and deskewing. (b) is a spectrogram of the received signal after dechirping and deskewing. (c) is the spectrum of the received signal from just the target at 0 m after dechirping and deskewing.	112

5.4	Range returns from three targets with a LFM chirp and five RF interferers, before and after dechirping and deskewing. The parameter for the LFM chirp are: centre frequency is 308 MHz, the chirp bandwidth is 324 MHz, the chirp period is 10 μ s. Targets are located at 0, +400 and -400 m (relative to the centre of the scene). RF interferers at 208, 258, 308, 358 and 408 MHz. (a) is a spectrogram of the received signal before dechirping and deskewing. (b) is a spectrogram of the received signal after dechirping and deskewing.	113
5.5	SAR images formed from simulated phase histories with RFI: (a) fast BP algorithm with no RFI suppression, (b) Wiener filtered followed by the BP algorithm, (c) RFI-aware sparse image formation and (d) range compression RFI-aware sparse image formation.	118
5.6	CFAR detections in red: (a) BP with no RFI suppression, (b) Wiener filtered followed BP, (c) RFI-aware sparse image formation, (d) range compression RFI-aware sparse image formation.	119

List of Tables

2.1	Image formation times (seconds)	64
3.1	LSQR image formation times (seconds)	81
3.2	FISTA image formation times (seconds)	81
4.1	System parameters for synthetic experiments	96
4.2	Continuation parameters	97
4.3	System parameters for simulated UWB SAR	102
4.4	System parameters for simulated multifunction SAR	103
5.1	System parameters for simulated UWB SAR	117
A.1	Transmission and reception simulation parameters	126
A.2	Receiver simulation parameters	126
A.3	Notched LFM parameters	127
A.4	RFI parameters	128

Nomenclature

Acronyms and Abbreviations

ADC analog-to-digital converter

AM amplitude modulation

BP back-projection

BPDN basis pursuit denoising

CFAR constant false alarm rate

CS compressed sensing

CT computed tomography

DEM digital elevation model

DFT discrete Fourier transform

FFT fast Fourier transform

FHA Fourier-Hankel algorithm

FISTA fast iterative shrinkage-thresholding algorithm

FM frequency modulation

FMM fast multipole method

GPU graphics processing unit

IDFT inverse discrete Fourier transform

IF intermediate frequency

IHT iterative hard thresholding

LASSO least absolute shrinkage and selection operator

LFM linear frequency modulated

LHS	left-hand side
LS	least squares
LSQR	least squares QR
MCA	multichannel autofocus
MD	map drift
MMSE	minimum mean square error
NFFT	non-uniform fast Fourier transform
NSP	null space property
PDE	partial differential equation
PFA	polar format algorithm
PGA	phase gradient autofocus
PPI	plan position indicator
PRF	pulse repetition frequency
PSD	power spectral density
RCMC	range cell migration correction
RDA	range-Doppler algorithm
RF	radio frequency
RFI	radio frequency interference
RHS	right-hand side
RIP	restricted isometry property
RMA	range migration algorithm
RVP	residual video phase
SAR	synthetic aperture radar
SAS	synthetic aperture sonar
SNR	signal-to-noise ratio
SPG	spectral projected gradient

SR sparse reconstruction

TV total variation

UHF ultra high frequency

UWB ultra-wideband

VHF very high frequency

Symbols

$\#$ cardinality of a set

$|\cdot|$ absolute value

\approx approximately equal

$*$ convolution

$(\cdot)^\dagger$ pseudoinverse

$(\cdot)^H$ conjugate transpose

$(\cdot)^T$ transpose

$\cdot, (\cdot)$ operand

\circ element-wise Hadamard matrix product

$\text{diag}(\mathbf{x})$ diagonal matrix with the elements of a vector \mathbf{x} on the main diagonal

$\frac{\partial}{\partial t}$ partial derivative with respect to t

$\langle \mathbf{x}, \mathbf{y} \rangle$ inner product of vectors \mathbf{x} and \mathbf{y}

$\langle \mathbf{x}, \mathbf{y} \rangle_{\mathbf{Q}}$ inner product of vectors \mathbf{x} and $\mathbf{Q}\mathbf{y}$, where, \mathbf{Q} is a positive-definite matrix

\mathcal{S}^c the complement of a set \mathcal{S}

$\nabla \cdot$ divergence operator

$\nabla \times$ curl operator

∇^2 Laplace operator

$\|\cdot\|_0$ $\|\mathbf{x}\|_0 = \# \{i, x_i \neq 0\}$, $\|\mathbf{X}\|_0 = \# \{(i, j), x_{i,j} \neq 0\}$

$\|\cdot\|_\infty$ $\|\mathbf{x}\|_\infty = \max_i \{|x_i|\}$, $\|\mathbf{X}\|_\infty = \max_{i,j} \{|x_{i,j}|\}$

$\|\cdot\|_p$ $\|\mathbf{x}\|_p = (\sum_i |x_i|^p)^{1/p}$, $\|\mathbf{X}\|_p = \left(\sum_{i,j} |x_{i,j}|^p\right)^{1/p}$, $p > 0$

$$\|\cdot\|_F \quad \|\mathbf{X}\|_F = \left(\sum_{i,j} x_{i,j}^2 \right)^{1/2}$$

$$\|h(\cdot)\| \quad \max \{ \|h(\mathbf{X})\|_F, \|\mathbf{X}\|_F = 1 \}$$

$$\text{vec}(\mathbf{X}) \quad \text{vectorise } \mathbf{X} \in \mathbb{C}^{M \times N} \text{ to } \mathbf{x} \in \mathbb{C}^{MN} \text{ by vertically stacking the columns of } \mathbf{X}$$

$$\text{tr}(\cdot) \quad \text{trace of a matrix}$$

$$\vec{\mathbf{x}} = [x_1, x_2, x_3]^T \quad \text{vector of three Cartesian Coordinates}$$

$$\mathbf{0}_{M,N} \quad \text{zero matrix of size } M \times N$$

$$\mathbf{x}^{(i)} \quad i\text{th row of a matrix } \mathbf{X}$$

$$\mathbf{x}_i \quad i\text{th column of a matrix } \mathbf{X}$$

$$\mathbf{x}_{\mathcal{S}} \quad \text{the projection of } \mathbf{x} \text{ onto the set } \mathcal{S}$$

$$x_i \quad i\text{th element of a vector } \mathbf{x}$$

$$x_{i,j} \quad \text{element in the } i\text{th row and } j\text{th column of a matrix } \mathbf{X}$$

$$\delta(\cdot) \quad \text{delta Dirac function}$$

$$\mathcal{N}(\mu, \sigma^2) \quad \text{Gaussian distribution with a mean } \mu \text{ and a variance } \sigma^2$$

$$\mathcal{O}(\cdot) \quad \text{big O notation}$$

$$\mathcal{U}(a, b) \quad \text{uniform distribution between } a \text{ and } b$$

$$N(\cdot) \quad N(\mathbf{A}) = \{\mathbf{x} : \mathbf{A}\mathbf{x} = 0\} \text{ right null space of a matrix } \mathbf{A}, N(h(\cdot)) = \{\mathbf{X} : h(\mathbf{X}) = 0\} \text{ right null space of a linear map } h(\cdot)$$

Chapter 1

Introduction

1.1 Background

Radar is an acronym for “radio detection and ranging”. The acronym refers to the application for which radar was originally developed, which is the detection and location of objects using radio waves. Since its initial development, radar technology has been applied to a vast array of military and civilian applications. These applications include: weather-sensing, navigation, terrain mapping and imaging. Radar remains a critical sensing modality because it can function during both the day and the night and in all-weather conditions unlike passive optical-based systems.

This thesis will concentrate on one important application of radar, which is imaging. Imaging radar systems are used to approximate the reflectivity of the elements in a scene of interest. More specifically, in this thesis, the focus will be on a type of imaging radar known as synthetic aperture radar (SAR). SAR is an extremely versatile form of imaging radar which can produce high-resolution images without a large physical antenna aperture. SAR systems generate two-dimensional (possibly three-dimensional) images from a collection of data which is one-dimensional (range-only). This range-only data is collected from spatially separated locations along a *synthetic aperture*. The complete collection of data is commonly referred to as a *phase history*.

The procedure of forming an image from a phase history typically involves the application of a series of linear operations. These operations approximate a matched filter. Matched filter based approaches produce excellent images for most SAR applications, however, there are a number of emerging applications of SAR where such methods do not perform so well. This can be due to interrupted sampling along the synthetic aperture, spectral notches in the radar signal, uncertainty in observation model or radio frequency interference. In these scenarios a solution to the problem of producing an image from a phase history may require some form of *iterative* method. These emerging applications of SAR and the development of iterative image

formation algorithms will be the focus of this thesis.

The proceeding sections of this chapter will describe an overview of SAR and its various forms of operation, in particular, those applications that will be consider in this thesis. There is also a review of compressed sensing (CS) and sparse reconstruction (SR) theory. This theory will be used extensively throughout this thesis to motivate and guide the development of iterative image formation algorithms.

1.1.1 Synthetic Aperture Radar

The SAR imaging methodology was first developed in the 1950s and later appear in the open literature in the 1960s [118, 19]. It was developed as a more effective means of producing radar images than *real-aperture* imaging methods.

In real-aperture radar systems, an antenna with a large cross-range aperture is used to produced an antenna *footprint* with a narrow beamwidth. This narrow footprint is scanned along the scene of interest and an image is formed using knowledge of the beam locations and their corresponding one-dimensional range profiles. Real-aperture systems are sometimes used in air traffic control and ship navigation. In these systems the narrow beam is rotated in a circle around the radar antenna and the real-aperture image is displayed in polar co-ordinates on a plan position indicator (PPI). The problem with real-aperture systems is that the cross-range resolution of the resulting image is entirely dependent on the antenna footprint. Therefore, to produce a high cross-range resolution image, a large (often unfeasibly large) physical antenna is required.

Unlike a real-aperture imaging system, a SAR system does not require a large cross-range antenna aperture in order to produce a high cross-range resolution image. It instead uses a smaller physical aperture antenna mounted to a moving *platform* (typically an aircraft or a satellite) to synthesise a larger aperture. Also, in SAR, unlike real-aperture systems, the cross-range resolution is independent of range.

There are three main modes of operation for SAR systems: stripmap, spotlight and scan. Each mode differs in the way they synthesise an aperture. Each of these three modes of operation are illustrated in Fig. 1.1.

Stripmap Mode SAR The first mode of SAR which was developed, was the stripmap mode. In this mode the antenna footprint is swept along a scene of interest with a fixed antenna beam direction relative to the platform velocity. This makes the synthetic aperture length dependent on the cross-range antenna beamwidth. This is because the beamwidth determines the length of the synthetic aperture for which any target in the scene is contained with in the antenna's footprint. Interestingly this means, for a stripmap mode system, the smaller the antenna the higher cross-range resolution, which is the opposite case to a real-aperture imaging system. It

is natural to use stripmap mode SAR to image a scene which consists of a long strip of terrain, therefore, it is efficient at imaging large regions with a relatively coarse-resolution.

Spotlight Mode SAR In the 1970s the spotlight mode of SAR was developed [134]. In spotlight mode the antenna beam is steered such that the antenna footprint on the ground illuminates the same scene of interest at all platform locations. Spotlight mode SAR can be used to create an image with a higher cross-range resolution, with the same physical antenna, as that which would be achievable in the stripmap mode. This is because in spotlight mode SAR the synthetic aperture length is not dependent on the antenna beamwidth, instead, the cross-resolution continues to improve with an increasing synthetic aperture length. Spotlight mode avoids limitations on the synthetic aperture length because the antenna is steered such that the antenna footprint always contains the scatterers in the scene of interest at all platform positions.

Spotlight mode is a flexible mode which can be used to image a single scene or multiple scenes at a number of different viewing angles during a single pass. This is possible because the SAR platform usually travels a longer distance than the synthetic aperture length which is required to achieve the desired cross-range resolution. Therefore, the platform motion is in excess of the required synthetic aperture length and this excess platform motion can be used to generate additional images of a single scene or to image multiple scenes. If the system images a single scene from multiple viewing angles, the multiple images can be used to determine the scattering properties of targets that vary with observation angle. This additional scattering information could be used to improve target detection and identification. It may also be useful to use the excess platform motion to image multiple scenes of interest at a high resolution.

Scan Mode SAR

Scan mode SAR can be seen as a generalisation of the other two modes of SAR. It can be used to trade off the benefits of the stripmap and spotlight modes. These benefits are the imaging of large regions and imaging with high cross-range resolution. In scan mode the antenna is steered such that the antenna footprint illuminates a strip or multiple strips of terrain at an angle relative to the platform motion. Scan mode is usually more complex, operationally and in terms of its processing, than spotlight and stripmap modes and is therefore less commonly used than the other two modes of SAR.

Standard SAR Image Formation

The majority of SAR image formation algorithms, for all modes of SAR, can be considered to be an approximation of a two-dimensional matched filter, where each pixel in the resulting image is the result of a correlation of the phase history with the expected signal for a target at that location.

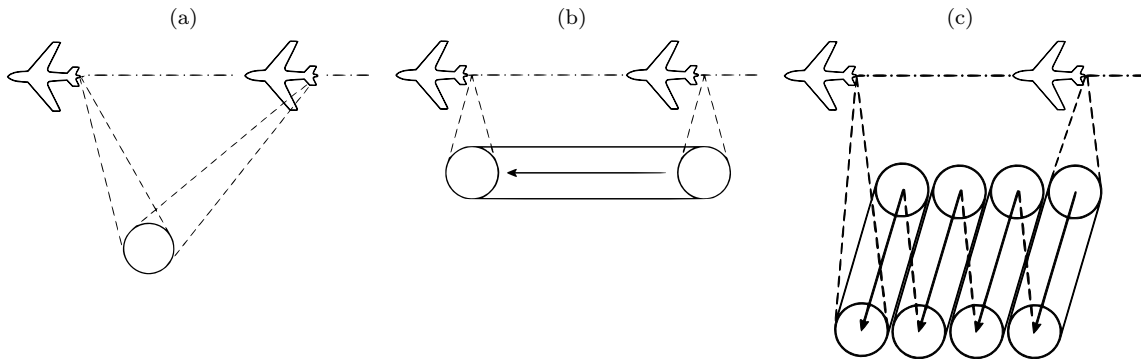


Figure 1.1: The main operational modes of SAR: (a) spotlight mode, (b) stripmap mode and (c) scan mode

For stripmap mode, arguably the most commonly used algorithm for image formation is the range-Doppler algorithm (RDA) [97]. The basic components of the RDA are *range compression*, *range cell migration correction (RCMC)* and *cross-range compression*¹. RCMC is required so that the matched filtering can be performed separately in range and cross-range. While the RDA is only suitable for far-field scenes, there are also algorithms for image formation which more accurately approximate a two-dimensional matched filter and can be used with a near-field scene. They include the range migration algorithm (RMA) [21, 112, 93], the Fourier-Hankel algorithm (FHA) [60, 71, 5] and the chirp scaling algorithm [109]. In these algorithms the matched filtering is *not* performed separately in range and cross-range.

For the spotlight mode, the most commonly used image formation algorithm is the polar format algorithm (PFA) [134]. The PFA uses the near-field scene approximation to simplify the two-dimensional matched filter to a two-dimensional discrete Fourier transform (DFT) from polar to Cartesian co-ordinates. This has been traditionally achieved, in a computationally efficient manner, by using zero-padded FFTs and separable one-dimensional polynomial interpolation. More recently, computationally efficient algorithms have been proposed for two-dimensional non-uniform FFTs (NFFT) [54, 68, 62]. These algorithms can compute DFTs from a uniform to an arbitrary grid and vice versa with the same order of complexity as a standard FFT algorithm. These algorithms can be used to compute the PFA with high accuracy [61, 4]. The most accurate approximation to the true matched filter solution is achieved by what are sometimes called *time-domain* algorithms or *back-projection* (BP) algorithms, named due to their close relation to the BP algorithms in computed tomography (CT) [96]. It should be noted that the spotlight mode image formation algorithms can also be used for the stripmap mode with some preprocessing. Also if the aperture is linear, then the stripmap mode algorithms can be used for the spotlight mode with some preprocessing.

Although the matched filter is the optimal linear algorithm for maximising the signal-to-

¹“Compression” in the radar literature, refers to what is known as matched filtering in the signal processing field.

noise ratio (SNR) for a single target in the presence of additive white Gaussian noise, it is not optimal for image formation [58]. This is because a SAR image will contain many targets and the matched filter is only optimal for one. For this reason, the phase history is sometimes *filtered* before applying a matched filter type algorithm, in order to maximise the SNR for all the targets in the image. This filtering usually involves applying weights to the phase history.

Non-standard SAR Systems

There are a number of non-standard SAR scenarios in which standard SAR image formation algorithms provide insufficient image quality. One such scenario is the case of phase history undersampling. The missing data in an undersampled phase history can take various forms, which include:

- *Missing locations along the synthetic aperture.* This corresponds to temporary interruptions in the acquisition of SAR data during the platform motion. This type of interruption typically occurs when the radar antenna is needed for multiple tasks. For example, the system is collecting SAR data from multiple ground patches (as in scan mode) or multiple polarisations and cannot always maintain the required pulse repetition frequency (PRF) or the system is passively sensing the air space (which is useful in a military context) [116, 131, 124].
- *Missing frequency bands in the spectrum of the radar signal.* This type of missing data occurs in ultra-wideband (UWB) SAR, where the spectrum of the transmitted signal contains sub-bands where transmission is not allowed [48, 42, 87]. This usually occurs when operating in the very high frequency (VHF) and the ultra high frequency (UHF) spectra. In order to be able to operate a SAR system within these spectra, spectral notches must be added to the transmitted signal to avoid the specified sub-bands.
- *Arbitrary missing data.* This will occur when samples are discarded from the acquired data to reduce the amount of data stored on the acquisition platform. This may be done in order to achieve a small amount of compression of the data. This may be useful on some platforms, such as satellites, which have only a small amount of computational resources or which have low storage capacities [14, 110].

When there is data undersampling, standard image formation algorithms will produce large target sidelobes in the image.

Another scenario where non-standard methods are required is when there are significant errors in the system observation model. To reconstruct a SAR image, knowledge of the acquisition system is required. Such knowledge of a system cannot be perfectly known in practical situations. Imperfect knowledge can result in errors that are perceived as phase errors in the phase history. If they are not corrected, these phase errors can severely degrade the image

quality. Methods for correcting these errors in a fully-sampled system are known as autofocus algorithms. These methods are most commonly used as a post-processing method on the degraded image [132, 94, 76, 29]. Post-processing autofocus algorithms are successful at correcting phase errors in fully-sampled scenarios, however, they may not be suitable for undersampled SAR.

The last scenario that will be described also occurs in UWB SAR systems. In the VHF/UHF spectrum, even within the bands where transmission is allowed, strong interference from other users, particularly from narrow-band (amplitude modulation (AM) and frequency modulation (FM)) transmitters, can deteriorate the dynamic range of the resulting SAR image. To achieve a reasonable level of performance, a SAR system must include a method of radio frequency interference (RFI) suppression. Unfortunately, RFI suppression will degrade an image formed using a standard algorithm by introducing range sidelobes [87, 86, 79, 1, 66].

1.1.2 Compressed Sensing and Sparse Reconstruction

The theory of CS and SR provides a theoretical framework which suggests it is possible to reconstruct some signals from a smaller number of linear measurements than suggested by conventional sampling theory.

The conventional approach to sampling signals is based around the Nyquist-Shannon sampling theorem. This theorem states that the sampling rate for real-valued signals must be at least twice as large as the highest frequency present in the signal. This theory can also be extended to many *real world* signals that do not have a highest frequency, e.g. images. For these signals the standard practise is to use a low-pass filter, also known as an anti-aliasing filter, on the signal before sampling. For this type of signal, the resolution of the sampled signal will be determined by the bandwidth of the filter.

During the middle of the first decade of the twenty first century the theory of CS was developed, largely motivated by the perceived inefficiencies in many conventional sampling systems [24, 50, 27, 25]. In many sampling systems, a large amount of signal data are acquired, however, a compression stage which follows the data acquisition discards a significant proportion of these data. This leads to the question, “is it possible to combine the signal acquisition and compression stages and only acquire the critical information about the signal, in just a small amount of data?”. CS theory answers this question in the affirmative.

Some problems which are not strictly a CS problem are closely related. One such problem, will be referred to as a SR problem. In a SR problem, the goal is to recover a signal from a fixed sampling system, where the inversion from a conventional perspective is ill-posed. Prior knowledge about the compressibility of the signal is used to make the inversion problem well-posed. Much of the theory of CS is equally applicable to SR problems, where it can be used to determine when a SR problem is likely to be well-posed.

There are a number of good tutorial style article on CS. They include [28] and [114]. In this section, the key concepts and theoretical results of the CS literature will be provided.

The Sensing Problem

A discrete sampling of a linear observation system is considered. Such a system can be written mathematically as

$$y_m = \langle \phi_m, \mathbf{x} \rangle, \quad m = 1, \dots, M. \quad (1.1)$$

This equation states that M samples of a signal \mathbf{x} are acquired by taking M inner products with the sensing vectors $\{\phi_1, \dots, \phi_M\}$. Most commonly the signal is continuous, therefore, \mathbf{x} and ϕ_m are infinite dimensional vectors. Some common examples of sensing vectors are translated Dirac delta functions, translated indicators functions or sinusoids.

Instead of considering continuous-time/space signals, it is usually more convenient to consider discrete signals, therefore, $\mathbf{x} \in \mathbb{R}^N$ and $\phi_m \in \mathbb{R}^N$ are finite vectors. The reason for this choice is because the CS theory for discrete signals is simpler and more developed than the theory for continuous signals. Also, the discrete theory still provides important insights and tools that can be extended to the continuous domain. It should also be noted that most of the CS literature addresses real-valued signals, however, the results which will be given in the following section are equally extendable to complex signals with slightly modified constants [27].

A discrete linear observation system can be written as

$$\mathbf{y} = \Phi \mathbf{x}, \quad (1.2)$$

where, $\mathbf{y} \in \mathbb{R}^M$ are the measurements, $\mathbf{x} \in \mathbb{R}^N$ is the signal and $\Phi \in \mathbb{R}^{M \times N}$ is the sensing matrix with the vectors $\{\phi_1^H, \dots, \phi_M^H\}$ as its rows.

CS addresses the undersampling problem where the number of measurements M is much smaller than the dimension N of the signal. In this scenario, the linear system is under-determined and without additional information there are infinitely many feasible signals $\hat{\mathbf{x}}$ that match the observed measurements, i.e. $\mathbf{y} = \Phi \hat{\mathbf{x}}$. In CS, this further information commonly comes in the form of a sparse signal model and is used to select a unique solution $\hat{\mathbf{x}}$ from all the feasible solutions.

Sparse/Compressible Signal Model

Sparsity expresses the idea that a signal can be represented using a small number of coefficients in a particular basis. To express this concept mathematically, first observe that any signal \mathbf{x} can be uniquely represented in a basis $[\psi_1, \dots, \psi_N]$, e.g. a wavelet basis, with the sum

$$\mathbf{x} = \sum_{n=1}^N \alpha_n \psi_n, \quad (1.3)$$

where, $\boldsymbol{\alpha} \in \mathbb{R}^N$ is the coefficient vector. If the signal is *sparse* in the selected basis, then only $K < N$ elements of $\boldsymbol{\alpha}$ will be non-zero. The set of all K -sparse coefficient vectors is defined as

$$\Sigma_K = \{\boldsymbol{\alpha} \in \mathbb{R}^N : \|\boldsymbol{\alpha}\|_0 \leq K\}. \quad (1.4)$$

In practice, most signals do not have *exact sparse* representations, instead, they are only *well approximated* by a sparse signal. Such signals are referred to as *compressible signals*. An example of a compressible signal is an image. Images can be well approximated by a sparse signal in a wavelet basis.

To give a mathematical definition of a compressible signal, it is convenient to define the best K -sparse approximation $\boldsymbol{\alpha}_K$ of a coefficient vector $\boldsymbol{\alpha}$. The best K -sparse approximation is the vector within Σ_K that minimises $\|\boldsymbol{\alpha} - \boldsymbol{\alpha}_K\|_p$. For all ℓ_p norms, $\boldsymbol{\alpha}_K$ can be computed by thresholding all but the K largest magnitude elements of $\boldsymbol{\alpha}$ [46]. For compressible signals the distance between the signal and its best K -sparse approximation will decrease rapidly as K increases. A mathematical definition of a compressible signal is frequently given as any signal whose coefficients vector, with elements sorted in decreasing order, satisfies the inequality

$$|\alpha_k| \leq C_0 k^{-C_1}, \quad (1.5)$$

where C_0 and C_1 are positive real constants.

The knowledge that a signal is sparse, in particular orthogonal basis, changes the inversion problem. If an orthogonal basis expansion of a sparse signal is included, the system model becomes

$$\mathbf{y} = \boldsymbol{\Phi} \boldsymbol{\Psi} \boldsymbol{\alpha} = \mathbf{A} \boldsymbol{\alpha}, \quad (1.6)$$

where, $\boldsymbol{\Psi} \in \mathbb{R}^{N \times N}$ contains the basis vectors $\{\psi_1^H, \dots, \psi_N^H\}$ as its rows. Now, instead of considering whether $\boldsymbol{\Phi}$ embeds N -dimensional signals in the measurements, one instead considers the embedding of K -sparse signals in these same measurements.

Sensing Matrices

In CS it is important to understand which classes of sensing matrices preserve the information of sparse signals and whether they allow these sparse signals to be recovered by tractable algorithms. The properties of classes of matrices are usually studied in terms of key desirable properties. One of the most fundamental matrix properties, required for the unique embedding of sparse signals in the measurements, is known as the *spark* [51].

Definition 1.1.1. *The spark of a matrix \mathbf{A} is equal to the smallest number of columns of \mathbf{A} that are linearly dependent.*

With this definition, the following theorem provides a necessary and sufficient condition, in terms of the spark of a \mathbf{A} , for which sparse signals are uniquely embedded in the measurements.

Theorem 1.1.2 ([51, Corollary 1]). *If and only if the spark $\{\mathbf{A}\} > 2K$ then for any vector $\mathbf{y} \in \mathbb{R}^M$, there exists at most one signal $\boldsymbol{\alpha} \in \Sigma_K$ such that $\mathbf{y} = \mathbf{A}\boldsymbol{\alpha}$.*

The spark condition is suitable for the exact sparse problem, however, for the problem of recovering approximately sparse signals a more restrictive property is required. One such property is known as the null space property (NSP). Informally, it requires that signals that lie in the null space of \mathbf{A} do not have most of their signal energy concentrated in a small number of their elements.

Definition 1.1.3. *A matrix \mathbf{A} has the mixed NSP in (p, q) of order K if there exists a positive real constant C and an exponent $s = 1/q - 1/p$, where, $1 \leq q \leq p \leq 2$, such that for all $\mathcal{K} \subset \{1, \dots, N\}$ and all $\mathbf{h} \in N(\mathbf{A})$ where $\#\mathcal{K} \leq K$,*

$$\|\mathbf{h}_{\mathcal{K}}\|_p \leq Ck^{-s} \|\mathbf{h}_{\mathcal{K}^c}\|_q, \quad (1.7)$$

The NSP can be used to not only guarantee the exact recovery of all K -sparse signals but also can guarantee a robustness to non-sparse signals, including compressible signals. This robustness is given in the following theorem.

Theorem 1.1.4 ([39, Theorem 8.1]). *Given a norm $\|\cdot\|_p$, a matrix \mathbf{A} and a positive integer K . If \mathbf{A} satisfies the mixed NSP in (p, q) of order $2K$ with a constant $C_0/2$ and an exponent $s = 1/q - 1/p$, where, $1 \leq q \leq p \leq 2$, then there exists a recovery algorithm $\Delta(\cdot)$ such that*

$$\|\Delta(\mathbf{A}\boldsymbol{\alpha}) - \boldsymbol{\alpha}\|_p \leq C_0K^{-s} \|\boldsymbol{\alpha} - \boldsymbol{\alpha}_K\|_q. \quad (1.8)$$

Conversely, the validity of Eq.(1.8) for an arbitrary recovery algorithm $\Delta(\cdot)$ implies that \mathbf{A} has the mixed NSP in (p, q) of order $2K$ with constant C_0 and an exponent s .

Guarantees of the form as in Eq.(1.8) are called *instance-optimal* because they hold for all instances of $\boldsymbol{\alpha}$ [39]. A typical choice for the norms in the mixed NSP is $p = 2$ and $q = 1$ or $p = 1$ and $q = 1$.

While the NSP can be used to analyse the suitability of a sensing system for exact sparse and compressible signals, it cannot be used to analyse the system's robustness to noise. To analyse this problem an important property is the restricted isometry property (RIP).

Definition 1.1.5. *A matrix \mathbf{A} satisfies the RIP of order K if for all K -sparse vectors $\boldsymbol{\alpha}$ there exists a positive constant $\delta_K < 1$ which satisfies the following inequalities:*

$$(1 - \delta_K) \|\alpha\|_2^2 \leq \|\mathbf{A}\alpha\|_2^2 \leq (1 + \delta_K) \|\alpha\|_2^2. \quad (1.9)$$

The smallest constant δ_K for which this holds, defines the RIP constant.

When RIP holds, \mathbf{A} approximately preserves the Euclidean distance of K -sparse signals, which implies that K -sparse vectors cannot be in the null space of \mathbf{A} . Hence, this implies that the spark $(\mathbf{A}) \geq K$. The RIP also implies the NSP [57, Theorem 1.5]. Clearly, the RIP is a more restrictive condition than the NSP and the spark.

The RIP is very useful because it can be used to guarantee the performance of practical algorithms for reconstructing sparse and compressive signals from noisy measurements. Many random matrices satisfy RIP with an overwhelming probability. These include $\mathbf{A} \in \mathbb{R}^{M \times N}$, where its elements are i.i.d. entries from a Gaussian, Bernoulli or any other sub-Gaussian distribution. For these classes of matrices, \mathbf{A} will satisfy an order $2K$ RIP with overwhelming probability if

$$M \geq CK \log(N/K), \quad (1.10)$$

where, C is some constant depending on the class of the matrix [7, 90].

RIP can also be shown to hold for pairs of orthogonal bases. If $\mathbf{A} = \mathbf{R}\Phi\Psi$, where, Φ and Ψ are orthogonal bases and \mathbf{R} selects M coordinates uniformly at random then if

$$M \geq CK (\log N)^5, \quad (1.11)$$

then \mathbf{A} satisfies an order $2K$ RIP with overwhelming probability [115].

Finally, RIP can also be shown to hold for sensing matrices of the form $\mathbf{A} = \Phi\Psi$, where, Ψ is a orthogonal basis and Φ is an $M \times N$ random matrix with its entries drawn from one of the previous mentioned distributions. For this class of matrix, with overwhelming probability, \mathbf{A} satisfies an order $2K$ RIP, provided M satisfies Eq. (1.10).

The spark, NSP and RIP all provide guarantees for the recovery of K -sparse signals, however, it appears that verifying that any particular matrix \mathbf{A} satisfies any of these properties requires an algorithm with a combinatorial computational complexity. This is because to verify any one of the properties, one must inspect the properties of all $\binom{N}{K}$ submatrices. Therefore, for a given matrix, it may instead be preferable to use a alternative property that is easily computable and also provides recovery guarantees. The *coherence* of a matrix is a property that satisfies this criteria [126].

Definition 1.1.6. The coherence of a matrix \mathbf{A} is given by the maximum correlation between

any two of its columns $\mathbf{a}_i, \mathbf{a}_j$:

$$\mu(\mathbf{A}) = \max_{1 \leq i < j \leq N} \frac{|\langle \mathbf{a}_i, \mathbf{a}_j \rangle|}{\|\mathbf{a}_i\|_2 \|\mathbf{a}_j\|_2} \quad (1.12)$$

The coherence of a matrix is always in the range $\mu(\mathbf{A}) \in \left[\frac{N-M}{M(N-1)}, 1 \right]$ [135]. It can be used to show the uniqueness of the exact sparse problem.

Theorem 1.1.7 ([125, Corollary 3.6]). *For any vector \mathbf{y} , if*

$$K < \left(1 + \frac{1}{\mu(\mathbf{A})} \right), \quad (1.13)$$

then there exist at most one signal $\boldsymbol{\alpha} \in \Sigma_K$, where, $\mathbf{y} = \mathbf{A}\boldsymbol{\alpha}$.

Coherence can also be used to show a particular matrix \mathbf{A} satisfies the RIP.

Lemma 1.1.8 ([57, Lemma 1.5]). *If a matrix \mathbf{A} has unit-norm columns and a particular coherence then the matrix has an RIP of order K with $\delta_K = (K-1)\mu(\mathbf{A})$ for all $K < \mu(\mathbf{A})^{-1}$.*

Reconstruction

The problem of recovering sparse or approximating compressible signals can be formulated as the optimisation program

$$\underset{\hat{\boldsymbol{\alpha}}}{\text{minimise}} \|\hat{\boldsymbol{\alpha}}\|_0 \text{ subject to } \mathbf{y} = \mathbf{A}\hat{\boldsymbol{\alpha}}. \quad (1.14)$$

To solve this program requires a combinatorial computational complexity algorithm. Therefore, instead of solving this problem, many practical signal reconstruction algorithms have been proposed that have a polynomial time computational complexity. The two main classes of tractable algorithms are convex relaxations and greedy methods.

Convex Relaxations A convex relaxation is where the ℓ_0 -norm in Eq. 1.14 is replaced by the convex ℓ_1 -norm. The modified program is then given by

$$\underset{\hat{\boldsymbol{\alpha}}}{\text{minimise}} \|\hat{\boldsymbol{\alpha}}\|_1 \text{ subject to } \mathbf{y} = \mathbf{A}\hat{\boldsymbol{\alpha}}. \quad (1.15)$$

If \mathbf{A} has an RIP then the solution to Eq. (1.15) has the following guarantee.

Theorem 1.1.9 ([23, Theorem 1.1]). *If \mathbf{A} has a RIP of order $2K$ with $\delta_{2K} < \sqrt{2} - 1$ then the solution $\hat{\boldsymbol{\alpha}}$ of Eq. (1.15) satisfies*

$$\|\hat{\boldsymbol{\alpha}} - \boldsymbol{\alpha}\|_2 \leq C_0 \frac{\|\boldsymbol{\alpha} - \boldsymbol{\alpha}_K\|_2}{\sqrt{K}} \quad (1.16)$$

for some constant C_0 .

If algorithms are to be useful in a practical setting, they need to be able to deal with compressible signals and also with noise. The system equation with additive noise is given by

$$\mathbf{y} = \mathbf{A}\boldsymbol{\alpha} + \mathbf{n}, \quad (1.17)$$

where, \mathbf{n} is a stochastic or deterministic error term. If \mathbf{A} has an RIP then the solution to the constrained optimisation program,

$$\min_{\hat{\boldsymbol{\alpha}}} \|\hat{\boldsymbol{\alpha}}\|_1 \text{ subject to } \|\mathbf{y} - \mathbf{A}\hat{\boldsymbol{\alpha}}\|_2 \leq \epsilon, \quad (1.18)$$

is robust in the following sense.

Theorem 1.1.10 ([23, Theorem 1.2]). *Assume that $\delta_{2K} < \sqrt{2} - 1$ and $\|\mathbf{n}\|_2 \leq \epsilon$. Then the solution $\hat{\boldsymbol{\alpha}}$ to (1.18) obeys*

$$\|\hat{\boldsymbol{\alpha}} - \boldsymbol{\alpha}\|_2 \leq C_0 \|\boldsymbol{\alpha} - \boldsymbol{\alpha}_K\|_1 / \sqrt{K} + C_1 \epsilon \quad (1.19)$$

for positive constants C_0 and C_1 .

This result shows that a convex optimisation algorithm can be used to estimate a signal with an error that is bounded by the sum of two terms. The first is an error term associated with the approximation of $\boldsymbol{\alpha}$ using a sparse vector, for exact sparse signals this will be zero. The second term is proportional to the noise, for a noiseless system this will be zero. The constants C_0 and C_1 are computable and are only dependent on the order $2K$ RIP constant δ_{2K} .

Greedy Methods The other class of methods for the recovery of sparse signals are greedy methods [88, 17, 40, 52, 101, 126]. They attempt to recover sparse signals by directly trying to approximate the solution to Eq. 1.14. Greedy methods use iterative algorithms to approximate the *support* (the locations of the non-zero elements) of the signal and their corresponding values. Some greedy methods have been shown to have similar performance guarantees to those that have been obtained for convex relaxation approaches [100, 16], and when implemented, many greedy methods have a remarkably similar structure to the convex relaxation approaches. In this thesis we are primarily focused on the adaptations of convex relaxation approaches so we will not provide any further details on greedy methods.

The theoretical results of CS that provide performance guarantees are largely motivational for the SR problem. In practice the constants given in the performance bounds, for a given achievable RIP constant, may be unreasonably large, however, from numerical work it appears that, typically, these constants are small. This suggests the existing bounds are not tight or do not reflect the average performance.

1.2 Organisation

Chapter 2 In the second chapter of this thesis, a discrete observation model for a mono-static spotlight-mode SAR system will be developed. This model will be used throughout the thesis to develop image formation algorithms. We will then investigate fast algorithms for computing the adjoint of this observation model in terms of their accuracy and computational complexity. The fast algorithms are based on fast BP algorithms. A fast BP algorithm will be proposed, which has a novel decimation strategy, and has a number of advantages over existing fast BP algorithms.

Chapter 3 In the third chapter, a framework for iterative image formation will be proposed, which makes use of the fast algorithms from the second chapter. This framework performs near-field imaging with non-flat terrain. The performance of the image formation framework, compared with standard image formation algorithms, will be investigated when the phase histories are fully-sampled and also when they are undersampled. When the phase histories are under-sampled the framework leverages image sparsity and uses tools from the CS field.

Chapter 4 The fourth chapter will consider errors in the system observation model when there is phase history undersampling. The suitability of conventional algorithms (autofocus algorithms) to correct these errors will be investigated. A novel sparsity-based autofocus algorithm will be proposed which corrects errors within its iterative image formation procedure. The performance of the algorithm will be investigated theoretically and through numerical experiments.

Chapter 5 In the fifth chapter, ultra-wideband synthetic aperture radar image formation will be considered. In particular the effect of RFI on image formation. A algorithm will be proposed which uses knowledge of the RFI spectrum and image sparsity to minimise the effects of the RFI on the formed image. The performance of this algorithm will be compared against conventional linear filter based approaches.

Chapter 6 In the final chapter, the key results of this thesis will be summarised and future research, which could build upon this thesis, will be discussed.

1.3 Contributions

The main contributions to this thesis are:

- **Fast algorithms for the system observation model and its adjoint:** we have proposed fast near-field algorithms for the system observation model and its adjoint. These algorithms are required by large-scale gradient based iterative algorithms for image

formation. Two sets of algorithms are proposed, one set is based on existing fast back-projection algorithms and the other set is based on a new decimation strategy which is proposed in this thesis. The new decimation strategy reduces the image-element-wise errors in the image which is not possible with existing algorithms.

- **An iterative near-field image formation framework:** utilising the proposed fast algorithms, we proposed a framework for iterative image formation in the near-field. The superior performance of the framework, relative to matched filter based algorithms, is investigated using both simulated and real SAR phase histories.
- **An Autofocus algorithm for undersampled SAR:** practical SAR systems contain errors in the system observation model which must be corrected using an autofocus algorithm. We show that conventional post-processing autofocus algorithms are unsuitable for undersampled phase histories. Instead, we propose an image formation algorithm which corrects errors within the iterative image formation procedure. This proposed approach improves the quality of the formed images and has a faster convergence rate than previous approaches.
- **Image formation and RFI mitigation for UWB SAR:** due to the large spectrum of UWB signals, RFI can significantly degrade UWB SAR image quality. A significant problem with existing strategies for RFI suppression is that they introduce range sidelobes. We propose an algorithm which uses knowledge of the RFI spectrum to suppress RFI during image formation and does not introduce range sidelobes. The algorithms can also reduce the effect of transmit notching on the formed image.

1.4 Publications

Peer Reviewed Journal Articles:

1. S.I. Kelly, M. Yaghoobi, and M.E. Davies, *Sparsity-based autofocus for under-sampled synthetic aperture radar*, IEEE Trans. Aerosp. Electron. Syst. 50 (2014), no. 2, to appear.
2. S.I. Kelly, C. Du, G. Rilling, and M.E. Davies, *Advanced image formation and processing of partial synthetic aperture radar data*, IET Signal Processing 6 (2012), no. 5, 511–520.

Conference Proceedings:

1. S.I. Kelly and M.E. Davies, *A fast decimation-in-image back-projection algorithm for SAR*, Proc. IEEE Radar Conf., May 2014, to appear.
2. S.I. Kelly and M.E. Davies, *RFI suppression and sparse image formation for UWB SAR*, Proc. Int. Radar Symposium, vol. 2, Jun. 2013, pp. 655–660.

3. S.I. Kelly, M. Yaghoobi, and M.E. Davies, *Auto-focus for under-sampled synthetic aperture radar*, Proc. Sensor Signal Processing Def., Sept. 2012, pp. 1–5.
4. S.I. Kelly, M. Yaghoobi, and M.E. Davies, *Auto-focus for compressively sampled SAR*, Proc. Compressed Sensing Appl. Radar, May 2012.
5. S.I. Kelly, G. Rilling, M.E. Davies, and B. Mulgrew, *Iterative image formation using fast (re/back)-projection for spotlight-mode SAR*, Proc. IEEE Radar Conf., May 2011, pp. 835–840. **Awarded third place in “best student paper award” contest.**

Chapter 2

Fast Synthetic Aperture Radar Image formation

2.1 Introduction

The goal of SAR imaging is to form an image which will be an approximation of the reflectivity of the elements in the scene. This image will consist of a finite number of complex samples. Many algorithms have been proposed for SAR image formation, some of the most popular were introduced in Section 1.1. Until recently, these algorithms were predominately approximations of a matched filter. Arguably the most commonly encountered of these algorithms, for airborne SAR, are the BP algorithm, the RMA and the PFA. Each algorithm has its advantages and disadvantages, which are based around the trade off between image quality and computational complexity. The BP algorithm is the most versatile of these algorithms and provides the best image quality of all the commonly used matched filter based algorithms. This versatility means it can be used for all types of synthetic apertures, chirp bandwidths, beamwidths and scene terrains. In contrast, the RMA is only suitable for flat terrain and synthetic apertures that are linear. While, the PFA is only suitable for far-field imaging. Unfortunately, the complexity of the BP algorithm is much greater than the complexity of the other algorithms and therefore it has seldom been used operationally.

New modalities of SAR, in particular UWB SAR, have renewed interest in the BP algorithm. In these applications, the synthetic aperture can be very long which makes maintaining a linear aperture challenging. Also, at large wavelengths, the antenna beam width is usually large, making the imaging near-field. In these scenarios, the BP algorithm is the only matched filter based algorithm suitable for image formation.

These types of applications have led many researchers to develop algorithms which are as versatile as the BP algorithm but have a reduced complexity [104, 138, 128, 65, 89, 133, 136].

These algorithms are usually referred to as fast BP algorithms. Fast BP algorithms have been proposed which require $\mathcal{O}(N^2 \log N)$ operations for an $N \times N$ pixel image which is formed from a phase history with N aperture positions. This is a reduced order of operations, when compared to the BP algorithm which requires $\mathcal{O}(N^3)$ operations. The reduced complexity order is usually achieved by recursively splitting the image grid and correspondingly decimating the phase history before performing the BP algorithm. In [128] and [65], the image grid is recursively split in a quad tree structure and the phase history is decimated by combining close aperture positions at each stage of recursion, with a beamforming like procedure in a polar coordinate system. In [89, 133, 136], the image is also recursively split in a quad tree structure, however, the phase history is decimated at each stage of recursion in a different manner to the previous algorithms. The phase history is instead decimated independently in fast and slow times. The algorithms presented in [133] and [136] were motivated by [10], which appeared in the tomography literature, but are virtually identical to the algorithm presented in [89]. More recently, in [44], another algorithm has been proposed which has a different strategy for achieving the same order of complexity. The authors state that their “butterfly” algorithm can be considered to be a generalisation of the fast multipole method (FMM) [69]. Variations of the FMM have previously been used to compute fast matrix vector products, for example the FMM based NFFT [55].

In this chapter we will develop a general linear model for a mono-static spotlight-mode SAR system and investigate how this model can be represented in a discrete form. We will then show how approximations are used to reduce the complexity of a matched filter type algorithm. A fast BP algorithm will then be presented which is based on those that are proposed in [89, 133, 136]. A novel fast BP algorithm will also be proposed, which is coined, the fast *decimation-in-image* BP algorithm. The name was selected due to its relation to decimation-in-time FFT algorithms. It is the natural dual of the other fast BP algorithm presented, which we coin as the fast *decimation-in-phase-history* BP algorithm due to its relation to decimation-in-frequency FFT algorithms. The performance of the fast BP algorithms, in terms of their image quality and computational speed, will also be investigated.

2.2 A Mathematical Model for Synthetic Aperture Radar

In this section we will develop a mathematical model for a monostatic side-looking spotlight-mode SAR system. The starting point for this model will be to consider the radio frequency (RF) wave propagation. The developed wave propagation model will then be used to model the transmission and reception of a linear frequency modulated (LFM) chirp signal. A model of the dechirping and deskewing operations will then be developed. Finally, the minimum fast-time sampling rate for the analogue dechirped and deskewed signal will be considered as well as the minimum slow-time sampling rate necessary for a smooth synthetic aperture.

2.2.1 Propagation Model

The development of an RF wave propagation model will follow closely, the development in [36] and [37]. The starting point for this model will be Maxwell's Equations:

$$\nabla \times \mathbf{E} = -\frac{\partial \mathbf{B}}{\partial t} \quad (2.1a)$$

$$\nabla \times \mathbf{H} = \mathbf{J} + \frac{\partial \mathbf{D}}{\partial t} \quad (2.1b)$$

$$\nabla \cdot \mathbf{E} = \rho \quad (2.1c)$$

$$\nabla \cdot \mathbf{B} = 0, \quad (2.1d)$$

Where, \mathbf{E} is the electric field, \mathbf{D} is the electric displacement field, \mathbf{B} is the magnetic field, \mathbf{H} is the magnetising field, ρ is the charge density, \mathbf{J} is the current density and t is time. As illustrated in Fig. 2.1, if we assume that the propagation medium is free space ($\mathbf{D} = \epsilon_0 \mathbf{E}$, $\mathbf{H} = \mu_0 \mathbf{B}$, $\mathbf{J} = 0$ and $\rho = 0$, where, ϵ_0 is the permittivity and μ_0 is the permeability of free space) then Maxwell's equations imply the electromagnetic wave equation for the electric field:

$$\left(\nabla^2 - c_0^{-2} \frac{\partial^2}{\partial t^2} \right) \mathbf{E} = 0, \quad (2.2)$$

where, $c_0 = (\mu_0 \epsilon_0)^{-1/2}$ is the propagation speed of electromagnetic waves in free space. Only the propagating electric field is considered because in this model we will consider only a single transmit and receive polarisation and will also ignore polarisation effects that occur as a result of scattering. Therefore, it is sufficient to consider only the electric field. The Green's function of the wave equation for the electric field, is a function $g(t, \vec{\mathbf{x}})$ that satisfies the homogeneous partial differential equation (PDE):

$$\left(\nabla^2 - c_0^{-2} \frac{\partial^2}{\partial t^2} \right) g(t, \vec{\mathbf{x}}) = -\delta(t, \vec{\mathbf{x}}), \quad (2.3)$$

where, $\vec{\mathbf{x}}$ is a spatial co-ordinate. This Green's function is given by:

$$g(t, \vec{\mathbf{x}}) = \frac{\delta(t - \|\vec{\mathbf{x}}\|/c_0)}{4\pi \|\vec{\mathbf{x}}\|}. \quad (2.4)$$

We can use this Green's function to derive the transmitted field. If we assume the transmitter is at a point $\vec{\mathbf{x}}$, and produces an electrical potential $s(t)$, then the resulting field $\mathbf{E}_{\text{in}}(t, \vec{\mathbf{y}})$, at a position $\vec{\mathbf{y}}$, is given by:

$$\begin{aligned} \mathbf{E}_{\text{in}}(t, \vec{\mathbf{y}}) &= (g * s)(t, \vec{\mathbf{y}} - \vec{\mathbf{x}}) = \int g(t - \tau, \vec{\mathbf{y}} - \vec{\mathbf{x}}) s(\tau) d\tau \\ &= \frac{s(t - \|\vec{\mathbf{y}} - \vec{\mathbf{x}}\|/c_0)}{4\pi \|\vec{\mathbf{y}} - \vec{\mathbf{x}}\|}. \end{aligned} \quad (2.5)$$

Now that we have a model of the transmitted field we will consider its scattering. If we model scattering in terms of classical scattering theory, the electric field \mathbf{E}_{tot} at a scatterer is equal to the sum of the incident \mathbf{E}_{in} and the scattered field \mathbf{E}_{sc} , i.e. $\mathbf{E}_{\text{tot}} = \mathbf{E}_{\text{in}} + \mathbf{E}_{\text{sc}}$. Therefore, the scattered field at a position $\vec{\mathbf{z}}$ from a scatterer at a position $\vec{\mathbf{y}}$ satisfies:

$$\left(\nabla^2 - c_0^{-2} \frac{\partial^2}{\partial t^2} \right) \mathbf{E}_{\text{sc}}(t, \vec{\mathbf{z}}) = -v(\vec{\mathbf{y}}) \frac{\partial^2}{\partial t^2} \mathbf{E}(t, \vec{\mathbf{y}}), \quad (2.6)$$

where, $v(\vec{\mathbf{y}}) = c_0^{-2} - c(\vec{\mathbf{y}})^{-2}$ is the reflectivity of the scatterer at $\vec{\mathbf{y}}$ and $c(\vec{\mathbf{y}})$ is the wave speed at $\vec{\mathbf{y}}$. Hence, using the Green's function and Eq. (2.6), the resulting scattered field $\mathbf{E}_{\text{sc}}(t, \vec{\mathbf{z}})$ at a position $\vec{\mathbf{z}}$ will be given by:

$$\mathbf{E}_{\text{sc}}(t, \vec{\mathbf{z}}) = \int \int g(t - \tau, \vec{\mathbf{z}} - \vec{\mathbf{y}}) v(\vec{\mathbf{y}}) \frac{\partial^2}{\partial t^2} \mathbf{E}_{\text{tot}}(\tau, \vec{\mathbf{y}}) d\tau d\vec{\mathbf{y}} \quad (2.7)$$

In SAR we are interested in determining the reflectivities $v(\vec{\mathbf{y}})$ from the scattered field $\mathbf{E}_{\text{sc}}(t, \vec{\mathbf{z}})$. Therefore, to linearise the relationship between the two, we use the Born approximation. This involves replacing the total field \mathbf{E}_{tot} , within the previous integral, with the incident field \mathbf{E}_{in} , resulting in:

$$\begin{aligned} \mathbf{E}_{\text{sc}}(t, \vec{\mathbf{z}}) &\approx \int \int g(t - \tau, \vec{\mathbf{z}} - \vec{\mathbf{y}}) v(\vec{\mathbf{y}}) \frac{\partial^2}{\partial t^2} \mathbf{E}_{\text{in}}(\tau, \vec{\mathbf{y}}) d\tau d\vec{\mathbf{y}} \\ &= \int \frac{v(\vec{\mathbf{y}})}{4\pi \|\vec{\mathbf{z}} - \vec{\mathbf{y}}\|} \frac{\partial^2}{\partial t^2} \mathbf{E}_{\text{in}}(t - \|\vec{\mathbf{z}} - \vec{\mathbf{y}}\|/c_0, \vec{\mathbf{y}}) d\vec{\mathbf{y}} \\ &= \int \frac{v(\vec{\mathbf{y}})}{(4\pi)^2 \|\vec{\mathbf{z}} - \vec{\mathbf{y}}\| \|\vec{\mathbf{y}} - \vec{\mathbf{x}}\|} \frac{\partial^2}{\partial t^2} s(t - (\|\vec{\mathbf{z}} - \vec{\mathbf{y}}\| + \|\vec{\mathbf{y}} - \vec{\mathbf{x}}\|)/c_0) d\vec{\mathbf{y}}. \end{aligned} \quad (2.8)$$

The Born approximation is extremely useful because it makes the relationship between the scattered field $\mathbf{E}_{\text{sc}}(t, \vec{\mathbf{z}})$ and reflectivities $v(\vec{\mathbf{y}})$ linear, however, it ignores all second order scattering interactions and therefore ignores multiple bounce scattering effects. The Born approximation is used in virtual all work in radar imaging.

2.2.2 Linear Frequency Modulated Chirped Radar

The developed RF propagation model can be used to model the transmission and reception of a LFM chirp. To do this we will make use of the ubiquitously used stop-and-hop approximation. This approximation assumes that during the time of transmission and reception, the SAR platform has an approximately constant position and therefore the fast and slow times can be considered independently. This is a good approximation in SAR because the platform velocity is much less than the velocity of the propagating RF wave.

An LFM chirp signal is given by $\text{Re}\{s(t)\}$, where,

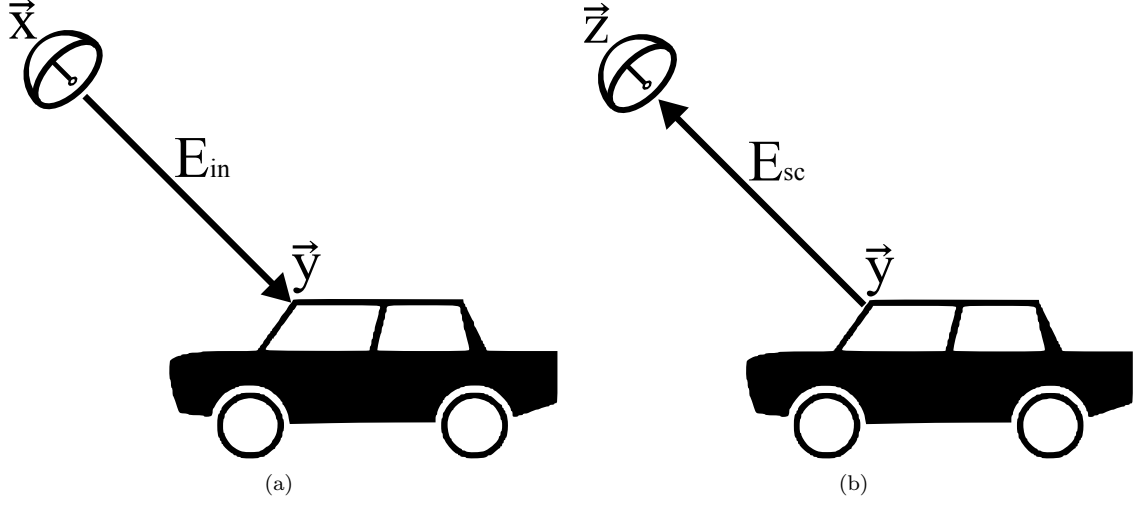


Figure 2.1: RF wave propagation model: (a) incident field and (b) scattered field.

$$s(t) = w(t) \exp(j(\omega_0 t + \alpha t^2)), \quad (2.9)$$

ω_0 is the carrier frequency, 2α is the chirp rate and $w(t)$ is a window function centred around the fast-time $t = 0$, with a period T_s such that $w(|t| > T_s/2) = 0$. This window can be $\text{rect}(t/T_s)$ or a slowly varying function, e.g. Taylor window.

In this model we will consider monostatic radar, therefore, the transmitter and receiver are located at the same position, i.e. $\vec{z} = \vec{x}$. At this position \vec{x} , we denote the scene radius in the range direction as $L_u(\vec{x})$, which is centred around a distance $u_0(\vec{x})$ from the transmitter. The scene centre and radius are controlled by the antenna beam pattern. Incorporating these details into Eq. 2.8, we get a model for the electric field at the receiver $\mathbf{E}_r(t, \vec{x})$ which is given by:

$$\mathbf{E}_r(t, \vec{x}) = \text{Re} \left\{ \int_{-L_u(\vec{x})}^{+L_u(\vec{x})} A(t, u_0(\vec{x}) + u) p(u_0(\vec{x}) + u, \vec{x}) s\left(t - t_0(\vec{x}) - \frac{2u}{c_0}\right) du \right\} \quad (2.10)$$

where,

$$\begin{aligned}
A(t, u_0(\vec{x}) + u) &= (4\pi(u_0(\vec{x}) + u))^{-2} \left(\frac{d^2 w \left(t - \frac{2(u_0(\vec{x}) + u)}{c_0} \right)}{dt^2} + \right. \\
&\quad \left. j2 \frac{dw \left(t - \frac{2(u_0(\vec{x}) + u)}{c_0} \right)}{dt} \left(\omega_0 + 2\alpha \left(t - \frac{2(u_0(\vec{x}) + u)}{c_0} \right) \right) + \right. \\
&\quad \left. w \left(t - \frac{2(u_0(\vec{x}) + u)}{c_0} \right) \left(j2\alpha - \left(\omega_0 + 2\alpha \left(t - \frac{2(u_0(\vec{x}) + u)}{c_0} \right) \right)^2 \right) \right) \\
&\quad (2.11)
\end{aligned}$$

$$\begin{aligned}
&\approx - \left(\frac{\omega_0 + 2\alpha \left(t - \frac{2(u_0(\vec{x}) + u)}{c_0} \right)}{4\pi(u_0(\vec{x}) + u)} \right)^2 w \left(t - \frac{2(u_0(\vec{x}) + u)}{c_0} \right) \\
&= a(t, u_0(\vec{x}) + u) w \left(t - t_0(\vec{x}) - \frac{2u}{c_0} \right), \\
&\quad (2.12)
\end{aligned}$$

$t_0(\vec{x}) = 2u_0(\vec{x})/c_0$ is the two way delay from the platform to the scene centre and

$$\begin{aligned}
p(u_0(\vec{x}) + u, \vec{x}) &= \int v(\vec{y}) \delta(\|\vec{y} - \vec{x}\| - (u_0(\vec{x}) + u)) \delta(z(y_1, y_2) - y_3) \\
&\quad b_\theta(\vec{y}, \vec{x}) b_\phi(\vec{y}, \vec{x}) d\vec{y} \\
&\quad (2.13)
\end{aligned}$$

are the accumulated reflectivities of scatterers at a range distance $u_0(\vec{x}) + u$ from the platform and

$$b_\phi(\vec{y}, \vec{x}) = \text{rect} \left(\frac{\phi(\vec{y} - \vec{x}) - \phi_0(\vec{x})}{\Phi/2} \right) \quad (2.14a)$$

$$b_\theta(\vec{y}, \vec{x}) = \text{rect} \left(\frac{\theta(\vec{y} - \vec{x}) - \theta_0(\vec{x})}{\Theta/2} \right), \quad (2.14b)$$

as visualised in Fig. 2.2, model the antenna beam in the spherical coordinates, $\theta(\vec{z}) = \cos^{-1}(z_3/\|\vec{z}\|)$ and $\phi(\vec{z}) = \tan^{-1}(z_2/z_1)$, with a azimuth beamwidth of Θ and a polar beamwidth of Φ . $\theta_0(\vec{x}) = \theta(\vec{y}_0 - \vec{x})$ and $\phi_0(\vec{x}) = \phi(\vec{y}_0 - \vec{x})$ are the angles associated with the centre of the beam, where, \vec{y}_0 is a position on the scene surface which is used to centre the beam. This is a very simplified model of an antenna beam pattern. In spotlight mode SAR, the beam centre \vec{y}_0 remains constant for all positions along the aperture. Scattering is assumed to occurs only at the surface $[y_1, y_2, z(y_1, y_2)]^T$, where, $z(y_1, y_2)$ is the surface height at (y_1, y_2) .

Eq. (2.11) can usually be well approximated by Eq. (2.12). This is because the third term dominates the first two terms in Eq. (2.11). Which is true because $w(t)$ is a slowly varying function in time and therefore its derivatives will be small. Also, the squared value of the carrier frequency is generally much larger than the chirp rate, i.e. $\omega_0^2 \gg 2\alpha$, so the $j2\alpha$ factor in the third term can also be ignored.

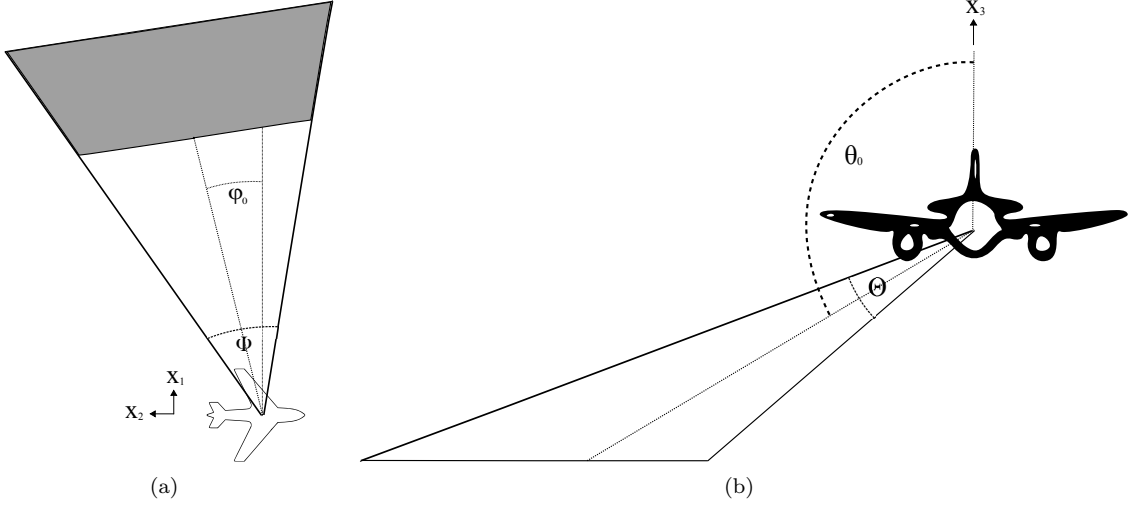


Figure 2.2: SAR antenna beam angles: (a) azimuth angles and (b) polar angles.

Finally, the scene radius and scene centre in the range direction can be explicitly defined as

$$2L_u(\vec{\mathbf{x}}) = \max\{\|\vec{\mathbf{y}} - \vec{\mathbf{x}}\| : \vec{\mathbf{y}} \in \mathcal{Y}_{\vec{\mathbf{x}}}\} - \min\{\|\vec{\mathbf{y}} - \vec{\mathbf{x}}\| : \vec{\mathbf{y}} \in \mathcal{Y}_{\vec{\mathbf{x}}}\} \quad (2.15a)$$

$$2u_0(\vec{\mathbf{x}}) = \max\{\|\vec{\mathbf{y}} - \vec{\mathbf{x}}\| : \vec{\mathbf{y}} \in \mathcal{Y}_{\vec{\mathbf{x}}}\} + \min\{\|\vec{\mathbf{y}} - \vec{\mathbf{x}}\| : \vec{\mathbf{y}} \in \mathcal{Y}_{\vec{\mathbf{x}}}\} \quad (2.15b)$$

where, $\mathcal{Y}_{\vec{\mathbf{x}}} = \{\vec{\mathbf{y}} : b_\theta(\vec{\mathbf{y}}, \vec{\mathbf{x}})b_\phi(\vec{\mathbf{y}}, \vec{\mathbf{x}})\delta(h(y_1, y_2) - y_3) \neq 0\}$ is the set of all reflectivities within the antenna beam at a platform position $\vec{\mathbf{x}}$. The scene radius is half the distance between the furthest and the closest scene element within the antenna beam in the range direction. The scene centre is defined as the point between the furthest and the closest scene element.

Fig. 2.3(a) shows a time-frequency plot for a simulated $\mathbf{E}_r(t, \vec{\mathbf{x}})$ at a platform position $\vec{\mathbf{x}}$, where the scene contains three targets.

2.2.3 Dechirping

To reduce the sampling requirements of the receiver analog-to-digital converter (ADC), a technique known as dechirping is commonly used in high resolution SAR systems. Therefore, we will consider a dechirping operation in our model. The mathematical description of dechirping and deskewing, which is to follow, is based on [29]. However, it is incorporated into our more detailed propagation and scattering models.

A description of dechirping is as follows. Firstly the received signal $\mathbf{E}_r(t, \vec{\mathbf{x}})$ is mixed with

two reference chirps:

$$\text{rect} \left(\frac{t - t_0(\vec{x})}{T_s + 4L_u(\vec{x})/c_0} \right) \cos \left(\omega_0 (t - t_0(\vec{x})) + \alpha (t - t_0(\vec{x}))^2 \right) \quad (2.16a)$$

$$- \text{rect} \left(\frac{t - t_0(\vec{x})}{T_s + 4L_u(\vec{x})/c_0} \right) \sin \left(\omega_0 (t - t_0(\vec{x})) + \alpha (t - t_0(\vec{x}))^2 \right). \quad (2.16b)$$

The two resulting signals from the mixing are

$$\begin{aligned} r_{\text{real}}(t, \vec{x}) = & \frac{1}{2} \text{Re} \left\{ \int_{-L_u(\vec{x})}^{+L_u(\vec{x})} a(t, u_0(\vec{x}) + u) w \left(t - t_0(\vec{x}) - \frac{2u}{c_0} \right) p(u_0(\vec{x}) + u, \vec{x}) \right. \\ & \exp \left(j\alpha \left(\frac{2u}{c_0} \right)^2 \right) \exp \left(-j \frac{2u}{c_0} (\omega_0 + 2\alpha (t - t_0(\vec{x}))) \right) \\ & \left. \left(\exp \left(j \left(2\omega_0 (t - t_0(\vec{x})) + 2\alpha (t - t_0(\vec{x}))^2 \right) \right) + 1 \right) du \right\} \end{aligned} \quad (2.17a)$$

$$\begin{aligned} r_{\text{imag}}(t, \vec{x}) = & \frac{1}{2} \text{Im} \left\{ \int_{-L_u(\vec{x})}^{+L_u(\vec{x})} a(t, u_0(\vec{x}) + u) w \left(t - t_0(\vec{x}) - \frac{2u}{c_0} \right) p(u, \vec{x}) \right. \\ & \exp \left(j\alpha \left(\frac{2u}{c_0} \right)^2 \right) \exp \left(-j \frac{2u}{c_0} (\omega_0 + 2\alpha (t - t_0(\vec{x}))) \right) \\ & \left. \left(\exp \left(j \left(2\omega_0 (t - t_0(\vec{x})) + 2\alpha (t - t_0(\vec{x}))^2 \right) \right) - 1 \right) du \right\}. \end{aligned} \quad (2.17b)$$

$r_{\text{real}}(t, \vec{x})$ and $r_{\text{imag}}(t, \vec{x})$ are then low-pass filtered to produce

$$\begin{aligned} y_{\text{real}}(t, \vec{x}) = & \frac{1}{2} \text{Re} \left\{ \int_{-L_u(\vec{x})}^{+L_u(\vec{x})} a(t, u_0(\vec{x}) + u) w \left(t - t_0(\vec{x}) - \frac{2u}{c_0} \right) p(u_0(\vec{x}) + u, \vec{x}) \right. \\ & \left. \exp \left(j\alpha \left(\frac{2u}{c_0} \right)^2 \right) \exp \left(-j \frac{2u}{c_0} (\omega_0 + 2\alpha (t - t_0(\vec{x}))) \right) du \right\} \end{aligned} \quad (2.18a)$$

$$\begin{aligned} y_{\text{imag}}(t, \vec{x}) = & \frac{1}{2} \text{Im} \left\{ \int_{-L_u(\vec{x})}^{+L_u(\vec{x})} a(t, u_0(\vec{x}) + u) w \left(t - t_0(\vec{x}) - \frac{2u}{c_0} \right) p(u_0(\vec{x}) + u, \vec{x}) \right. \\ & \left. \exp \left(j\alpha \left(\frac{2u}{c_0} \right)^2 \right) \exp \left(-j \frac{2u}{c_0} (\omega_0 + 2\alpha (t - t_0(\vec{x}))) \right) du \right\}. \end{aligned} \quad (2.18b)$$

These two filtered signals are then used as the real and imagery parts of the complex dechirped signal, $y(t, \vec{x}) = y_{\text{real}}(t, \vec{x}) + jy_{\text{imag}}(t, \vec{x})$, which is given by:

$$\begin{aligned} y(t, \vec{x}) = & \frac{1}{2} \int_{-L_u(\vec{x})}^{+L_u(\vec{x})} a(t, u_0(\vec{x}) + u) w \left(t - t_0(\vec{x}) - \frac{2u}{c_0} \right) p(u_0(\vec{x}) + u, \vec{x}) \\ & \exp \left(j\alpha \left(\frac{2u}{c_0} \right)^2 \right) \exp \left(-j \frac{2u}{c_0} (\omega_0 + 2\alpha (t - t_0(\vec{x}))) \right) du. \end{aligned} \quad (2.19)$$

Fig. 2.3(b) shows a time-frequency plot for a simulated version of the dechirped signal $y(t, \vec{x})$. For the example shown in this figure, the bandwidth of the received signal has been reduced from 324 MHz to approximately 200 MHz by dechirping.

2.2.4 Deskewing

The time delay between the scattered field from close targets and far targets in the scene is sometimes referred to as skew. If the scene size is large, a dechirped signal will contain significant skew. Deskewing is a process which removes this skew from the dechirped signal. Deskewing will remove the $2u/c_0$ term in the window function $w(\cdot)$ and also will remove the $\exp(j\alpha(2u/c_0)^2)$ term in Eq. 2.19 (known as the residual video phase (RVP)). The process of deskewing is described in the following. The process involves taking a Fourier transform of Eq. 2.19 with respect to $t - t_0(\vec{x})$, which results in

$$\mathcal{F}_{t-t_0(\vec{x})}(\omega, \vec{x}) \{y(t, \vec{x})\} = \frac{1}{2} \int_{-L_u(\vec{x})}^{+L_u(\vec{x})} \mathcal{A}\left(\omega + \frac{4u\alpha}{c_0}, u_0(\vec{x}) + u\right) p(u_0(\vec{x}) + u, \vec{x}) \exp\left(-j\alpha\left(\frac{2u}{c_0}\right)^2\right) \exp\left(-j\frac{2u}{c_0}(\omega_0 + \omega)\right) du, \quad (2.20)$$

where,

$$\mathcal{A}\left(\omega + \frac{4u\alpha}{c_0}, u_0(\vec{x}) + u\right) = \mathcal{F}_{t-t_0(\vec{x})}\left(\omega + \frac{4u\alpha}{c_0}, u_0(\vec{x}) + u\right) \left\{ a'(t - t_0(\vec{x}), u_0(\vec{x}) + u) w(t - t_0(\vec{x})) \right\}, \quad (2.21)$$

and

$$a'(t - t_0(\vec{x}), u_0(\vec{x}) + u) = -\left(\frac{\omega_0 + 2\alpha(t - t_0(\vec{x}))}{4\pi(u_0(\vec{x}) + u)}\right)^2. \quad (2.22)$$

The Fourier transformed signal is then multiplied by $\exp(-j\omega^2/4\alpha)$ to produce

$$\tilde{y}(\omega, \vec{x}) = \frac{1}{2} \int_{-L_u(\vec{x})}^{+L_u(\vec{x})} \mathcal{A}\left(\omega + \frac{4u\alpha}{c_0}, u_0(\vec{x}) + u\right) p(u_0(\vec{x}) + u, \vec{x}) \exp\left(-j\frac{\left(\omega + \frac{4u\alpha}{c_0}\right)^2}{4\alpha}\right) \exp\left(-j\frac{2u}{c_0}(\omega_0)\right) du \quad (2.23)$$

If we then take the inverse Fourier transform of Eq.(2.23) we get

$$\mathcal{F}_\omega^{-1}(t - t_0(\vec{x}), \vec{x}) \{ \tilde{y}(\omega, \vec{x}) \} \approx \frac{1}{2} \int_{-L_u(\vec{x})}^{+L_u(\vec{x})} a'(t - t_0(\vec{x}), u_0(\vec{x}) + u) w(t - t_0(\vec{x})) p(u_0(\vec{x}) + u, \vec{x}) \exp\left(-j \frac{2u}{c_0} (\omega_0 + 2\alpha(t - t_0(\vec{x})))\right) du \quad (2.24)$$

which is a good approximation if

$$\int \mathcal{A}(\omega, u_0(\vec{x}) + u) \exp\left(-j \frac{\omega^2}{4\alpha}\right) - \mathcal{A}(\omega, u_0(\vec{x}) + u) d\omega \approx 0. \quad (2.25)$$

Using this approximation will introduce a small amount of error into the model. The errors introduced by this approximation can be viewed as a chirping of the frequency sidelobes of the signal. Fig. 2.3(c) shows a time-frequency plot for a simulated version of the dechirped and deskewed signal in Eq.(2.24). This chirping effect can be seen particularly at the edges of the support of each chirp. These artifacts are usually negligible but can be minimised, if required, by using a windowed chirp waveform. It can also be seen that the returns from the three targets are no longer skewed. In practice deskewing is done on the sampled dechirped signal, therefore, a DFT and an inverse discrete Fourier transform (IDFT) are used instead of their continuous versions.

2.2.5 Continuous Observation Model

Using the developed models for dechirping, deskewing and wave propagation and also defining

$$k_u(t - t_0(\vec{x})) = \frac{2}{c_0} (\omega_0 + 2\alpha(t - t_0(\vec{x}))), \quad (2.26)$$

after dechirping and deskewing our complete continuous SAR observation model can be given by

$$\tilde{y}(t, \vec{x}) = \frac{1}{2} w(t - t_0(\vec{x})) \left(\int_{-L_u(\vec{x})}^{+L_u(\vec{x})} a'(t - t_0(\vec{x}), u_0(\vec{x}) + u) p(u_0(\vec{x}) + u, \vec{x}) \exp(-jk_u(t - t_0(\vec{x}))u) du \right), \quad (2.27)$$

where, $\Delta k_u = 4\alpha T_s / c_0$. Interestingly, Eq.(2.27) can be viewed as a weighted short spatial Fourier transform of the accumulated reflectivities with a limited spatial Fourier support of

$$\frac{2}{c_0} (\omega_0 - \alpha T_s) \leq k_u(t - t_0(\vec{x})) \leq \frac{2}{c_0} (\omega_0 + \alpha T_s) \quad (2.28)$$

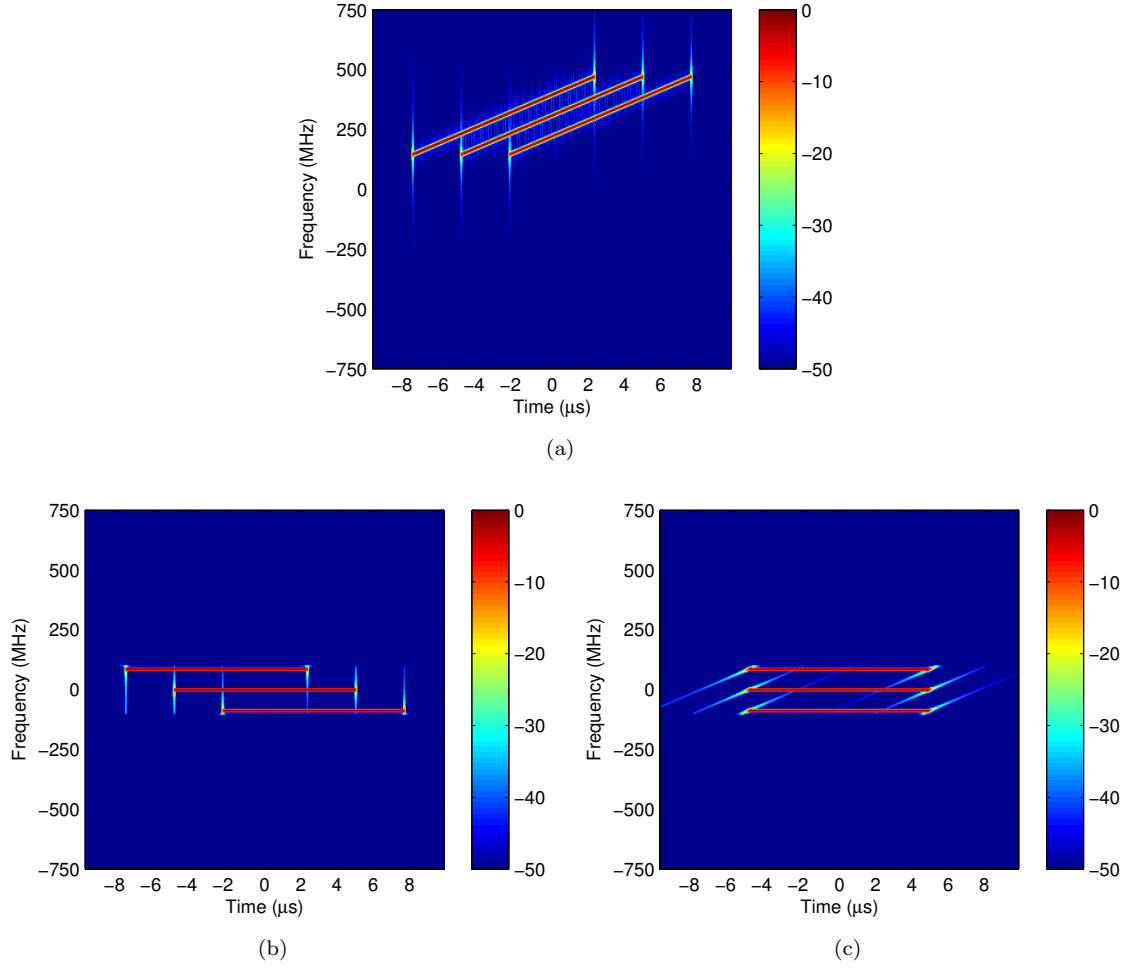


Figure 2.3: A time-frequency plot of a simulated received signal from three targets at the different stages of receiver processing. Where, $\omega_0/2\pi = 308$ MHz, $\alpha/\pi = 32.4$ MHz/ μ s and $T = 10$ μ s. (a) is the unprocessed received signal. (b) is the received signal after dechirping. (c) is the dechirped signal after deskewing.

2.2.6 Phase History Sampling Requirements

In this section we will determine the minimum sampling rate requirements for slow and fast times. In order to sample an analog signal without aliasing the Nyquist-Shannon sampling theorem states that we must sample a complex signal at a rate greater or equal to its bandwidth. Therefore, to determine a minimum sampling rate, we must determine the bandwidth of the received signals in fast and slow times.

The bandwidth of the dechirped signal in Eq. (2.27), with respect to its fast-time, is approximately equal to the difference between the maximum and minimum instantaneous frequencies of its complex exponent, this is given by

$$\begin{aligned}
 f_{t_{\min}}(\vec{x}) &\approx \frac{1}{2\pi} \max \left\{ \left| \frac{d}{dt} (-k_u(t - t_0(\vec{x}))u_a) - \frac{d}{dt} (-k_u(t - t_0(\vec{x}))u_b) \right| : \right. \\
 &\quad \left. u_a \in [-L_u(\vec{x}), +L_u(\vec{x})], u_b \in [-L_u(\vec{x}), +L_u(\vec{x})] \right\} \\
 &= \frac{4L_u(\vec{x})\alpha}{\pi c_0} \text{ [samples / second]}.
 \end{aligned} \tag{2.29}$$

Determining the bandwidth with respect to the slow-time is not as straight forward as for the fast-time. We denote slow-time as \hat{t} , where $\hat{t} = 0$ is the slow-time at the beginning of the synthetic aperture and $\hat{t} = T_{\hat{t}}$ at the end. To simplify our analysis we will assume that our platform motion is smoothly varying, such that its position $\vec{x}(\hat{t})$ with respect to the slow-time \hat{t} , can be well approximated about a time \hat{t}_0 by $\vec{x}'(\hat{t}, \hat{t}_0) = \vec{x}(\hat{t}_0) + \vec{v}(\hat{t}, \hat{t}_0) = [x_1(\hat{t}_0) + v_1(\hat{t}_0)(\hat{t} - \hat{t}_0), x_2(\hat{t}_0) + v_2(\hat{t}_0)(\hat{t} - \hat{t}_0), x_3]^T$. The bandwidth of the signal in Eq. (2.27), with respect to its slow time is then approximately given by

$$\begin{aligned}
 f_{\hat{t}_{\min}} &\approx \frac{1}{2\pi} \max \left\{ \left| -k_u(t - t_0) \frac{d}{d\hat{t}} ((\|\vec{y}_a - \vec{x}'(\hat{t}, \hat{t}_a)\| - \|\vec{y}_0 - \vec{x}'(\hat{t}, \hat{t}_a)\|)) + \right. \right. \\
 &\quad \left. \left. k_u(t - t_0) \frac{d}{d\hat{t}} ((\|\vec{y}_b - \vec{x}'(\hat{t}, \hat{t}_b)\| - \|\vec{y}_0 - \vec{x}'(\hat{t}, \hat{t}_b)\|)) \right| : \right. \\
 &\quad \left. \hat{t}_a \in [0, T_{\hat{t}}], \hat{t}_b \in [0, T_{\hat{t}}], \vec{y}_a \in \mathcal{Y}_{\vec{x}'(\hat{t}, \hat{t}_a)}, \vec{y}_b \in \mathcal{Y}_{\vec{x}'(\hat{t}, \hat{t}_b)}, t - t_0 \in \left[-\frac{T_s}{2}, \frac{T_s}{2} \right] \right\}.
 \end{aligned} \tag{2.30}$$

In order to find an analytic expression which approximates the bandwidth $f_{\hat{t}_{\min}}$, we expand u using a first order Taylor expansion. The derivative of u with respect to the slow-time then becomes approximately given by:

$$\begin{aligned}
\frac{d}{d\hat{t}} (\|\vec{y} - \vec{x}'(\hat{t}, \hat{t}_0)\| - \|\vec{y}_0 - \vec{x}'(\hat{t}, \hat{t}_0)\|) &\approx \frac{d}{d\hat{t}} \left\{ \left(\|\vec{y} - \vec{x}(\hat{t}_0)\| - \|\vec{y}_0 - \vec{x}(\hat{t}_0)\| + (\hat{t} - \hat{t}_0) \right. \right. \\
&\quad \left(\frac{v_1(\hat{t}_0)(x_1(\hat{t}_0) - y_1) + v_2(\hat{t}_0)(x_2(\hat{t}_0) - y_2)}{\|\vec{y} - \vec{x}(\hat{t}_0)\|} - \right. \\
&\quad \left. \left. \frac{v_1(\hat{t}_0)(x_1(\hat{t}_0) - y_{01}) + v_2(\hat{t}_0)(x_2(\hat{t}_0) - y_{02})}{\|\vec{y}_0 - \vec{x}(\hat{t}_0)\|} \right) \right\} \\
&= \frac{v_1(\hat{t}_0)(y_{01} - x_1(\hat{t}_0)) + v_2(\hat{t}_0)(y_{02} - x_2(\hat{t}_0))}{\|\vec{y}_0 - \vec{x}(\hat{t}_0)\|} - \\
&\quad \frac{v_1(\hat{t}_0)(y_1 - x_1(\hat{t}_0)) + v_2(\hat{t}_0)(y_2 - x_2(\hat{t}_0))}{\|\vec{y} - \vec{x}(\hat{t}_0)\|} \\
&= \sin(\theta_0(\vec{x}(\hat{t}_0)))(v_1(\hat{t}_0) \cos(\phi_0(\vec{x}(\hat{t}_0))) + \\
&\quad v_2(\hat{t}_0) \sin(\phi_0(\vec{x}(\hat{t}_0)))) - \\
&\quad \sin(\theta(\vec{y} - \vec{x}(\hat{t}_0)))(v_1(\hat{t}_0) \cos(\phi(\vec{y} - \vec{x}(\hat{t}_0))) + \\
&\quad v_2(\hat{t}_0) \sin(\phi(\vec{y} - \vec{x}(\hat{t}_0)))) \\
&= \|\vec{v}(\hat{t}, \hat{t}_0)\| (\sin(\theta_0(\vec{x}(\hat{t}_0))) \\
&\quad \cos(\phi_0(\vec{x}(\hat{t}_0)) - \phi(\vec{v}(\hat{t}, \hat{t}_0))) - \\
&\quad \sin(\theta(\vec{y} - \vec{x}(\hat{t}_0))) \\
&\quad \cos(\phi(\vec{y} - \vec{x}(\hat{t}_0)) - \phi(\vec{v}(\hat{t}, \hat{t}_0))))
\end{aligned} \tag{2.31}$$

If we assume that the polar angle $\theta_0(\vec{x}(\hat{t}_0))$ and the magnitude of the platform velocity $\|\vec{v}(\hat{t}, \hat{t}_0)\|$ are constant in slow-time then we can compute an approximation of the worst-case bandwidth which is given by:

$$f_{\hat{t}_{\min}} \approx \frac{2 \|\vec{v}\| k_u \left(\frac{T_s}{2}\right)}{\pi} \sin\left(\theta_0 - \frac{\Theta}{2}\right) \sin\left(\frac{\Phi}{2}\right) [\text{samples / second}] \tag{2.32}$$

This approximation is valid for virtually all systems where the beam is pointed downwards towards the scene and therefore its antenna beam's polar angle is in the range $(\pi/2, \pi)$.

If we define a fast-time sample rate of $f_t > \max\{f_{t_{\min}}(\vec{x}), \vec{x} \in \mathcal{X}\}$ and a slow-time sample rate of $f_{\hat{t}} > f_{\hat{t}_{\min}}$, where, $\mathcal{X} = \{\vec{x}(\hat{t}) : \hat{t} \in [0, T_{\hat{t}}]\}$ is the set of all platform positions along the synthetic aperture and define a fast-time sampling interval of $T_t > T_s$, the sampled phase histories can be modelled as

$$\mathbf{Y} = \{y_{mn} = \tilde{y}(t_m + t_0(\vec{x}(\hat{t}_n)), \vec{x}(\hat{t}_n))\}, \tag{2.33}$$

where, $t_m = (m - 1)/f_t - T_t/2$ for $m = 1, \dots, M$ and $\hat{t}_n = (n - 1)/f_{\hat{t}}$ for $n = 1, \dots, N$. The

number of samples in fast and slow time will be $M = \lfloor f_t T_t \rfloor$ and $N = \lfloor f_t T_t \rfloor$, respectively.

2.2.7 Discrete Observation Model

Before forming a SAR image we must first define a discrete spatial grid onto which the image will be formed. In this section we will assume that the scene lies on a flat plane at $y_3 = 0$, however, equivalent results could be derived for images on other smooth surfaces. We will also choose the spatial grid to be independent in each axis y_1 and y_2 .

In order to define a spatial grid for the image we first define its radius in terms of y_1 and y_2 , which are given by

$$2L_{y_1} = \max \{ |y_{a1} - y_{b1}| : \vec{\mathbf{x}}_a \in \mathcal{X}, \vec{\mathbf{x}}_b \in \mathcal{X}, \vec{\mathbf{y}}_a \in \mathcal{Y}_{\vec{\mathbf{x}}_a} \cup \mathcal{Y}_{\vec{\mathbf{x}}_b}, \vec{\mathbf{y}}_b \in \mathcal{Y}_{\vec{\mathbf{x}}_a} \cup \mathcal{Y}_{\vec{\mathbf{x}}_b} \} \quad (2.34a)$$

$$2L_{y_2} = \max \{ |y_{a2} - y_{b2}| : \vec{\mathbf{x}}_a \in \mathcal{X}, \vec{\mathbf{x}}_b \in \mathcal{X}, \vec{\mathbf{y}}_a \in \mathcal{Y}_{\vec{\mathbf{x}}_a} \cup \mathcal{Y}_{\vec{\mathbf{x}}_b}, \vec{\mathbf{y}}_b \in \mathcal{Y}_{\vec{\mathbf{x}}_a} \cup \mathcal{Y}_{\vec{\mathbf{x}}_b} \} \quad (2.34b)$$

These radii are half the largest distance between scene elements that are in the antenna beam, in each direction.

Due to the limited aperture length and the limited chirp bandwidth, the received signals only contain significant energy in a limited region of the spatial Fourier domain of the reflectivities, therefore, we define our SAR image to have an approximately limited spatial Fourier support. The bandwidth of this limited spatial Fourier support will define the sample spacing of the image's spatial grid. The minimum sampling rate for the image's spatial grid in y_1 and y_2 are approximately given by:

$$\begin{aligned} f_{y_{1\min}} &\approx \frac{1}{2\pi} \max \left\{ \left| k_u (t - t_0) (\sin(\phi(\vec{\mathbf{y}}_a - \vec{\mathbf{x}}_a)) \cos(\theta(\vec{\mathbf{y}}_a - \vec{\mathbf{x}}_a)) - \right. \right. \\ &\quad \left. \left. \sin(\phi(\vec{\mathbf{y}}_b - \vec{\mathbf{x}}_b)) \cos(\theta(\vec{\mathbf{y}}_b - \vec{\mathbf{x}}_b))) \right| : \right. \\ &\quad \left. \vec{\mathbf{x}}_a \in \mathcal{X}, \vec{\mathbf{x}}_b \in \mathcal{X}, \vec{\mathbf{y}}_a \in \mathcal{Y}_{\vec{\mathbf{x}}_a} \cup \mathcal{Y}_{\vec{\mathbf{x}}_b}, \vec{\mathbf{y}}_b \in \mathcal{Y}_{\vec{\mathbf{x}}_a} \cup \mathcal{Y}_{\vec{\mathbf{x}}_b}, t - t_0 \in \left[-\frac{T_s}{2}, \frac{T_s}{2} \right] \right\} [\text{samples / metre}] \end{aligned} \quad (2.35a)$$

$$\begin{aligned} f_{y_{2\min}} &\approx \frac{1}{2\pi} \max \left\{ \left| k_u (t - t_0) (\sin(\phi(\vec{\mathbf{y}}_a - \vec{\mathbf{x}}_a)) \sin(\theta(\vec{\mathbf{y}}_a - \vec{\mathbf{x}}_a)) - \right. \right. \\ &\quad \left. \left. \sin(\phi(\vec{\mathbf{y}}_b - \vec{\mathbf{x}}_b)) \sin(\theta(\vec{\mathbf{y}}_b - \vec{\mathbf{x}}_b))) \right| : \right. \\ &\quad \left. \vec{\mathbf{x}}_a \in \mathcal{X}, \vec{\mathbf{x}}_b \in \mathcal{X}, \vec{\mathbf{y}}_a \in \mathcal{Y}_{\vec{\mathbf{x}}_a} \cup \mathcal{Y}_{\vec{\mathbf{x}}_b}, \vec{\mathbf{y}}_b \in \mathcal{Y}_{\vec{\mathbf{x}}_a} \cup \mathcal{Y}_{\vec{\mathbf{x}}_b}, t - t_0 \in \left[-\frac{T_s}{2}, \frac{T_s}{2} \right] \right\} [\text{samples / metre}], \end{aligned} \quad (2.35b)$$

We can now define the sample rates $f_{y_1} > f_{y_{1\min}}$ and $f_{y_2} > f_{y_{2\min}}$ and use them to define the

three dimensional spatial grid as

$$\vec{\mathbf{y}}_{kl} = \left[\frac{l-1}{f_{y_1}} + y_{01} - L_{y_1}, \frac{k-1}{f_{y_2}} + y_{02} - L_{y_2}, 0 \right]^T, \quad (2.36)$$

for, $k = 1, \dots, M'$ and $l = 1, \dots, N'$, where $M' = \lfloor f_{y_2} 2L_{y_2} \rfloor$ and $N' = \lfloor f_{y_1} 2L_{y_1} \rfloor$.

If we use a discrete SAR image model in Eq 2.33 we get the following discrete SAR observation model.

$$y_{mn} \approx w_m \sum_{k=1}^{M'} \sum_{l=1}^{N'} a_{kln} b_\theta(\vec{\mathbf{y}}_{kl}, \vec{\mathbf{x}}_n) b_\phi(\vec{\mathbf{y}}_{kl}, \vec{\mathbf{x}}_n) x_{kl} \exp(-jk_u(t_m)u_{kln}), \quad (2.37)$$

where,

- $b_\theta(\vec{\mathbf{y}}_{kl}, \vec{\mathbf{x}}_n)$ and $b_\phi(\vec{\mathbf{y}}_{kl}, \vec{\mathbf{x}}_n)$ model the antenna beam,
- $u_{kln} = \|\vec{\mathbf{y}}_{kl} - \vec{\mathbf{x}}_n\| - u_0(\vec{\mathbf{x}}_n)$ is the distance between each sample in the image to each platform position minus the distance between the scene centre at the corresponding platform position,
- $a_{kln} = (4\pi(u_0(\vec{\mathbf{x}}_n) + u_{kln}))^{-2}$ models the RF wave energy loss due to spreading in three-dimensional space and
- $w_m = -\frac{1}{2}w(t_m)(\omega_0 + 2\alpha t_m)^2$ models the frequency dependency of scattering predicted by our scattering model.

This can be written in matrix form as

$$\mathbf{Y} = h(\mathbf{X}), \quad (2.38)$$

where, $h : \mathbb{C}^{M' \times N'} \rightarrow \mathbb{C}^{M \times N}$ is the linear map in Eq. 2.37, $\mathbf{X} \in \mathbb{C}^{M' \times N'}$ is the SAR image and $\mathbf{Y} \in \mathbb{C}^{M \times N}$ is the phase history. Using this model, the problem of reconstructing a SAR image involves computing an estimate of \mathbf{X} , from the measurements \mathbf{Y} .

2.3 Matched Filter based Image Formation

In this section we will consider the standard SAR image formation algorithms that are based on approximations of a two-dimensional matched filter. The matched filter for the forward observation model $h(\cdot)$ is given by its adjoint $h^H(\cdot)$. The direct computation of $h^H(\cdot)$ which we define as $g_{mf}(\cdot)$ can be written as

$$\begin{aligned} \hat{\mathbf{X}} &= g_{mf}(\mathbf{Y}) \\ &= \left\{ \sum_{n=1}^N b_\theta(\vec{\mathbf{y}}_{kl}, \vec{\mathbf{x}}_n) b_\phi(\vec{\mathbf{y}}_{kl}, \vec{\mathbf{x}}_n) a_{kln} \sum_{m=1}^M w_m y_{mn} \exp(jk_u(t_m)u_{kln}) \right\}_{kl}. \end{aligned} \quad (2.39)$$

The formed image, $\hat{\mathbf{X}}$, can be computed in this direct manner in $\mathcal{O}(M'N'MN)$ operations. This order of operations is much too high for any realistically sized problems. Therefore, reduced complexity algorithms are used to approximate the adjoint.

2.3.1 Back-projection Algorithm

The BP algorithm reduces the complexity of computing the adjoint by observing that it can be written as

$$\hat{\mathbf{X}} = g_{\text{bp}}(\mathbf{Y}) = \left\{ \sum_{n=1}^N b_{\theta}(\vec{\mathbf{y}}_{kl}, \vec{\mathbf{x}}_n) b_{\phi}(\vec{\mathbf{y}}_{kl}, \vec{\mathbf{x}}_n) a_{kln} p_{kln} \right\}_{kl}, \quad (2.40)$$

where,

$$p_{kln} = \sum_{m=1}^M w_m y_{mn} \exp(jk_u(t_m) u_{kln}). \quad (2.41)$$

and that the elements of a matrix $\mathbf{P}_n = \{p_{kln}\}_{kl}$ can be approximated using a fast non-uniform DFT algorithm. Traditional, zero padding and linear interpolation has been used to approximate \mathbf{P}_n in $\mathcal{O}(M \log(M) + M'N')$ operations. Modern NFFT algorithms can also be used to approximate \mathbf{P}_n with a specified accuracy [54]. They have a complexity order which depends on the approximation error. To compute \mathbf{P}_n with these algorithms requires $\mathcal{O}((M \log(M) + M'N' \log(1/\epsilon)))$ operations, where ϵ is the approximation error. Using this approximation for \mathbf{P}_n , $\hat{\mathbf{X}}$ can be approximated in $\mathcal{O}(M'N'N \log(1/\epsilon))$ operations.

2.3.2 Polar Format Algorithm

The PFA further reduces the complexity of computing the adjoint of the observation model by making a far-field approximation [76]. A far-field approximation assumes that the wavefront is well approximated by a plane wave and therefore the distances in the range direction can be given as,

$$\begin{aligned} u_{kln} &\approx \sin \theta_0(\vec{\mathbf{x}}) \left(\left(\frac{k-1}{f_{y1}} - L_{y1} \right) \cos(\phi_0(\vec{\mathbf{x}}_n)) + \left(\frac{l-1}{f_{y2}} - L_{y2} \right) \sin(\phi_0(\vec{\mathbf{x}}_n)) \right) \\ &= u_{kln}^{\text{ff}}, \end{aligned} \quad (2.42)$$

which is an inner product between the image element locations and the normalised vector between the platform position and the scene centre. Using the approximation u_{kln}^{ff} for u_{kln} and by ignoring the beam pattern, we get the following approximation for the adjoint.

$$\hat{\mathbf{X}} = g_{\text{pfa}}(\mathbf{Y}) = \left\{ \sum_{n=1}^N \sum_{m=1}^M w_m y_{mn} \exp(jk_u(t_m) u_{kln}^{\text{ff}}) \right\}_{kl}. \quad (2.43)$$

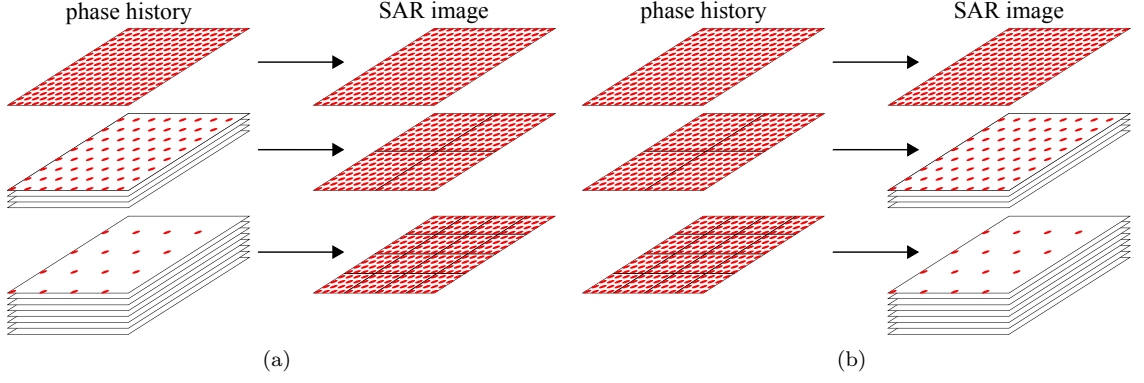


Figure 2.4: Decomposition in the fast BP algorithms: (a) Decomposition in the decimation-in-phase-history algorithm and (b) Decomposition in the decimation-in-image algorithm.

This summation is a two-dimensional non-uniform DFT. Like the one-dimensional case in the BP algorithm, the two-dimensional non-uniform DFT in the PFA has been traditionally approximated using zero padding and linear interpolation. This requires $\mathcal{O}(M'N' \log(\max\{M', N'\}))$ operations. It can also be approximated using a two-dimensional NFFT algorithm in $\mathcal{O}(M'N' \log(\max\{M', N'\}) + MN \log(1/\epsilon))$ operations.

2.3.3 Fast Back-projection Algorithms

When the far-field approximation is not suitable, it is still desirable to have an algorithm with a smaller complexity than the BP algorithm. The RMA is an example of an algorithm that does not make the far-field approximation, however, like the PFA, it ignores the beam pattern. The RMA can approximate the adjoint in $\mathcal{O}(MN \log(\max\{M, N\}))$ operations. The RMA is limited however to linear apertures and also must assume that the scene terrain is flat.

Fast BP algorithms, on the other hand, do not make the far-field approximation and can accommodate beam patterns, non-linear apertures and non-flat scene terrains. They approximate the adjoint in $\mathcal{O}(MN \log(\max\{M, N\}))$ operations [89, 133, 136]. They achieve this by recursively decimating the phase history and splitting the image grid at each stage of recursion. At the final stage of recursion, the BP algorithm is performed on a number of decimated phase histories to produce each segment of the final image. This can be seen to be analogous with the decimation-in-frequency FFT algorithms. In this section we will show why this decimation is possible and describe an implementation of this type of fast decimation-in-phase-history BP algorithm. We will also show how we can equivalently produce a fast decimation-in-image BP algorithm.

Fast Decimation-in-phase-history Back-Projection Algorithm

The decomposition strategy used in the fast decimation-in-phase-history BP algorithm, which uses a quad-tree structure, is visualised in Fig. 2.4(a). At the top of the figure we have the

original phase history and its corresponding image grid. At the first stage of decomposition, seen on the second line of the figure, the image grid is split into four even segments. The phase history is accordingly decimated into four new phase histories with each corresponding to one of the four image segments. At the second stage, this decomposition is repeated so there is now 16 image grid segments and there are 16 corresponding decimated phase histories. At the final stage of decomposition, the BP algorithm is used to compute the value of the pixels in each segment using only their corresponding decimated phase history.

Decimating in the phase history is possible because the required slow and fast time sampling rates are dependent on the size of the image segment. Therefore, a small image segment does not require the phase history to be sampled at as high a rate as for the entire image. In order to provide a simple expression to describe the relationship between the image segment size and the required phase history sampling rates, we will use a far-field approximation. It is important to note that this approximation is not being used in the same way as in the PFA, here, it is only used to analyse the algorithm. As stated earlier the far-field approximation assumes that the scene is in the far-field and hence the wavefront is planar and therefore the distance in the range direction is approximately given by Eq. 2.42. Under the fast-field approximation we can provide a bound for the minimum sampling rate for the phase history slow and fast times with respect to the size of the image segment, which is given by

$$f_{t_{\min}} \leq \frac{4\alpha}{\pi c_0} \sin(\theta_0) \sqrt{L_{y_1}^2 + L_{y_2}^2} \quad (2.44a)$$

$$f_{\hat{t}_{\min}} \leq \frac{2 \|\vec{v}\| k_u \left(\frac{T_s}{2}\right)}{\pi u_0} \sin(\theta_0) \sqrt{L_{y_1}^2 + L_{y_2}^2}. \quad (2.44b)$$

where, $f_{t_{\min}}$ is derived from Eq. (2.29) with $L_u(\vec{x}) = \sin(\theta_0) \sqrt{L_{y_1}^2 + L_{y_2}^2}$ and $f_{\hat{t}_{\min}}$ is from Eq. (2.32), where, $\sin(\frac{\Phi}{2}) \approx \sqrt{L_{y_1}^2 + L_{y_2}^2}/u_0$. and $\sin(\theta_0 - \frac{\Theta}{2}) \approx \sin(\theta_0)$. Importantly, both sampling rates are linearly dependent on the SAR image radius.

The dependency between the required phase history sampling rates and the image segment size is demonstrated in Fig. 2.5 and Fig. 2.6 using simulated phase history data. In this simulation, two phase histories were generated, one from a scene with a radius of 70.71 metres and the other from a scene with a radius of 35.36 metres. The first phase history has a fast-time bandwidth of approximately 22 MHz and a slow-time bandwidth of approximately 3.5 Hz. The second phase history has a fast-time bandwidth of approximately 11 MHz and a slow-time bandwidth of approximately 1.75 Hz. This simulation shows that the bandwidth of the phase history data, and hence the required sampling rates, approximately increases linearly with the size of the scene.

The approximately linear dependency is used in the fast decimation-in-phase-history BP algorithm. When the image is split into four image segments, the required sampling rate of the phase history is halved. Therefore the phase history for this image segment can be deci-

mated. To do this, the dechirp centre of the phase history must first be correct so that the new dechirp centre is located at the centre of the image segment. This will require $\mathcal{O}(MN)$ operations. The phase history may then be low-pass filtered and down-sampled by a half, in slow and fast times, to decimate the phase history. This will also require $\mathcal{O}(MN)$ operations. Therefore the number of operations required at each stage of decomposition is $\mathcal{O}(MN)$. To repeat this decomposition, until each phase history contains just a single element, will require $\mathcal{O}(MN \log(\max\{M, N\}))$ operations. For this completely decomposed problem, the number operations required to perform the BP algorithm for all of the image segments will be $\mathcal{O}(M'N')$. Therefore, the complexity of the fast decimation-in-phase-history BP algorithm is $\mathcal{O}(MN \log(\max\{M, N\}))$.

The pseudo code for a fast decimation-in-phase-history BP algorithm with a single stage of decomposition is given in Algorithm 1.

Algorithm 1 Fast decimation-in-phase-history BP algorithm $\hat{\mathbf{X}} = g_{\text{fbp}}(\mathbf{Y})$

Input: \mathbf{Y}

Output: $\hat{\mathbf{X}}$

$\mathbf{Y} \leftarrow \text{diag}(\mathbf{w})\mathbf{Y}$

$\hat{\mathbf{X}} \leftarrow \mathbf{0}_{M', N'}$

$L_{y_1} \leftarrow L_{y_1}/2$

$L_{y_2} \leftarrow L_{y_2}/2$

for $a = 0, 1$ **do**

for $b = 0, 1$ **do**

 {ADJUST DECHIRP CENTRE}

$\vec{\mathbf{y}}'_0 \leftarrow \vec{\mathbf{y}}_0 + \{(a - 1/2)L_{y_1}, (b - 1/2)L_{y_2}, 0\}^T$

$\mathbf{Y}' \leftarrow \{y_{mn} \exp(jk_u(t_m)(\|\vec{\mathbf{y}}'_0, \vec{\mathbf{x}}_n\| - \|\vec{\mathbf{y}}_0, \vec{\mathbf{x}}_n\|))\}_{m=1, n=1}^{M, N}$

 {DOWNSAMPLING}

$\mathbf{Y}' \leftarrow \left\{ \sum_{m'=1}^{2M_h+1} \sum_{n'=1}^{2N_h+1} h_{m'n'} y'_{(2m-1-M_h+m')(2n-1-N_h+n')} \right\}_{m=1, n=1}^{M/2, N/2}$

 {BACK-PROJECTION ALGORITHM}

for $n = 1, \dots, N/2$ **do**

$\vec{\mathbf{x}}'_n \leftarrow \vec{\mathbf{x}}_{2n-1}$

$\mathbf{P} \leftarrow \text{nfft}_n(\mathbf{Y}')$

for $k = aM'/2 + 1, \dots, (a+1)M'/2$ **do**

for $l = bN'/2 + 1, \dots, (b+1)N'/2$ **do**

$\hat{x}_{kl} \leftarrow \hat{x}_{kl} + b_\theta(\vec{\mathbf{y}}_{kl}, \vec{\mathbf{x}}'_n) b_\phi(\vec{\mathbf{y}}_{kl}, \vec{\mathbf{x}}'_n) a_{kl(2n-1)} p_{kl}$

end for

end for

end for

end for

end for

$\mathbf{h} \in \mathbb{C}^{M_h \times N_h}$ is a two-dimensional low pass filter and

$$\text{nfft}_n(\mathbf{Y}') \approx \sum_{m=1}^M y'_{mn} \exp(jk_u(t_m)u_{kln}). \quad (2.45)$$

Fast Decimation-in-image Back-Projection Algorithm

The decomposition strategy used in the fast decimation-in-image BP algorithm using a quad-tree structure is visualised in Fig. 2.4(b). At the top of the figure we have the original phase history and its corresponding image grid. At the first stage of decomposition, seen on the second line of the figure, the phase history is split into four even segments and the image is decimated into four new phase histories, with each corresponding to one of the four image segments. At the second stage, this decomposition is repeated so there is now 16 phase history grid segments and there are 16 corresponding decimated images. At the final stage of decomposition, the BP algorithm is used to compute an image for each segment of the phase history. The images can then be recursively upsampled and combined to produce a single image.

Decimating in the image is possible because the sampling rate of the scene is dependent on the period of the slow and fast times. In order to provide a simple expression to describe this relationship we will again make the far field approximation and also assume that aperture is in the y_2 direction and the slow and fast times are small enough such that the spatial Fourier support is approximately rectangular. Again, it is important to note that these approximations are only used to analyse the algorithm. Under these approximations we can provide a bound for the minimum sampling rate for the image grid, which are given by

$$f_{y_1 \min} \leq \frac{2\alpha}{\pi c_0} \sin(\theta_0) T_t \quad (2.46a)$$

$$f_{y_2 \min} \leq \frac{\|\vec{\nabla}\| \omega_0}{\pi c_0 u_0} \sin(\theta_0) T_t. \quad (2.46b)$$

In this scenario both sampling rates are linearly dependent on the SAR image radius. For the more general case where these approximations do not apply we do not have a linear dependency, however, it is still possible to have a practical decomposition strategy. This is demonstrated in Fig. 2.7 using a simulated phase history data. In the simulation, the phase history has been split into four segments. The BP algorithm was used to generate four images, one from each of the phase histories. An image was also created from the full phase history. For the complete phase history, the required sampling rates are approximately 1.75 samples per metre in y_1 and 2.2 samples per metre in y_2 . For the phase history segments in Fig. 2.7(c) and Fig. 2.7(e), the required sampling rates are approximately 0.9 samples per metre in y_1 and 0.7 samples per metre in y_2 . For the phase history segments in Fig. 2.7(d) and Fig. 2.7(f), the required sampling rates are approximately 1 samples per metre in y_1 and 1.1 samples per metre in y_2 . This simulation shows that the required sampling rate for the image grid approximately increases linearly with the period of the slow and fast times.

This property is used in the fast decimation-in-image BP algorithm. When the phase history is split into four image segments, the required sampling rate of the image is approximately halved, therefore, the image grid can be decimated. If the phase history is recursively split

such that each phase history segment contains just a single element, the number of operations required to perform the BP algorithm for all the images will be $\mathcal{O}(MN)$. The next stage of the fast decimation-in-image BP algorithm is to combine the images. This combination can be done recursively. At each stage groups of four images, which were formed from adjacent phase history segments, are combined. To do this each image must first be upsampled by a factor of two in y_1 and y_2 . This can be done for all decimated images with $\mathcal{O}(M'N')$ operations. The images can then be combined. This procedure is repeated until there is just a single image. The number of operations required to combine all images into a single image will be $\mathcal{O}(MN \log(\max\{M, N\}))$ operations. Therefore the complexity of the fast decimation-in-image BP algorithm is $\mathcal{O}(MN \log(\max\{M, N\}))$.

The pseudo code for a fast decimation-in-image BP algorithm with a single stage the decomposition is given in Algorithm 2.

There are errors which are introduced by approximating the adjoint with a fast BP algorithm. In both algorithms, the main source of error is due to the decimation and upsampling of finite length data with finite length filters. Since the data (the phase history or the image) is finite length, any decimating filter or upsampling filter will have “border effects” which will produce errors. Since in practise a filter will be finite length, the filter will have associated stopband and passband ripples and a transition bandwidth, which will also introduce errors.

In the decimation-in-phase-history algorithm, since the decimation is performed on the phase history, the border effects and finite filter length errors will occur in the phase history domain. For the decimation-in-image algorithm, because upsampling is performed on images, the border effects and finite filter length errors will occur in the image domain.

To demonstrate the described errors, 4° of the “Gotcha Volumetric SAR Data Set, Version 1.0” (described in [30]) was used to form images using the BP algorithm as well as the two fast methods with one and three stages of decomposition. The resulting images are shown in Fig. 2.8. The filter used for decimating and upsampling, in both of the fast algorithms, was a 41 sample length low-pass Chebyshev filter with 100dB side-lobe attenuation.

The relative errors between the image formed using the BP algorithm and the other images are shown in Fig. 2.9. Due to the source of the errors, the relative errors are displayed in the wavenumber domain for the decimation-in-phase-history images and in the image domain for the decimation-in-image images. The relative error is computed for each element in an image as $\|\hat{x} - x\|_2 / \|x\|_2$, where x is an element from the reference BP image and \hat{x} is the corresponding element from fast BP image.

The results in Fig. 2.9(a), Fig. 2.9(c), demonstrate the errors in the images formed using the fast decimation-in-image BP algorithms. With one decimation stage the errors within the image are approximately -100 dB and the border effects are highly concentrated on the edge of the image. With three stages, the error within the image has increased to approximately -90 dB and the border effects have also significantly increased.

Algorithm 2 fast decimation-in-image BP algorithm $\hat{\mathbf{X}} = g_{\text{fbp}}(\mathbf{Y})$

Input: \mathbf{Y}

Output: $\hat{\mathbf{X}}$

$\mathbf{Y} \leftarrow \text{diag}(\mathbf{w})\mathbf{Y}$

$\hat{\mathbf{X}} \leftarrow \mathbf{0}_{M',N'}$

for $a = 0, 1$ **do**

for $b = 0, 1$ **do**

 {SPLIT PHASE-HISTORY}

$\mathbf{Y}' \leftarrow \{y_{(aM/2+m)(bN/2+n)}\}_{m=1, n=1}^{M/2, N/2}$

$\vec{\mathbf{x}}' \leftarrow \{\vec{\mathbf{x}}_{bN/2+n}\}_{n=1}^{N/2}$

 {BACK-PROJECTION ALGORITHM}

for $n = 1, \dots, N/2$ **do**

$\hat{\mathbf{X}}' \leftarrow \mathbf{0}_{M'/2, N'/2}$

$\mathbf{P} \leftarrow \text{nfft}_n(\mathbf{Y}')$

for $k = 1, \dots, M'/2$ **do**

for $l = 1, \dots, N'/2$ **do**

$\vec{\mathbf{y}}' \leftarrow \vec{\mathbf{y}}_{(2k-1)(2l-1)}$

$\hat{x}'_{kl} \leftarrow \hat{x}_{kl} + b_\theta \left(\vec{\mathbf{y}}_{(2k-1)(2l-1)}, \vec{\mathbf{x}}_n \right) b_\phi \left(\vec{\mathbf{y}}_{(2k-1)(2l-1)}, \vec{\mathbf{x}}_n \right) a_{(2k-1)(2l-1)npkl}$

end for

end for

 {CENTRE IMAGE'S SPECTRAL SUPPORT}

$\vec{\mathbf{x}}_0 \leftarrow \vec{\mathbf{x}}_{\lceil N/2 \rceil + 1}$

$t_0 \leftarrow t_{\lceil M/2 \rceil + 1}$

$\hat{\mathbf{X}}' \leftarrow \left\{ \hat{x}'_{kl} \exp \left(-jk_u(t_0) \left(\left\| \vec{\mathbf{y}}_{(2k-1)(2l-1)} - \vec{\mathbf{x}}_0 \right\| - \left\| \vec{\mathbf{y}}_0 - \vec{\mathbf{x}}_n \right\| \right) \right) \right\}_{k=1, n=l}^{M'/2, N'/2}$

 {UPSAMPLING}

$\hat{\mathbf{X}}' \leftarrow \left\{ \text{if } k \wedge l \text{ are odd then } x'_{(k/2+1/2)(l/2+1/2)}, \text{ else } 0 \right\}_{k=1, n=l}^{M', N'}$

$\hat{\mathbf{X}}' \leftarrow \left\{ \sum_{k'=1}^{2M_h+1} \sum_{l'=1}^{2N_h+1} h_{k'l'} \hat{x}'_{(2k-1-M_h+k')(2l-1-N_h+l')} \right\}_{k=1, l=1}^{M', N'}$

 {COMBINE IMAGES}

$\hat{\mathbf{X}}' \leftarrow \left\{ \hat{x}'_{kl} \exp(jk_u(t_0) (\left\| \vec{\mathbf{y}}_{kl} \right\| - \left\| \vec{\mathbf{x}}_0 \right\| - \left\| \vec{\mathbf{y}}_0 - \vec{\mathbf{x}}_n \right\|)) \right\}_{k=1, n=l}^{M', N'}$

$\hat{\mathbf{X}} = \hat{\mathbf{X}} + \hat{\mathbf{X}}'$

end for

end for

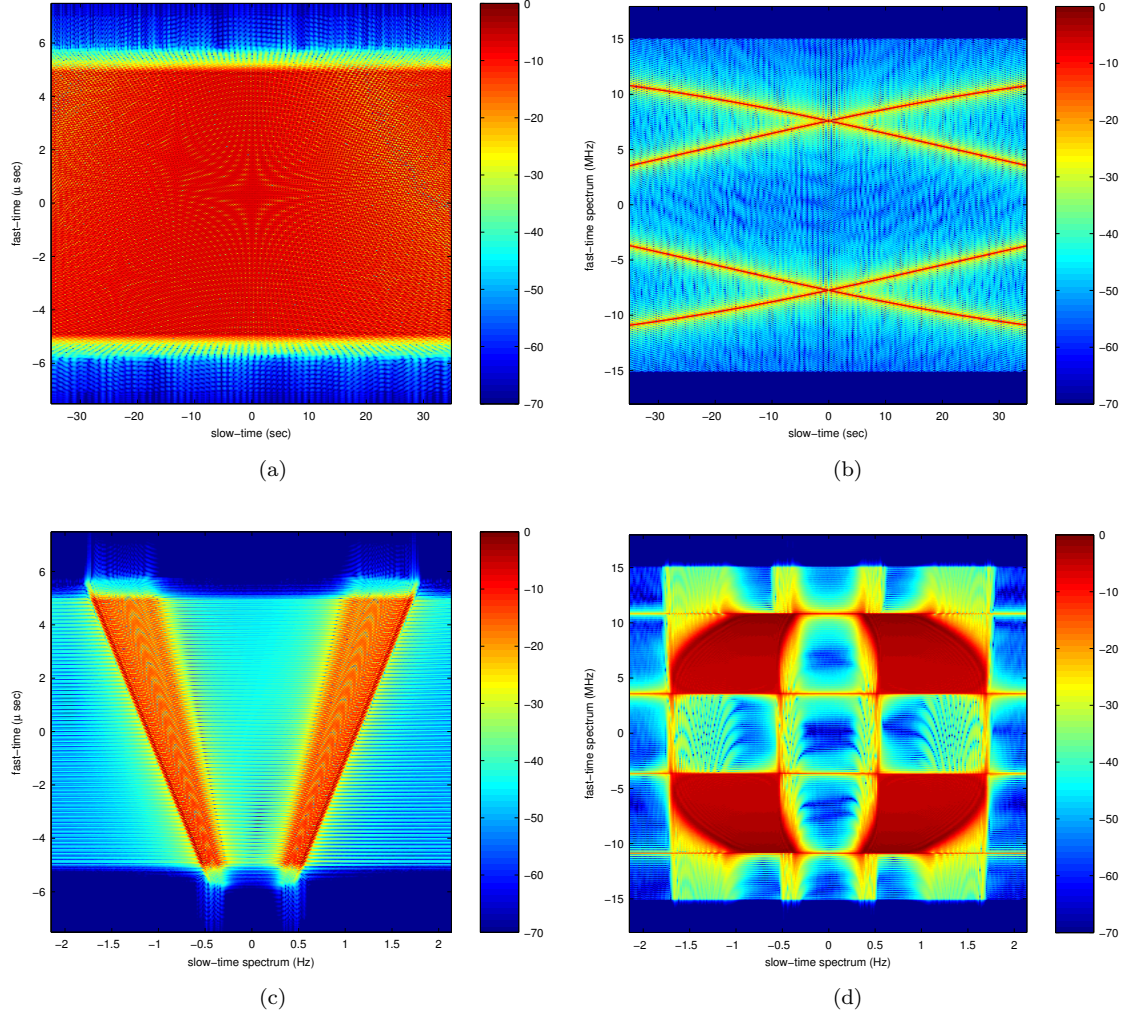


Figure 2.5: Simulated phase history from four targets located at $[50, 50, 0]^T$ m, $[-50, 50, 0]^T$ m, $[50, -50, 0]^T$ m and $[-50, -50, 0]^T$ m (relative to the scene centre). The system parameter are: carrier frequency $\omega_0/2\pi = 308$ MHz, chirp rate $\alpha/\pi = 32.4$ MHz/ μ s, chirp period $T = 10$ μ s, synthetic aperture $[7, -3.5, 7]^T$ km to $[7, 3.5, 7]^T$ km (relative to the scene centre) and platform velocity 100 m/s. (a) is the phase history in the fast time and the slow time. (b) is the phase history in the fast time spectrum and the slow time. (c) is the phase history in the fast time and slow time spectrum. (d) is the phase history in fast time spectrum and slow time spectrum.

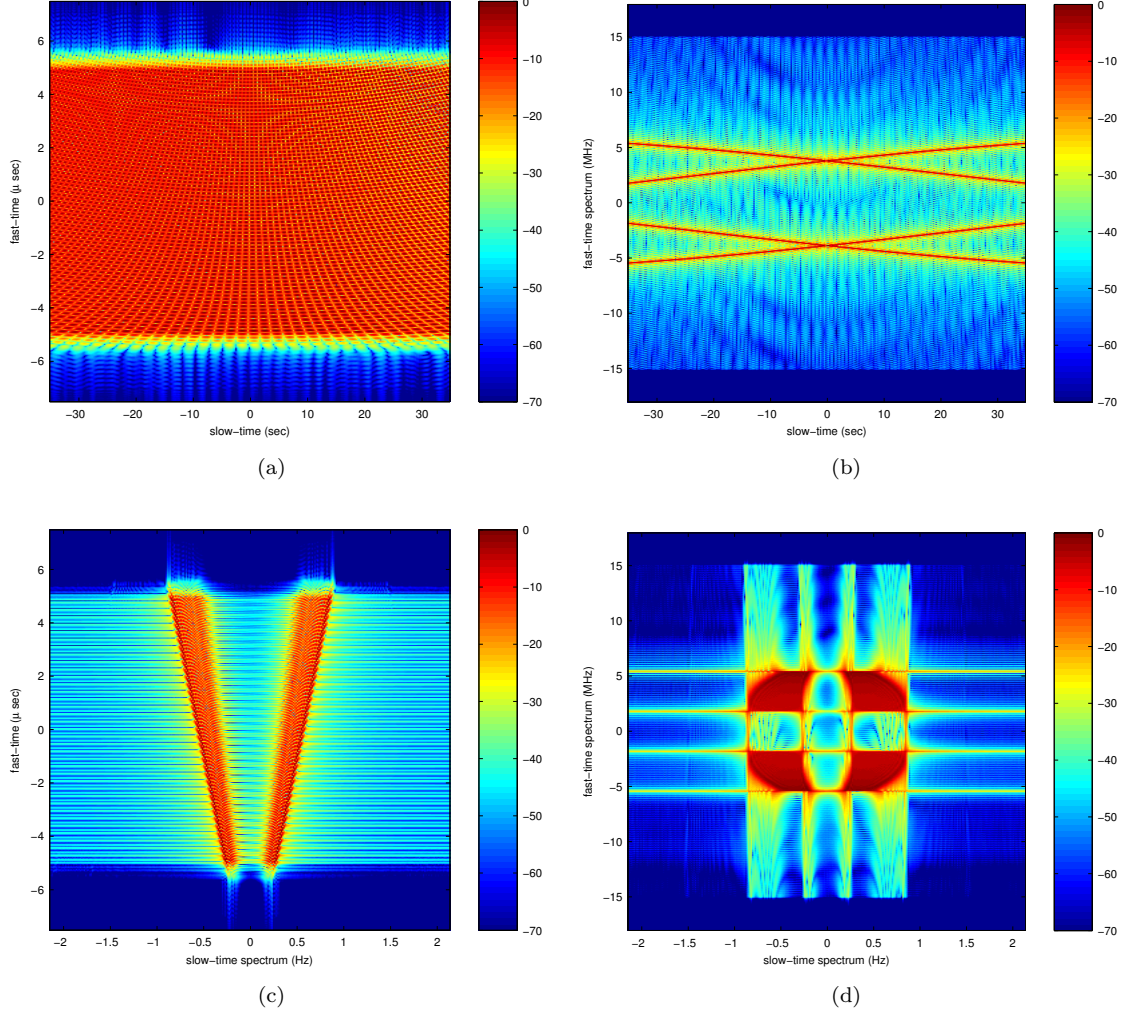


Figure 2.6: Simulated phase history from four targets located at $[25, 25, 0]^T$ m, $[-25, 25, 0]^T$ m, $[25, -25, 0]^T$ m and $[-25, -25, 0]^T$ m (relative to the scene centre). The system parameter are: carrier frequency $\omega_0/2\pi = 308$ MHz, chirp rate $\alpha/\pi = 32.4$ MHz/ μ s, chirp period $T = 10$ μ s, synthetic aperture $[7, -3.5, 7]^T$ km to $[7, 3.5, 7]^T$ km (relative to the scene centre) and platform velocity 100 m/s. (a) is the phase history in the fast time and the slow time. (b) is the phase history in the fast time spectrum and the slow time. (c) is the phase history in the fast time and slow time spectrum. (d) is the phase history in fast time spectrum and slow time spectrum.

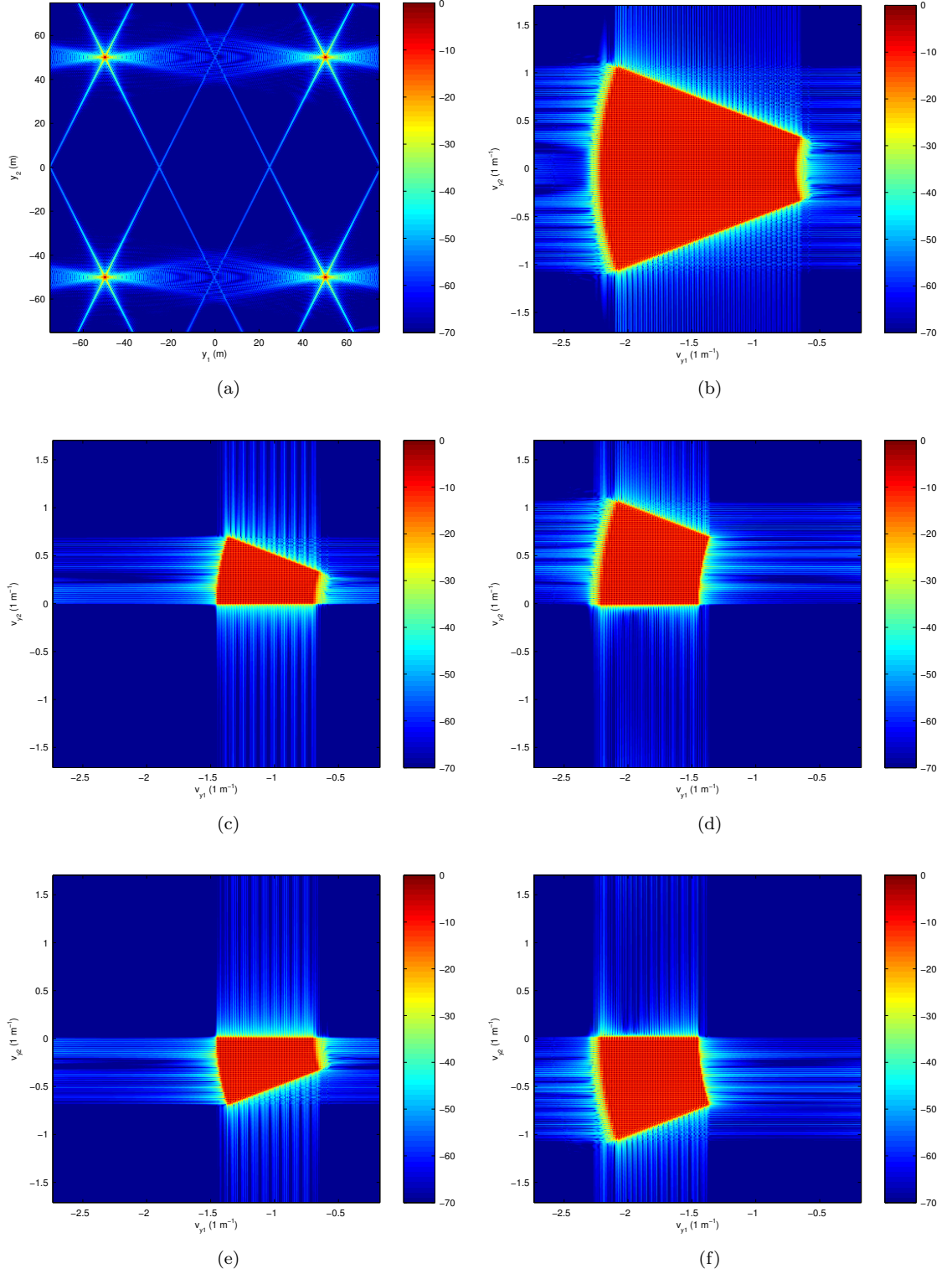


Figure 2.7: Images formed using the BP algorithm from a simulated phase history which was generated using four targets located at $[25, 25, 0]^T$ m, $[-25, 25, 0]^T$ m, $[25, -25, 0]^T$ m and $[-25, -25, 0]^T$ m (relative to the scene centre). The system parameter are: carrier frequency $\omega_0/2\pi = 308$ MHz, chirp rate $\alpha/\pi = 32.4$ MHz/ μs , chirp period $T = 10$ μs , synthetic aperture $[7, -3.5, 7]^T$ km to $[7, 3.5, 7]^T$ km (relative to the scene centre) and platform velocity 100 m/s. (a) is the resulting image and (b) is its spectrum. (c), (d), (e) and (f) are the spectra of images formed using four evenly sized segments of the full phase history.

Table 2.1: Image formation times (seconds)

N	BP	fast BP (dec.-in-image)	fast BP (dec.-in-phase-history)	PFA
256	18.26	4.75	4.64	0.90
512	140.22	18.77	18.74	3.24
1024	1120.96	77.18	76.98	13.15
2048	9052.47	318.43	317.36	69.15

For the fast decimation-in-phase-history BP algorithms, the results in Fig. 2.9(b), Fig. 2.9(d) demonstrate the errors in the formed images. With one decimation stage the errors within the image’s spectral support are approximately -50 dB and there are border effects. With three stages, the errors within the image’s spectral support have increased to approximately -40 dB and the edge effects have increased significantly. The errors associated with border effects, unlike in the decimation-in-image images, are not concentrated on the edge of the image’s spectral support. This is because targets have a spatially varying spectral support in a image formed using the BP algorithm.

Clearly in this example scenario, the fast decimation-in-image BP algorithm has a better performance, in terms of approximation error. This likely to be due to the circular aperture used in the Gotcha data set. The error performance of the decimation-in-phase-history algorithm could potentially be improved by interpolation the slow-time samples before they are decimated. This however would add an additional computational cost to the algorithm.

To demonstrate the computational advantages of the fast BP algorithms, the computational times for image formation were measured for different size phase histories and images. Images were formed using the BP algorithm, the PFA and the fast decimation-in-phase-history and decimation-in-image BP algorithms. Both the BP algorithm and the PFA made use of the NFFT algorithm in [68], with a interpolation kernel length of 24 samples which is what is suggested for double precision numerical accuracy. The image formation times were measured on a single core of a 2.5 GHz Intel Xeon processor with N^2 element images and N^2 element phase histories. The number of decomposition stages in the Fast BP algorithms was $\log_2 N - \log_2 64$. This number of stages was selected because through numerical simulation it was found to be a good trade off between algorithm “speed up” and approximation error. Table 2.1 shows the resulting image formation times in seconds.

For small images and phase histories, the fast BP algorithms only provides a modest speed up when compared to the BP algorithm. However, as the problem size grows, the speed up becomes more significant. It is also interesting to note that the ratio of image formation times between the PFA and the fast BP algorithms is approximately constant for all problem sizes. Since both algorithms have the same theoretical order of operations, this is an expected result. It is also worth noting that the BP algorithm and the PFA were implemented in C code while the decimation and upsampling code of the Fast BP algorithms were implemented in Matlab

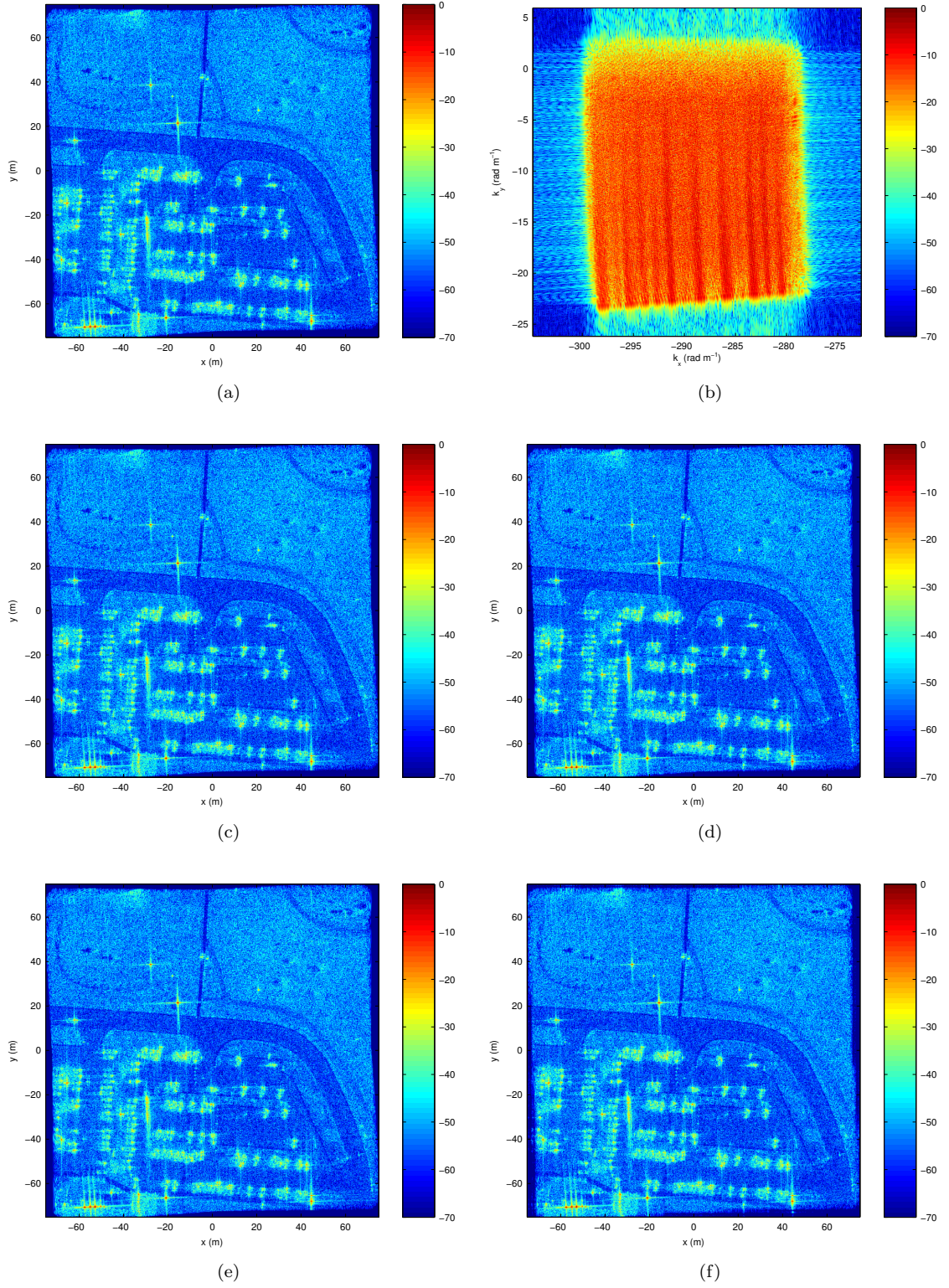


Figure 2.8: Images formed using the HH polarisation with angles $1 - 4^\circ$ of the eighth pass of the Gotcha data set. The images contain 768×768 pixels. The antenna beamwidths were limited to a 1.15° azimuth angle and a 0.57° polar angle. (a) was formed using the BP algorithm and (b) is its wavenumber spectrum. (c) was formed using the fast decimation-in-phase-history BP algorithm with one decomposition stage. (d) was formed using the fast decimation-in-image BP algorithm with one decomposition stage. (e) was formed using the fast decimation-in-phase-history BP algorithm with three decomposition stages. (f) was formed using the fast decimation-in-image BP algorithm with three decomposition stages.

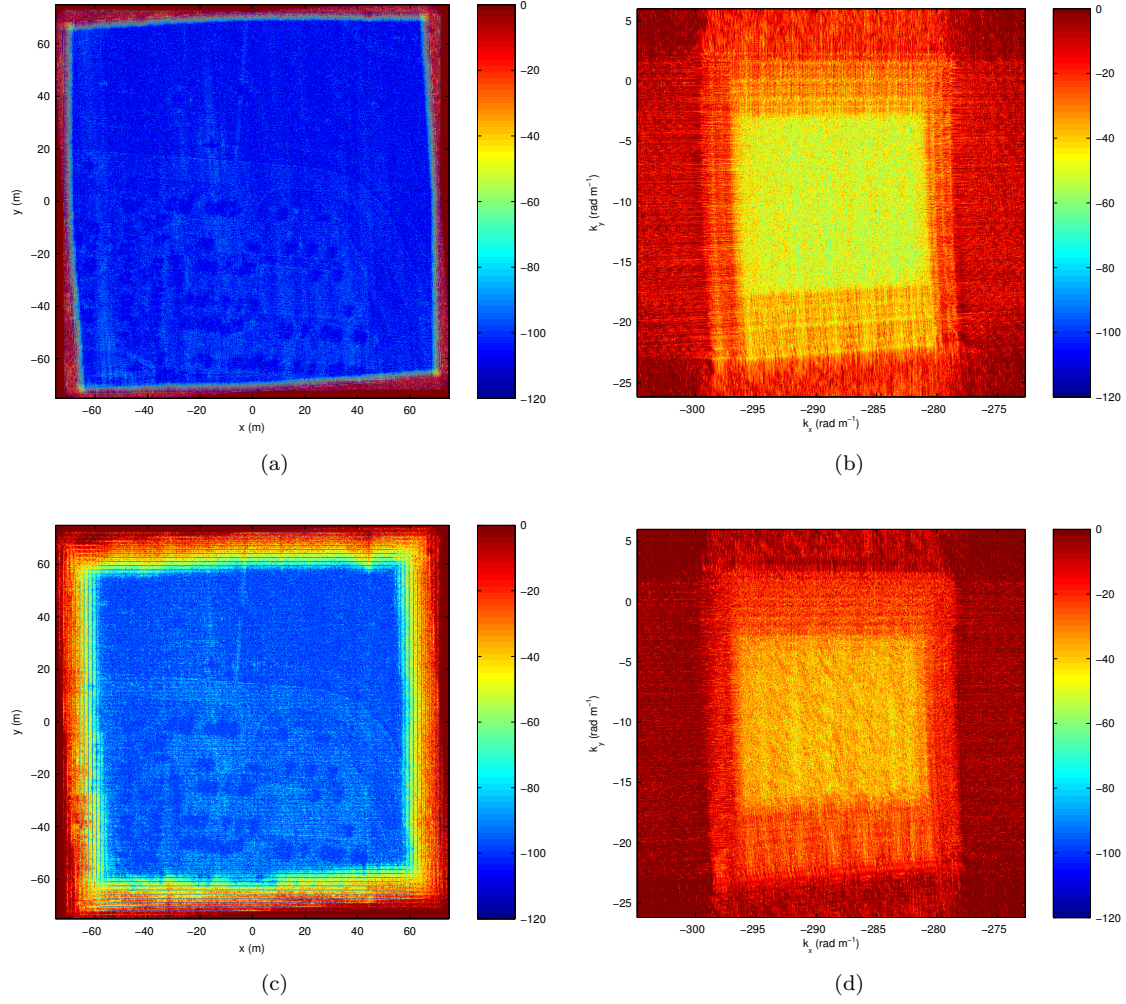


Figure 2.9: Relative errors in the Fast BP algorithms with respect to the BP algorithm. (a) is the relative error in the image in Fig. 2.8(d). (b) is the relative error in the wavenumber spectrum of the image in Fig. 2.8(c). (c) is the relative error in the image in Fig. 2.8(f). (d) is the relative error in the wavenumber spectrum of the image in Fig. 2.8(e).

script. If this code was ported to C code, one would expect some additional image formation time reduction, ideally close to the same speed as the PFA.

2.4 Summary

In this section we have developed a discrete SAR observation model and shown how standard image formation algorithms can be seen to be an approximation of a matched filter based on this model. Fast BP algorithms have been investigated and a novel fast BP algorithm has been proposed. Fast BP algorithms are important for new modalities of SAR, such as UWB SAR. The proposed fast decimation-in-image BP algorithm provides a similar level of speed up to existing algorithms, however, it has other advantages. Firstly, the errors introduced by the algorithm are concentrated on the edges of the image. This region usually contains the smallest amount of energy in the image due to the antenna beam pattern. Therefore, making the errors less significant. Also, since decimation and upsampling is most easily performed on a uniform grid, if the aperture is non-linear or is irregularly sampled, decimation-in-phase-history algorithms must first interpolate onto a grid before decimation. This is not required for decimation-in-image algorithms because the image grid is defined to be uniform. This could be a significant advantage for 3D SAR, where the multiple aperture passes will not be uniformly distributed in altitude. A mixed decimation strategy could also be used to reduce the edge effects, where, decimation could occur in both domains.

Chapter 3

Iterative Image Formation

3.1 Introduction

With a linear observation model for a SAR system it is possible to consider the SAR image formation as an inversion problem, instead of using an approximation of a matched filter to form the image. Using the linear observational model developed in Chap. 2, in its discrete form, the formation of an image is a inversion problem of the linear observational model

$$\mathbf{Y} = h(\mathbf{X}), \quad (3.1)$$

where, $\mathbf{Y} \in \mathbb{C}^{M \times N}$ is the phase history with M range and N cross-range measurements, $\mathbf{X} \in \mathbb{C}^{M' \times N'}$ is the SAR image and $h(\cdot)$ is the discrete linear observational model.

In many inversion problems, where the number of measurements is not equal to the dimensional of the signal, the pseudoinverse $h^\dagger(\cdot)$ of the observational model $h(\cdot)$ is used to invert the system. The pseudoinverse is typically approximated using a filtered matched filter based algorithm.

When the linear observational model $h(\cdot)$ is rank deficient because of missing data, there is no unique solution of Eq. (3.6). Instead, there is a set of solutions \mathcal{X} that equally minimise Eq. (3.6). The pseudoinverse solution is the solution $\hat{\mathbf{X}} \in \mathcal{X}$ that minimises $\|\hat{\mathbf{X}}\|_F$. This solution amounts to assuming that the missing data are zeroes. Since filtered matched filter based algorithms approximate this solution, they also assume that the missing data are zeroes. This assumption produces undesirable artifacts that may drastically reduce the quality of the image and make further exploitation impossible. In order to improve the image quality, further information must be included in the inversion problem. A standard signal processing approach is to solve a regularised least squares (LS) optimisation program of the form

$$\underset{\mathbf{X}}{\text{minimise}} \|\mathbf{Y} - h(\mathbf{X})\|_F^2 + \lambda P(\mathbf{X}), \quad (3.2)$$

where, $P(\mathbf{X})$ is a regularisation function. Typical examples of $P(\cdot)$ are ℓ_p and total variation (TV) norms. ℓ_p -norm regularisation functions with $p \leq 1$ have been considered for SAR in the context of superresolution [32, 33, 31, 61] and more recently for undersampled phase histories [34, 83, 111, 107, 108]. TV-norms have also been considered for SAR for speckle reduction [31, 107]. The use of ℓ_p norms has recently received considerable attention in the context of CS because it theoretically justifies their use (especially in the case $p = 1$), when the image can be modelled as collection of sparse targets. Motivated by CS, the intentional undersampling and redesign of radar waveforms has also been considered [8, 59, 73].

The field of CS has motivated the development of several fast solvers for the ℓ_1 regularised least squares problem (or one of its equivalent constrained optimisation forms) [63, 129, 41, 12, 13, 139]. Like conjugate gradient algorithms, these solvers require the iteration of the operators $h(\cdot)$ and $h^H(\cdot)$ and are therefore prohibitively slow unless fast implementations of the operators are available. In previous work on iterative algorithms for SAR, the far-field model has been used, therefore NFFT algorithms have been used to compute fast approximations of $h(\cdot)$ and $h^H(\cdot)$. However, in many of the applications where iterative algorithms may be useful, this approximation is not suitable.

In this chapter, a framework for SAR processing using iterative algorithms is proposed, which makes use of the fast BP algorithms from Chap. 2. In this framework, iterative algorithms can be used to reconstruct images with non-flat scene terrain from arbitrary trajectories within the near-field. Using techniques from the CS literature, which are modified for the SAR inversion problem, we demonstrate how the quality of an image formed from an undersampled phase history can be substantially improved using an iterative algorithm.

3.2 Fast (Re/Back)-projection Algorithms

In order to develop a gradient-based iterative algorithm to solve a LS or a regularised LS optimisation program there must be a fast means of computing $h(\mathbf{X})$ and $h^H(\mathbf{Y})$, for arbitrary $\mathbf{X} \in \mathbb{C}^{M' \times N'}$ and $\mathbf{Y} \in \mathbb{C}^{M \times N}$. In Chap. 2, fast algorithms for $h^H(\mathbf{Y})$ were proposed. The techniques from this chapter can also be used to produce a fast decimation-in-phase-history and decimation-in-image re-projection (RP) algorithm, which are fast approximations of the observational model. A fast decimation-in-phase-history RP algorithm has been proposed for use in iterative CT image formation algorithms [18].

The motivation for using fast RP and BP algorithms in iterative image formation algorithms, rather than NFFT algorithms, is the same motivating SAR applications, where the far-field and flat scene terrain approximation are not suitable, which leads to the development of fast BP algorithms. These approximations are especially unsuitable in an iterative algorithm where we wish to use additional information in terms of a signal model of the image.

A SAR scenario where the far-field approximation is not suitable occurs when the system has

a wide beamwidth. This is likely to occur in systems that use a low-frequency carrier because the antenna beamwidth is usually proportional to the wavelength of the transmitted signal. To demonstrate this scenario, a phase history was simulated from a scene containing four targets within a scene that is 1.4×1.4 km in size. A fast decimation-in-image BP algorithm and a PFA was used to form two images from the simulated data. These images are shown in Fig. 3.1. The image formed using the fast BP algorithm contains four point targets with their energy centred on the correct target locations. In PFA image, on the other hand, the four targets are not centred on the true target locations. Additionally, the energy of the targets is not concentrated on a single centre and instead is blurred. The reason for this blurring and translation of the targets can be understood by examining the wavenumber spectrum of the images. The wavenumber spectrum of the fast BP image shows that spectral support is spatially varying, each of the four targets has a spectral support that is unique. This is because the scene is large and therefore the angles of observation for each of the target are significantly different. The PFA algorithm implicitly approximates that each of the targets will have the same spectral support, which clearly in this case, is not a good approximation. The blurring of targets will also detrimentally effect the performance of CS based image formation algorithms that use a sparse image model.

Topographical variations of scene terrain can be incorporated into fast RP and BP algorithms using information provided by digital elevation maps (DEM) with no additional computational cost. This is not possible using other fast algorithms. When there is significant scene terrain variation, and if it is not considered in the image formation, the quality of the resulting image will be degraded [77]. The degradation will mean that the location and the relative distance between targets in the image will be inaccurate. Also, it may lead to a blurring of targets. To demonstrate this scenario, a phase history was simulated from a scene that had a non-flat scene terrain. Two images were generated from this phase history using a fast decimation-in-image BP algorithm. For one of the images, knowledge of the scene elevation was used, while, for the other image the scene terrain was assumed to be flat. The resulting images are shown in Fig. 3.2. For the image which assumed flat scene terrain, the four targets are displaced from their correct locations. For the image that used terrain information, the targets are at the correct locations. In this simulation the effect of the elevation is mainly a translation of the target in the scene, however, with larger scenes and terrain variation, targets will become blurred much like the target in Fig. 3.1(d). This will also effect the performance of CS based image formation algorithms.

3.3 Pseudoinverse Image Formation

The pseudoinverse can be written as

$$\hat{\mathbf{X}} = \mathbf{h}^H \left([\mathbf{h}\mathbf{h}^H]^\dagger (\mathbf{Y}) \right), \quad (3.3)$$

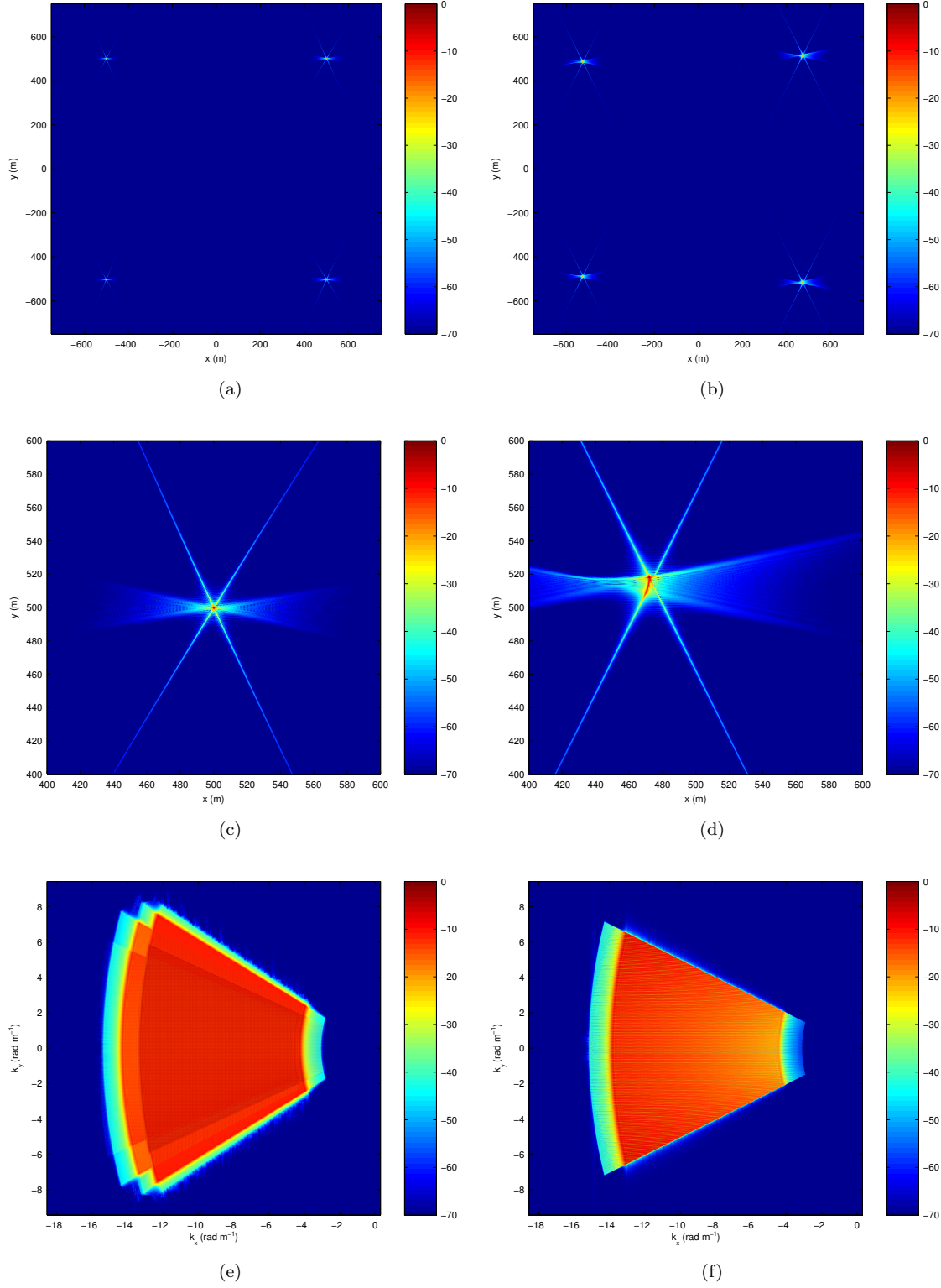


Figure 3.1: Images formed using a simulated phase history which was generated using four targets located at $[500, 500, 0]^T$ m, $[-500, 500, 0]^T$ m, $[500, -500, 0]^T$ m and $[-500, -500, 0]^T$ m (relative to the scene centre). The system parameters are: carrier frequency $\omega_0/2\pi = 308$ MHz, chirp rate $\alpha/\pi = 32.4$ MHz/ μs , chirp period $T = 10$ μs , synthetic aperture $[7, -3.5, 7]^T$ km to $[7, 3.5, 7]^T$ km (relative to the scene centre). (a) Image formed using the filtered BP Algorithm. (b) Image formed using the filtered PFA Algorithm. (c) Zoomed image in (a). (d) Zoomed image in (b). (e) wavenumber spectrum of image in (a). (f) wavenumber spectrum of image in (b).

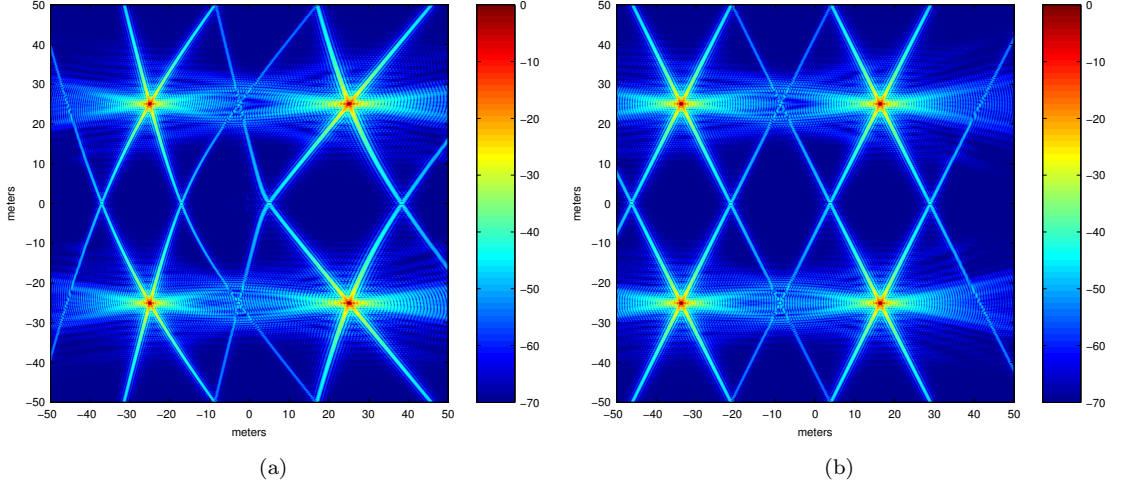


Figure 3.2: Images formed using a simulated phase history which was generated using four targets located at $[25, 25, 91.16]^T$ m, $[-25, 25, 91.16]^T$ m, $[25, -25, 91.16]^T$ m and $[-25, -25, 91.16]^T$ m (relative to the scene centre). The system parameters are: carrier frequency $\omega_0/2\pi = 308$ MHz, chirp rate $\alpha/\pi = 32.4$ MHz/ μ s, chirp period $T = 10$ μ s, synthetic aperture $[7, -3.5, 7]^T$ km to $[7, 3.5, 7]^T$ km (relative to the scene centre). (b) Image formed using the filtered BP algorithm without elevation knowledge. (a) Image formed using the filtered BP algorithm with elevation knowledge.

where, $[hh^H](\cdot)$ is the pseudoinverse of h ($h^H(\cdot)$). Due to the size of a typical SAR problem, $h^\dagger(\cdot)$ can not practically be computed, instead, it can only be approximated. Conventional filtered matched filter based algorithms, can be seen to be an approximation of this pseudoinverse. One commonly used filtered matched filter based image formation algorithm, which is motivated by filtered BP techniques in CT, is computed as

$$\hat{\mathbf{X}} = h^H(\mathbf{Q} \circ \mathbf{Y}) \quad (3.4)$$

where,

$$\mathbf{Q} = \text{diag} \left((\sin(\theta_0(\vec{\mathbf{x}}_n)))^{-1} (\omega_0 + 2\alpha(mT_s - T_t/2)) \right) \quad (3.5)$$

is a ramp filter [99] and $h^H(\cdot)$ is approximated using one of the algorithms discussed in Chap. 2. In this algorithm $[hh^H](\cdot)$ is approximated by an element-wise product of \mathbf{Q} and \mathbf{Y} .

Fig. 3.3 shows two images which were formed from a simulated phase history. The image in Fig. 3.3(a) was formed using the BP algorithm and the image in Fig. 3.3(b) was formed using a ramp filtered BP algorithm. The difference between the images is only minor. The filtered BP image has slightly reduced sidelobes. Unlike in the related problem of CT, filtering only provides minor improvements in the formed image, especially for narrow band systems.

Rather than approximating the pseudoinverse $h^\dagger(\cdot)$ with a filtered BP algorithm, an iterative algorithm can be used to approximate the pseudoinverse solution. If $h(\cdot)$ is full rank, the solution to the LS objective,

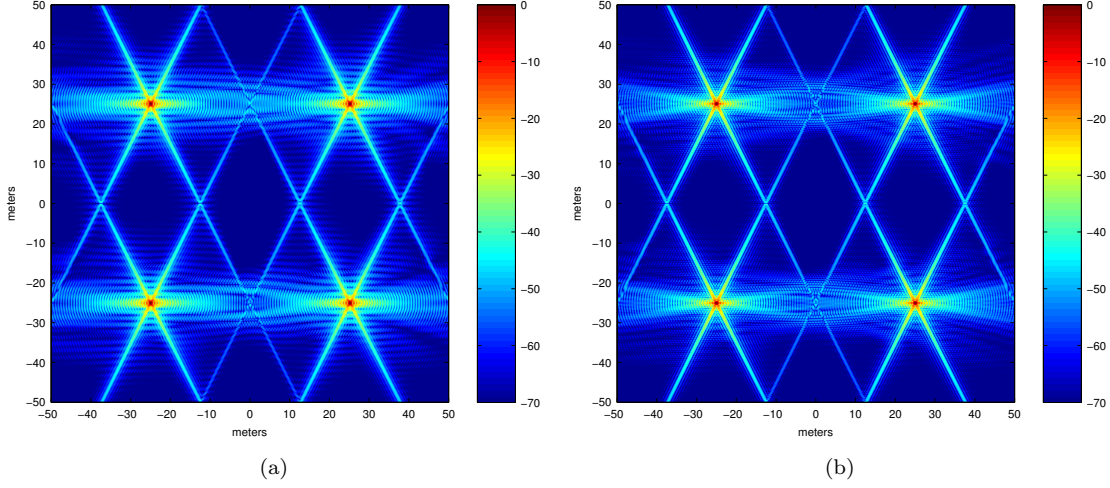


Figure 3.3: Images formed using a simulated phase history which was generated using four targets located at $[25, 25, 0]^T$ m, $[-25, 25, 0]^T$ m, $[25, -25, 0]^T$ m and $[-25, -25, 0]^T$ m (relative to the scene centre). The system parameter are: carrier frequency $\omega_0/2\pi = 308$ MHz, chirp rate $\alpha/\pi = 32.4$ MHz/ μ s, chirp period $T = 10$ μ s, synthetic aperture $[7, -3.5, 7]^T$ km to $[7, 3.5, 7]^T$ km (relative to the scene centre). (a) Image formed using the BP algorithm. (b) Image formed using the filtered BP algorithm.

$$\underset{\mathbf{X}}{\text{minimise}} \|\mathbf{Y} - h(\mathbf{X})\|_F, \quad (3.6)$$

defines the pseudoinverse solution. An approximation of this solution can be achieved very efficiently using a conjugate gradient algorithm. As was seen with the filtered BP algorithms, when the phase history is uniformly sampled, such iterative methods only provide minor image quality improvements. However, for irregularly sampled and nonlinear apertures an iterative approximation of the pseudo inverse may provide significant improvement.

When defining a grid for the image, typically the sample spacing is defined to be slightly smaller than the required sampling rate. This is so that the discrete model more accurately approximates the continuous observational model. Due to this slight oversampling, the discrete observational model $h(\cdot)$ is rank-deficient. Therefore, the pseudo inverse solution is $\hat{\mathbf{X}} \in \mathcal{X}$ that minimises $\|\hat{\mathbf{X}}\|_F$. This solution is not easily computable without using an expensive singular value decomposition (SVD). Instead, the pseudo inverse solution can be approximated using a filtered BP algorithm or alternatively by approximating the solution to the ℓ_F -norm regularised LS optimisation program

$$\underset{\mathbf{X}}{\text{minimise}} \|\mathbf{Y} - h(\mathbf{X})\|_F^2 + \lambda \|\mathbf{X}\|_F^2, \quad (3.7)$$

where, λ is a positive real scalar that controls the effect of the regularisation. As λ approaches 0, the solution of Eq. (3.7) approaches the pseudo inverse solution. This optimisation program can also be approximated using an iterative conjugate gradient algorithm.

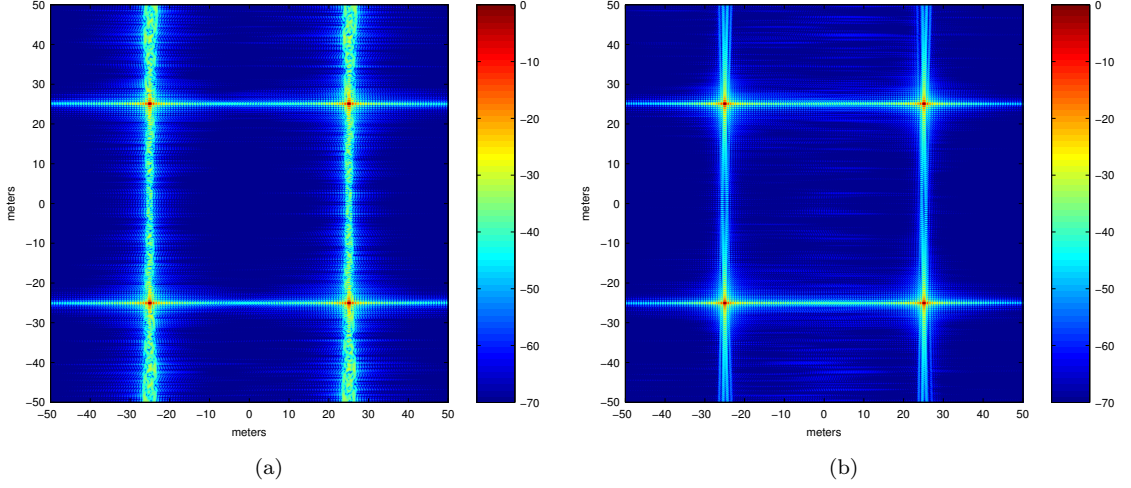


Figure 3.4: Images formed using a simulated phase history which was generated using four targets located at $[25, 25, 0]^T$ m, $[-25, 25, 0]^T$ m, $[25, -25, 0]^T$ m and $[-25, -25, 0]^T$ m (relative to the scene centre). The system parameters are: carrier frequency $\omega_0/2\pi = 10$ GHz, chirp rate $\alpha/\pi = 32.4$ MHz/ μ s, chirp period $T = 10$ μ s, synthetic aperture random locations between $[7, -0.3, 7]^T$ km to $[7, 0.3, 7]^T$ km (relative to the scene centre). (a) Image formed using the filtered BP algorithm (b) Image formed using the LSQR algorithm.

In most scenarios, forming an image by approximately solving Eq. (3.7) will offer little benefits in image quality compared to using a filtered BP algorithm. However, one scenario where it will offer improved image quality is when the synthetic aperture is sampled irregularly. This is because in this scenario, $[hh^H](\mathbf{Y})$ is not well approximated by $\mathbf{Q} \circ \mathbf{Y}$. To demonstrate this scenario, a phase history was simulated, using an irregularly sampled linear aperture, using a scene that contained four targets. The irregular sampling along the aperture was defined such that the slow time measurements were given

$$\hat{t}_n = T_{\hat{t}}N(n - 1 + \mathcal{U}(-0.5, 0.5)), \quad (3.8)$$

for, $n = 1, \dots, N$. Two images were then formed, one using a filtered fast decimation-in-image BP algorithm and the other using an iterative approximation of Eq. (3.7). The iterative approximation was computed using the least squares QR (LSQR) algorithm, which is a conjugate gradient algorithm. The resulting images are shown in Fig. 3.4. The filtered fast BP image has clearly visible cross-range sidelobe artifacts due to the irregular sampling. The ℓ_F -norm regularised LS image, on the other hand, has removed these artifacts and the sidelobes are now consistent with what is expected for the given aperture length. Image formation using an iterative approximation to the ℓ_F -norm regularised LS may also improve the image quality when the synthetic aperture is fully-sampled but highly non-linear.

3.4 Sparsity based Iterative Image Formation

In this section we will present an image formation framework using a mix of ℓ_1 and ℓ_F -norm regularisation, motivated by the theory of CS. The framework will be used to reconstruct *real world* SAR images, which are made up of coherent reflectors from man-made object as well as natural reflectors that exhibit speckle noise.

3.4.1 Image Properties

The theory of CS requires knowledge about the classes of signals to be recovered, which usually comes in the form of a sparse signal model. Therefore before being able to use the tools of CS, the properties of SAR images must be considered.

Statistical Properties

Similar to other coherent imaging systems, SAR images are corrupted by speckle noise. Significant speckle noise occurs in SAR images when the wavelength of the carrier wave is small compared to the resolution of the image. When this occurs, each element of the image can be modelled as the sum of a large number of sub-elements. Each of these objects reflects a fraction of the electromagnetic energy back towards the platform. Therefore, the reflectivity of each element in the image is a summation of the reflectivities of each of the sub-elements. Depending on the characteristics of the sub-elements, these sub-element summations of reflectivities may interfere in different ways:

- *Random interference:* if the scene is rough at the scale of the wavelength, for a particular image element, the summation will contain a large number of *independent* sub-elements. The sum of the reflectivities is then a circularly symmetric complex Gaussian random variable. Additionally, each of the image elements that contain randomly interfering sub-elements, are also independent. This results in the multiplicative circularly symmetric complex Gaussian noise model that is used for SAR images, which is often referred to as *speckle* noise.
- *Constructive interference:* If the scene is smooth for a particular image element, the sub-elements will have similar characteristics which will interfere constructively. This will produce specular reflection. Specular reflection will only reflect significant electromagnetic energy back to the platform if the scene surface is perpendicular to the incident wave. However, due to multiple bounce scattering effects certain objects, e.g. corner reflectors, result in large amounts of energy being reflected back to the platform. Corner reflectors and other objects that reflected large amounts of energy commonly occur in man-made structures and vehicles. Therefore, the corresponding image elements have

larger magnitudes than the image elements that are a result of random interference. Specular reflection is typically dominant in urban areas [49], where, corner reflection accounts for most of the very large magnitude image elements.

3.4.2 Image Model

In a typical SAR image, most image elements can be modelled as the result of random sub-element interference, and only a small number as constructive interference leading to very large magnitude image elements. In order to understand the behaviour of image formation algorithms, it is convenient to split the image into the two parts

$$\mathbf{X} = \mathbf{X}_s + \mathbf{X}_{bg}, \quad (3.9)$$

where, \mathbf{X}_s corresponds to the few very “bright” image elements and \mathbf{X}_{bg} are the lower reflectivity “background” image elements which are contaminated by speckle noise.

If we consider the whole image, most of the pixels contain multiplicative speckle noise and can therefore be modelled as non-stationary circularly symmetric complex Gaussian noise. In terms of information content, this means that the image has a very high entropy and therefore has a very low compressibility. This should mean that the image *cannot* be modelled as sparse in any basis, which prevents us from using CS tools to form an image, containing speckle noise, from an undersampled phase history.

If we consider the image in two parts, however, the part corresponding to the bright image elements \mathbf{X}_s is clearly *sparse* in the image domain and the sparse elements have a magnitude which is typically much larger than the values of the background image elements \mathbf{X}_{bg} . If one considers the image formation of only the bright elements, the rest of the image can be considered as noise. The tools of CS can then be used to recover the bright image elements from an under-sampled phase history. In many applications the image formation of bright image elements, which correspond to man-made structures and vehicles, is critical, especially in military applications.

3.4.3 Image Formation of Bright Image Elements

One of the standard techniques from the CS literature, for the recovery of sparse signals or the approximation of compressible signals from noisy measurements involves solving the convex basis pursuit denoising (BPDN) optimisation program

$$\underset{\mathbf{X}}{\text{minimise}} \|\mathbf{X}\|_1 \text{ subject to } \|\mathbf{Y} - h(\mathbf{X})\|_F \leq \epsilon, \quad (3.10)$$

where, ϵ is selected to be greater than the ℓ_F -norm of the additive noise. An equivalent program to the BPDN is the least absolute shrinkage and selection operator (LASSO) optimisation

program

$$\underset{\mathbf{X}}{\text{minimise}} \|\mathbf{Y} - h(\mathbf{X})\|_F^2 \text{ subject to } \|\mathbf{X}\|_1 \leq \tau \quad (3.11)$$

where, τ is parameter that controls the sparsity of the image. There is a one-to-one map between ϵ and τ for $\epsilon \in \{\|\mathbf{Y} - h(h^\dagger(\mathbf{Y}))\|_F, \|\mathbf{Y}\|_2\}$. The Lagrangian of the LASSO is given by the optimisation program

$$\underset{\mathbf{X}}{\text{minimise}} \|\mathbf{Y} - h(\mathbf{X})\|_F^2 + \lambda \|\mathbf{X}\|_1 \quad (3.12)$$

where, λ is the Lagrangian multiplier. The Lagrangian of LASSO is a ℓ_1 -norm regularised LS. This is a convenient formulation which has two main advantages. Firstly, it is unconstrained and there are fast methods for solving unconstrained problems. Secondly, the parameter selection of λ has only a fixed range of values $\lambda \in [0, 2\|h^H(\mathbf{Y})\|_\infty]$, which also have a one-to-one relation with $\epsilon \in \{\|\mathbf{Y} - h(h^\dagger(\mathbf{Y}))\|_F, \|\mathbf{Y}\|_2\}$. This can make parameter selection easier. In practise ϵ will not be known, however, research into the automatic selection of this parameter is a current area of research [6, 11].

The image formation of the bright image elements \mathbf{X}_s lends itself to the CS based framework because the signal we are trying to reconstruct is approximately sparse. Using the CS framework, \mathbf{X}_s can be formed by solving Eq. (3.12). In our framework we treat the background \mathbf{X}_{bg} as well as the system noise as the total additive noise and therefore, λ is chosen accordingly. Fast iterative algorithms can be used to approximate the solution to Eq. (3.12) using fast RP and BP algorithms. Alternatively, \mathbf{X}_s can also be formed using a greedy algorithm. For example, IHT is a state of the art greedy algorithm which approximately solves

$$\underset{\mathbf{X}}{\text{minimise}} \|\mathbf{Y} - h(\mathbf{X})\|_F^2 \text{ subject to } \|\mathbf{X}\|_0 \leq K. \quad (3.13)$$

Super-resolution Effects

Image formation algorithms that promote sparse solutions have been used with fully-sampled phase histories to produce mild super-resolution. This is because of the sharpening effect on the bright image elements, which produces an extrapolation of the spectral support of an image in the wavenumber spectral domain. This spectral extrapolation also occurs when the phase history is undersampled. This super-resolution effect may not always be desirable. In this situation, the extrapolated spectrum can be removed by computing $\mathbf{X}_s \leftarrow h^\dagger(h(\mathbf{X}_s))$.

To demonstrate this effect, a phase history was simulated from a scene with four targets. An image was then formed using an iterative approximation to Eq. (3.12). Another image was generated by removing the extrapolated spectrum from the first image, where, $h^\dagger(\cdot)$ was approximated using a filtered fast decimation-in-image BP algorithm. The two images are

shown in Fig. 3.5. The targets in the first image are represented by four non-zero pixels, while for the second image the targets have PSF which are what are expected for an image formed using a standard image formation algorithm with given chirp bandwidth and synthetic aperture length.

3.4.4 Image Formation of Background Image Elements

There is no possible sparse signal model for the background image elements because they contain speckle noise. Therefore, CS techniques are not directly applicable. Instead we propose forming the background image elements using an approximation of the pseudo inverse. This can be achieved by applying the filtered BP algorithm to the phase history with the bright image elements removed, i.e. $h^H(\mathbf{Q} \circ \mathbf{Y}_r)$, where, $\mathbf{Y}_r = \mathbf{Y} - h(\hat{\mathbf{X}}_s)$, or by using an iterative algorithm to solve the ℓ_F -norm regularised LS optimisation program

$$\underset{\mathbf{X}}{\text{minimise}} \|\mathbf{Y}_r - h(\mathbf{X})\|_F^2 + \lambda_{bg} \|\mathbf{X}\|_F^2, \quad (3.14)$$

where, λ_{bg} is a small value so that the solution is approximately the pseudo inverse solution. Both solutions will not address the undersampling and the image quality of the background elements will have large target sidelobes. The total image $\hat{\mathbf{X}}$ can then be formed by summing the two image components, i.e.

$$\hat{\mathbf{X}} = \hat{\mathbf{X}}_{bg} + \hat{\mathbf{X}}_s. \quad (3.15)$$

The total formed image will still have poor contrast in the image elements that are affected by speckle due to the undersampling. However, the overall image quality is likely to be improved in all elements compared with images formed using standard methods. This is because using a CS inspired approach improves the image formation of bright image elements, this not only improves the image quality for these elements but also reduces their effect on the background image elements. Using standard methods, a significant amount of energy from the bright image elements is contained in their sidelobes and because bright image elements tend to have much larger magnitudes than the background, this energy dominates the background of the image.

3.5 Experiments

To demonstrate the computational advantages of the fast BP algorithms in an iterative algorithm, the computational times for image formation were measured for different size phase histories and images. Images were formed using five iterations of the fast iterative shrinkage-thresholding algorithm (FISTA) and five iterations of the LSQR algorithm. For each algorithm an image was formed using four different algorithms for $h(\cdot)$ and $h^H(\cdot)$, the RP and

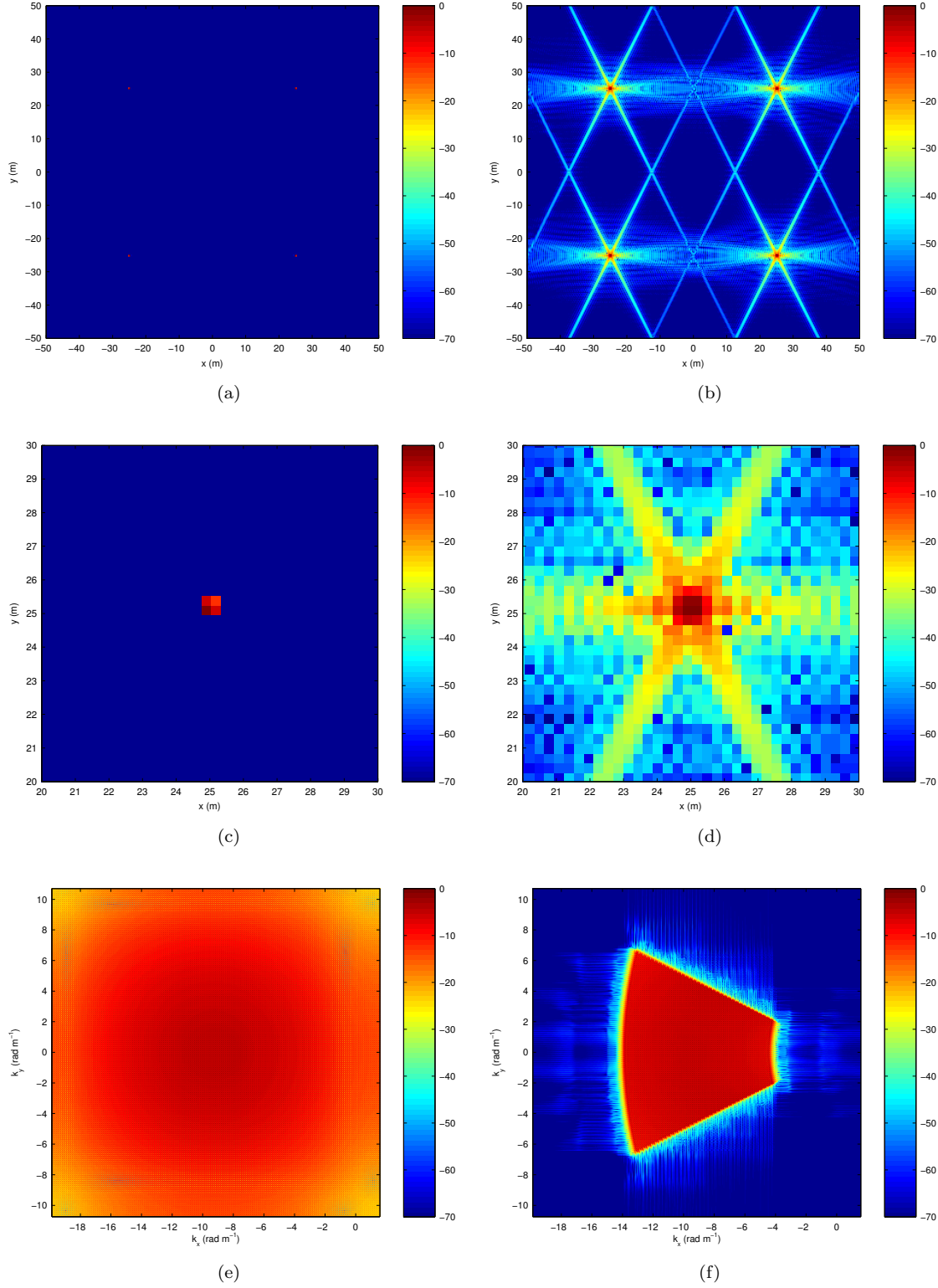


Figure 3.5: Images formed using a simulated phase history which was generated using four targets located at $[25, 25, 0]^T$ m, $[-25, 25, 0]^T$ m, $[25, -25, 0]^T$ m and $[-25, -25, 0]^T$ m (relative to the scene centre). The system parameters are: carrier frequency $\omega_0/2\pi = 308$ MHz, chirp rate $\alpha/\pi = 32.4$ MHz/ μ s, chirp period $T = 10$ μ s, synthetic aperture $[7, -3.5, 7]^T$ km to $[7, 3.5, 7]^T$ km (relative to the scene centre). Images were formed using the FISTA based sparse image formation. (a) Image with full spectral support. (b) Image with projected spectral support. (c) Zoomed image of (a). (d) Zoomed image of (b). (e) Wavenumber spectrum of image in (a). (f) Wavenumber spectrum of image in (b).

Table 3.1: LSQR image formation times (seconds)

N	RP/BP	fast RP/BP (Dec. Image)	fast RP/BP (Dec. PH)	PFA
256	186.10	49.28	48.88	9.26
512	1480.23	198.74	198.74	37.13
1024	12515.03	813.81	812.61	172.03
2048	100037.91	3286.19	3287.67	767.19

Table 3.2: FISTA image formation times (seconds)

N	RP/BP	fast RP/BP (Dec. Image)	fast RP/BP (Dec. PH)	PFA
256	236.03	62.13	61.96	11.77
512	1876.52	254.12	254.30	47.20
1024	16000.53	1031.99	1025.18	224.85
2048	127334.56	4168.90	4170.27	981.27

BP algorithm, the PFA and the fast decimation-in-phase-history and decimation-in-image BP algorithms. Both the RP and BP algorithm and the PFA made used the NUFFT algorithm with a interpolation kernel length of 24 samples. The image formation times were measured on a single core of a 2.5 GHz Intel Xeon processor with N^2 element images and N^2 element phase histories. The number of decomposition stages in the fast RP and BP algorithms was $\log_2 N - \log_2 64$. Table 3.1 and Table 3.2 show the resulting image formation times in seconds.

The computational cost of the LSQR algorithm is approximately 10-11 times that of the equivalent image formation computational cost in Chap. 2 in Table 2.1. While, the computational cost of the FISTA algorithm is approximately 13-14 times slower. This is consistent with the assumption that the main computational cost of iterative image formation algorithms comes from the computation of $h(\cdot)$ and $h^H(\cdot)$ at each iteration. The FISTA has a slightly greater computational cost because it must additionally perform an elements-wise *soft-shrinkage* at each iteration.

The number of iteration required to achieve an acceptable solution for the LSQR algorithms like other conjugate gradient algorithms depends on the condition number κ of $h^H(h(\cdot) + \lambda)$. Explicitly, the distance between the value at the i th iteration and the true solution is $\mathcal{O}\left(\left(\frac{\sqrt{\kappa}-1}{\sqrt{\kappa}+1}\right)^i\right)$ [67]. For the FISTA algorithm this same distance at the i th iteration is $\mathcal{O}(i^{-2})$ [12]. In practice, we found that in most problems, an acceptable solution is achievable in a small number of iterations, around ten.

To demonstrate the sparsity based iterative image formation framework for undersampled data, images were reconstructed from the Gotcha data set, with subsets of the phase history set to zero to simulate missing data. In the first experiment a 25% and 50% random subset of phase history in the fast-time direction was zeroed. In the other experiment a 25% and 50% random subset of phase history in the slow-time direction was zeroed. Images were reconstructed using the BP algorithm and a FISTA-based and a IHT-based sparsity based iterative image formation

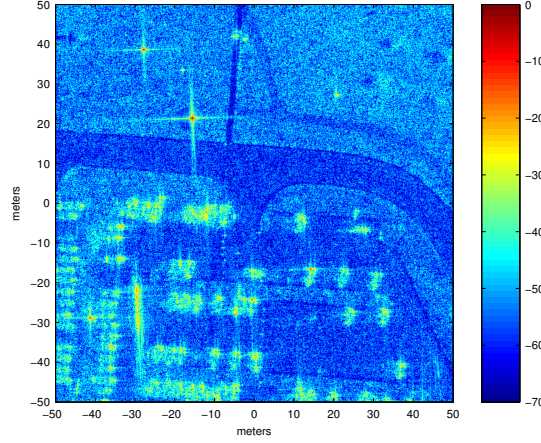


Figure 3.6: Image formed using the HH polarisation with the angles $1 - 4^\circ$ of the eighth pass of the Gotcha data set. The images contain 768×768 pixels. The antenna beamwidths were limited to a 1.15° azimuth angle and a 0.57° polar angle. Image was formed using the filtered BP algorithm

algorithm. For the FISTA-based algorithm, the bright elements were reconstructed using the FISTA algorithm with $\lambda = 0.005 \cdot 2 \|h^H(\mathbf{Y})\|_\infty$. While for the IHT-based algorithm, the IHT algorithm was used with $K = 15000$. In both sparsity based algorithms, after recovering the bright image elements, the super-resolution effects were removed, using the method described in Section 3.4.3. The background elements were then recovered using a fast filtered decimation-in-image BP algorithm. The resulting images are shown in Fig. 3.7 and Fig. 3.8. For reference, an image formed using the BP algorithm from the full phase history is shown in Fig. 3.6.

The resulting images using the sparsity based framework are visually improved. The recovered bright image elements look almost visually identical to the same elements in the reference image even with only half the phase history. For the background image elements, there is less contrast compared to the reference image which degrades as the undersampling increases. However, the image quality is still improved when compared with the fast BP image because the energy from the bright image elements has been well recovered. The differences between the visual image quality of the FISTA-based and IHT-based images are small.

3.6 Summary

In this chapter we have proposed an iterative image formation framework for SAR which is based on fast RP and BP algorithms. Unlike existing iterative image formation algorithms, the proposed framework can incorporate near-field scenes, non-linear apertures and non-flat scene terrain. The framework can improve the quality of images formed from fully-sampled and undersampled phase histories in some scenarios. When the phase history is undersampled the framework can make use CS sparsity based techniques. These techniques were tailored to the properties of real SAR images, namely speckle noise. Sparsity based image formation was show

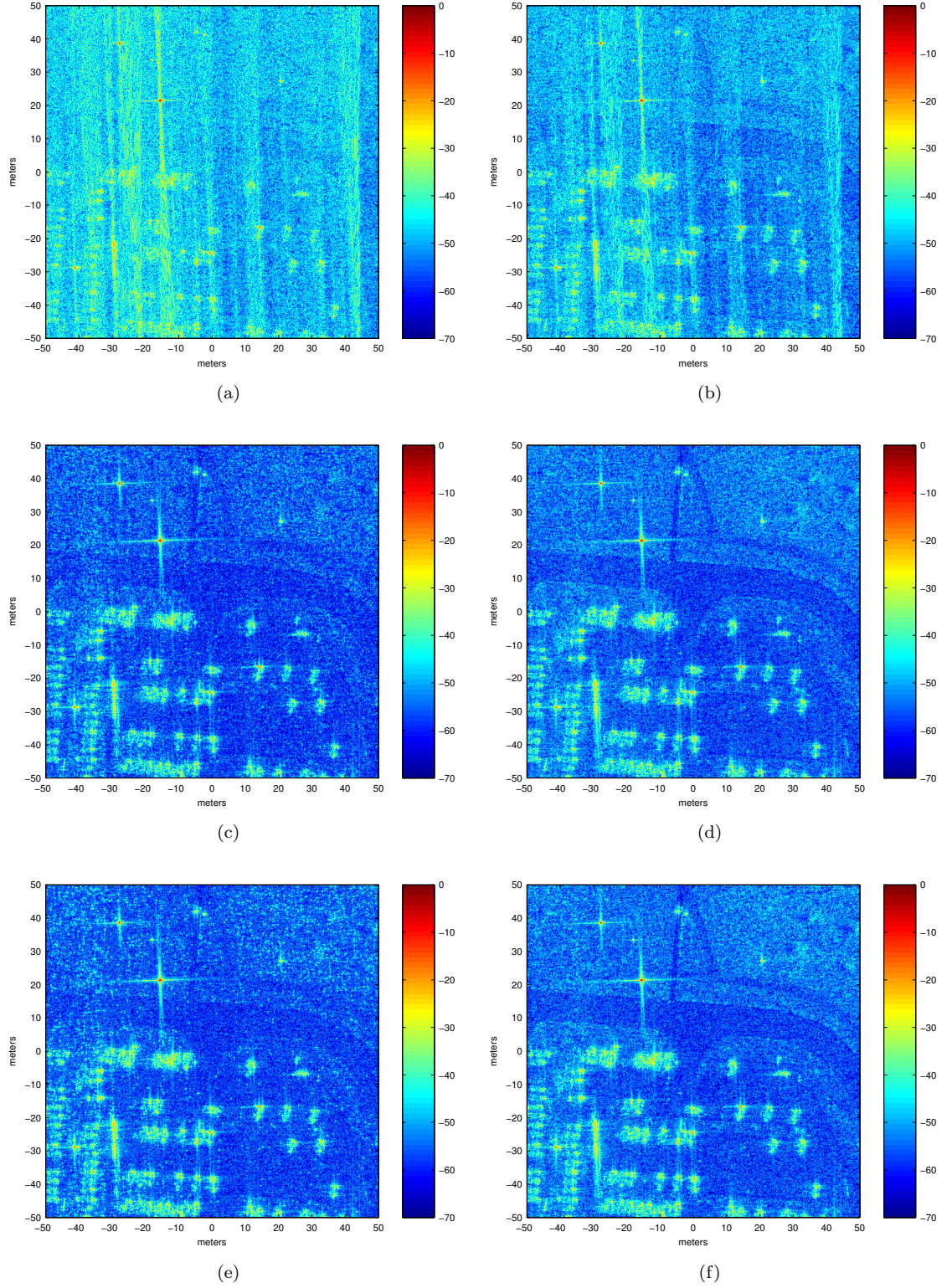


Figure 3.7: Images formed using the HH polarisation with the angles $1 - 4^\circ$ of the eighth pass of the Gotcha data set with cross-range undersampling. The images contain 768×768 pixels. The antenna beamwidths were limited to a 1.15° azimuth angle and a 0.57° polar angle. (b), (d) and (f) were formed using a random 75% subset of the phase history cross-range samples. (a), (c) and (e) were formed using a random 50% subset of the phase history cross-range samples. (b) and (a) were formed using the filtered BP algorithm. (d) and (c) were formed using the FISTA based sparse image formation. (f) and (e) were formed using the IHT based sparse image formation

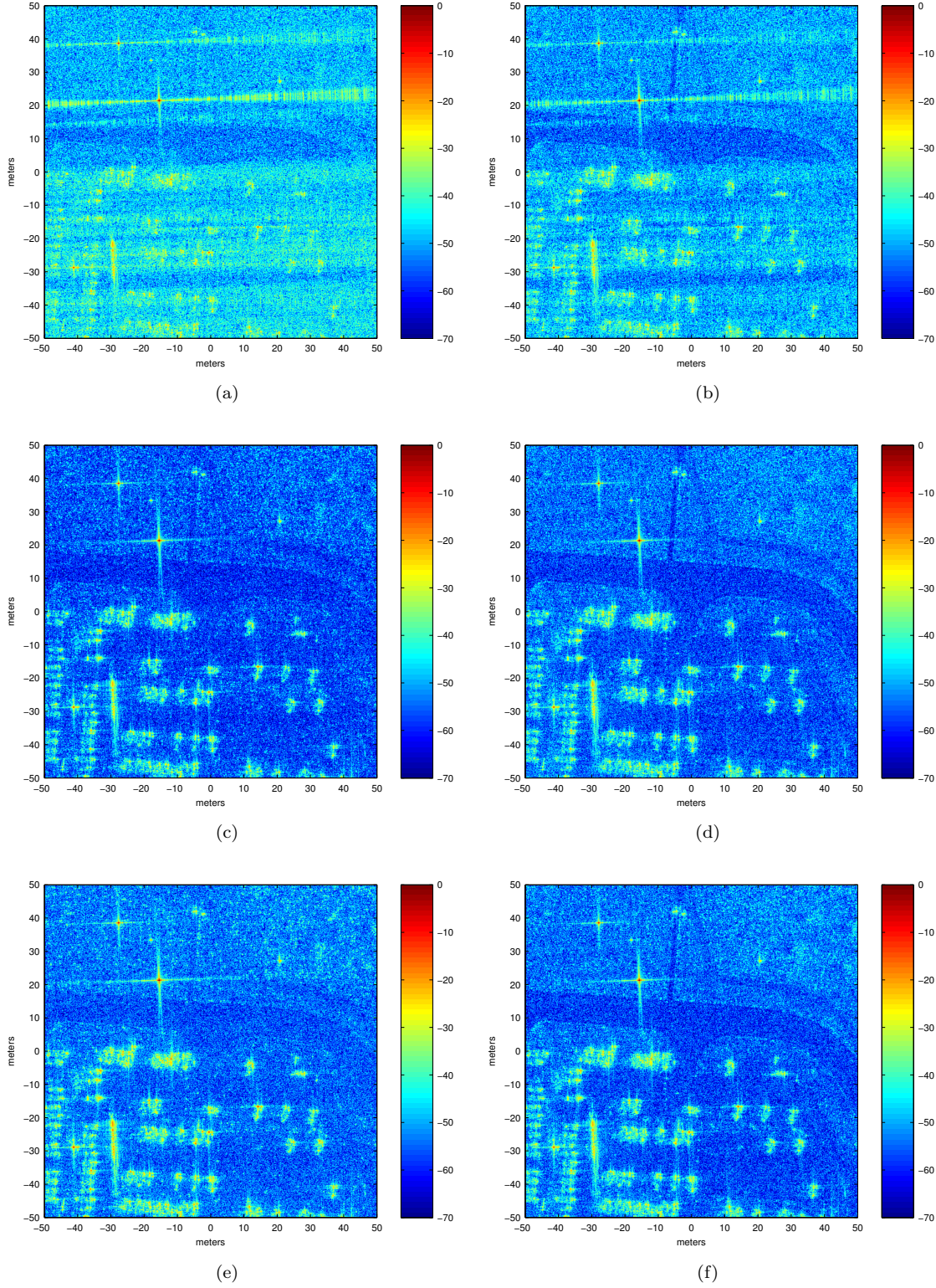


Figure 3.8: Images formed using the HH polarisation with the angles $1 - 4^\circ$ of the eighth pass of the Gotcha data set with range undersampling. The images contain 768×768 pixels. The antenna beamwidths were limited to a 1.15° azimuth angle and a 0.57° polar angle. (b), (d) and (f) were formed using a random 75% subset of the phase history range samples. (a), (c) and (e) were formed using a random 50% subset of the phase history range samples. (b) and (a) were formed using the filtered BP algorithm. (d) and (c) were formed using the FISTA based sparse image formation. (f) and (e) were formed using the IHT based sparse image formation

to improve the visual quality of images formed from a real undersampled phase history.

Chapter 4

Auto-focus

4.1 Introduction

SAR image formation algorithms are usually based on exact knowledge of the linear observation system, however, in practical situations, such a system cannot be perfectly known. Errors in the model of the linear observation system can produce significant errors in the phase history.

Significant errors arise in the model of a SAR system because the round trip propagation delay to a reference position in the scene must be estimated at each position along the aperture. In spotlight mode SAR, this reference point corresponds to the scene centre. Errors that occur in these estimates are primarily due to non-idealised propagation mediums and/or platform position errors due to inaccuracies in the navigation system. If not corrected, phase errors can degrade and produce distortions in the formed image.

Methods for correcting these errors in fully-sampled systems are known as autofocus algorithms and are most commonly used as a post-processing method on the formed image. All autofocus algorithms require a signal model for either the phase errors and the image or both. Additionally, many algorithms make a far-field and small aperture angle approximation so that the phase errors are constant along the range axis of the formed image. One of the earliest autofocus algorithms to be developed was the mapdrift (MD) algorithm [29]. MD estimates the phase errors based on a low-order polynomial model for the phase errors along the cross-range direction. Phase gradient autofocus (PGA), one of the most commonly used algorithms, requires the phase errors along the cross-range direction to vary smoothly and also requires the image to contain isolated point scatterers [132, 75]. Recently another algorithm, multichannel autofocus (MCA), has been proposed which requires the focused image to contain a known region which is almost zero [94, 84]. All of these listed algorithms are post-processors and although these methods have been very successful for correcting phase errors in fully-sampled scenarios, they may not be suitable for undersampled SAR.

In undersampling scenarios, the inverse is ill-posed. As was mentioned in Chap. 3, to make

this problem well-posed, an appealing idea is to apply the tools and theory of CS and SR. However, the tools and theoretical results from CS also require exact knowledge of the linear observation system. Therefore, the tools of CS cannot be directly used.

The algorithm proposed in this chapter for image formation and autofocus of an undersampled phase history has similarities with the proposed method in [106]. Although the method proposed in [106] primarily concentrates on the fully-sampled scenario it does demonstrate that it is also applicable to the undersampled scenario. Both methods involve approximately solving the same non-convex problem, however, the algorithm proposed in this chapter has some additional practical benefits. Firstly, it can be shown to be stable and it produces a sequence that converges to a connected set [137, Proposition B.3]. Secondly, it empirically converges in a significantly smaller number of iterations.

A closely related problem which has been investigated in the signal processing literature in the last few years is the problem of phase retrieval [26, 45, 85]. The goal of phase retrieval is to recover a complex signal from magnitude only measurements. The SAR imaging and autofocus problem is equivalent to the phase retrieval problem if we ignore all phase information due to a belief that it is corrupted. In these papers, a technique known as “phase-lifting” is used to pose a convex problem which is solved to recover the signal. This technique involves “lifting” the signal so instead of recovering $\mathbf{x} \in \mathbb{C}^N$ the algorithm recovers $\mathbf{X} = \mathbf{x}\mathbf{x}^H \in \mathbb{C}^{N \times N}$. This process is likely to be very costly computationally and will likely make these techniques infeasible for SAR systems.

The outline of this chapter is as follows. In Section 4.3 the expected performance of existing post-processing autofocus methods in a SR framework is investigated. Inherent ambiguities in the undersampled phase error problem are analysed in Section 4.4. An image formation algorithm for undersampled SAR with phase errors is proposed in Section 4.5. Finally experimental simulations in Section 4.6 are used to demonstrate the effectiveness of the proposed algorithm.

4.2 Observation model with Phase Errors

Consider the observation model for a SAR system after dechirping and deskewing developed in Chapter 2 with one small modification. This modification involves swapping the dimensions of the phase history $\mathbf{Y} \in \mathbb{C}^{M \times N}$ such that the row dimension is now fast-time and the column dimension is slow-time. This is done for notational convenience sake so the multiplication of the phase history with the phase errors is a right-hand side (RHS) multiplication. This non-standard convention is used only within this chapter. With this model, adding a delay error τ_e in the dechirping and deskewing operations at each aperture position produces the following discretised observation model [76].

$$\mathbf{Y} = \exp(j\Phi) \circ h(\mathbf{X}), \quad (4.1)$$

where,

$$\Phi \in \mathbb{C}^{M \times N} = \{\phi_{mn}\} = \left\{ \left(\omega_0 \tau_{em} - \alpha \tau_{em}^2 \right) + 2\alpha \tau_{em} \left(\frac{n-1}{f_t} - \frac{T_t}{2} \right) \right\} \quad (4.2)$$

are the phase errors which result from the delay errors. If we neglect the effects of the linear phase term, which is done in most systems because it usually has only a minor effect on the image quality, the discrete SAR observation model with phase errors becomes

$$\mathbf{Y} = \text{diag}(\exp(j\phi))h(\mathbf{X}), \quad (4.3)$$

where,

$$\phi_m = \omega_0 \tau_{em} - \alpha \tau_{em}^2 \quad (4.4)$$

are the phase errors.

Clearly, without further assumptions, the problem of recovering ϕ and \mathbf{X} from \mathbf{Y} is ill-posed if $M = M'$ and $N = N'$, since there are only $M'N'$ equations and $M'(N' + 1)$ unknowns.

4.3 Sparse Image Formation with Post-processing Autofocus

Most post-processing autofocus methods make a far-field and small aperture angle approximation in the SAR observation model [76], i.e. the image was formed using a separable two-dimensional image formation algorithm such as RDA [120]. Under the separable approximation and assuming we sample at exactly the Nyquist rate in range and cross range, the system can be modelled as the following left-hand side (LHS) and RHS matrix multiplication:

$$\mathbf{Y} = \text{diag}\{\exp(j\phi)\}\mathbf{A}\mathbf{X}\mathbf{B}, \quad (4.5)$$

where,

$$a_{mn} = \exp\left(-j\left(2\pi\frac{(m-1)(n-1)}{M} - (m-1)\pi - (n-1)\pi + \frac{M\pi}{2}\right)\right)$$

and

$$b_{mn} = \exp\left(-j\left(2\pi\frac{(m-1)(n-1)}{N} - (m-1)(\pi\omega_0\alpha T - \pi) - (n-1)\left(\pi + \frac{N\pi}{2} - 2\omega_0 L/c_0\right)\right)\right)$$

are the elements of the cross-range matrix $\mathbf{A} \in \mathbb{C}^{M \times M}$ and the range matrix $\mathbf{B} \in \mathbb{C}^{N \times N}$, respectively, where, L is the scene radius. This can be derived by assuming that the spatial

Fourier support is rectangular and offset from the origin by $\omega_0/\pi c_0$ in the range spatial Fourier dimension.

Under the assumption that \mathbf{A} is essentially a Fourier matrix, we can rewrite the observation model in Eq. (4.5) as $\mathbf{Y} = \mathbf{A}\Psi\mathbf{X}\mathbf{B}$, where, Ψ is a *circulant* matrix which may be viewed as a filter in cross-range direction for each range bin.

When fully-sampled, recovering $\Psi\mathbf{X}$ from \mathbf{Y} is straight forward because \mathbf{A} and \mathbf{B} are invertible. Post-processing autofocus algorithms can then recover \mathbf{X} from the filtered image $\Psi\mathbf{X}$, by using a signal model for Ψ and/or \mathbf{X} .

When \mathbf{Y} is undersampled in either range or cross-range the observation model will be:

$$\mathbf{Y}' = \mathbf{A}\Psi\mathbf{X}\mathbf{B}' \quad (4.6)$$

or

$$\mathbf{Y}' = \mathbf{A}'\Psi\mathbf{X}\mathbf{B}, \quad (4.7)$$

where, $\mathbf{A}' \in \mathbb{C}^{M \times M'}$ is a $M < M'$ row subset of \mathbf{A} and $\mathbf{B}' \in \mathbb{C}^{N' \times N}$ is a $N < N'$ column subset of \mathbf{B} . With this model, unlike in the fully-sampled situation, \mathbf{A}' and \mathbf{B}' are not invertible.

An estimate of $\Psi\mathbf{X}$ can be reconstructed by solving an ℓ_1 -norm regularised LS optimisation program. CS results can then be used to analyse the expected reconstruction quality of this estimate. If the undersampling is random in cross-range, the reconstruction of the filtered image is stable, in the sense that the columns of the recovered filtered image $\tilde{\Psi}\tilde{\mathbf{X}}$ satisfy Eq. (1.1.9), if the number of cross-range samples is greater than $\mathcal{O}(K \log^5(M'))$. For a fixed K , the reconstruction error is dependent on the additive noise and the K -term approximations of the columns of the filtered image. Larger phase errors will make these K -term approximations worse and therefore increase the error in the reconstructed filtered image.

With an estimate of the filtered image, the image can be recovered by applying a standard post-processing autofocus technique. The resulting image is given by

$$\tilde{\mathbf{X}} = \tilde{\Psi}^{-1}\tilde{\Psi}\tilde{\mathbf{X}}, \quad (4.8)$$

where, $\tilde{\Psi}^{-1} = \mathbf{A}^{-1} \text{diag} \left\{ \exp(-j\tilde{\phi}) \right\} \mathbf{A}$ is the phase error correction applied by the autofocus algorithm and $\tilde{\phi}$ are the estimated phase errors by the chosen algorithm. If the estimated phase errors are the true phase errors then the error in the reconstructed image is given by

$$\mathbf{X} - \tilde{\mathbf{X}} = \Psi^{-1}\mathbf{E} \quad (4.9)$$

where, $\mathbf{E} = \Psi\mathbf{X} - \tilde{\Psi}\tilde{\mathbf{X}}$ is the error in the estimated filtered image. Therefore, even with knowledge of the true phase errors, the effect of correcting phase errors as a post-processing step can result in a significant error in the reconstructed image. For this reason, in most cases,

post-processing autofocus methods are unsuitable for undersampled SAR.

4.4 Uniqueness of Image Formation and Autofocus

It is well-known that there are inherent ambiguities in the autofocus problem which prevent the problem having a unique solution. The formulation in Eq. (4.5) is known to be ambiguous to constant and linear phase errors along the cross-range dimension [76].

A sparsity based necessary condition for the uniqueness of the autofocus problem can be given which is dependent on the observation model $h(\cdot)$ and the signal model of the image \mathbf{X} . It is given as follows.

$$h(\tilde{\mathbf{X}}) = \text{diag}\{\mathbf{d}\}h(\mathbf{X}) \iff \exists \beta \in \{\beta \in \mathbb{C} : |\beta| = 1\} : \tilde{\mathbf{X}} = \beta\mathbf{X}, \quad (4.10)$$

$$\forall (\tilde{\mathbf{X}}, \mathbf{X}, \mathbf{d}) \in \left\{ \tilde{\mathbf{X}} \in \mathcal{X}, \mathbf{X} \in \mathcal{X}, \mathbf{d} \in \mathcal{D} \right\},$$

where,

$$\mathcal{X} = \left\{ \mathbf{X} \in \mathbb{C}^{M' \times N'} : \|\mathbf{X}\|_0 \leq K \right\},$$

i.e. we know the scene has at most K scatters, and

$$\mathcal{D} = \left\{ \mathbf{d} \in \mathbb{C}^M : |d_m| = 1 \right\}$$

is the set of all possible phase errors,

If Eq. (4.10) is satisfied then the problem is unique up to a scalar β multiplication of the true \mathbf{X} , i.e. $\tilde{\mathbf{X}} = \beta\mathbf{X}$, and the solutions are given by the following program.

$$\begin{aligned} & \underset{\mathbf{X}, \mathbf{d}}{\text{minimise}} \quad \|\mathbf{X}\|_0 \\ & \text{subject to} \quad \text{diag}\{\mathbf{d}\}\mathbf{Y} = h(\mathbf{X}) \\ & \quad \quad \quad d_m^* d_m = 1, \quad m = 1, \dots, M, \end{aligned} \quad (4.11)$$

Eq. (4.10) states that the phase error free observation model $h(\cdot)$ must have the property that the phase history of a sparse image cannot be equal to a phase error corrupted phase history of a different sparse image.

Using ideas from the dictionary learning literature we can define a set of sufficient conditions for the uniqueness of ϕ and \mathbf{X} given $\mathbf{Y}' = \text{diag}\{\mathbf{d}'\}\mathbf{A}'\mathbf{X}\mathbf{B}$ [2]. These conditions are as follows:

1. the spark condition: any $2K_{\mathbf{X}}$ columns of \mathbf{A}' are linearly independent

2. the columns of \mathbf{X} have exactly $K_{\mathbf{X}}$ non-zero elements
3. for each of the $\binom{M}{K_{\mathbf{X}}}$ possible $K_{\mathbf{X}}$ -sparse supports, there are at least $K_{\mathbf{X}} + 1$ columns of \mathbf{X}
4. any $K_{\mathbf{X}} + 1$ columns of \mathbf{X} which share the same support, span a $K_{\mathbf{X}}$ -dimensional space
5. any $K_{\mathbf{X}} + 1$ columns of \mathbf{X} , which have different supports, span a $(K_{\mathbf{X}} + 1)$ -dimensional space

Proposition 4.4.1 (see [2, Theorem 3]). *If the above conditions hold then there is a unique $\tilde{\mathbf{X}}$ which satisfies $\mathbf{Y}' = \text{diag}\{\tilde{\mathbf{d}}'\}\mathbf{A}'\tilde{\mathbf{X}}\mathbf{B}$. Where uniqueness is up to a unit magnitude scalar β and a circular permutation \mathbf{P}^m of the true \mathbf{X} , i.e. $\tilde{\mathbf{X}} = \beta\mathbf{P}^m\mathbf{X}$*

where, $m \in \mathbb{Z}$ and

$$\mathbf{P} = \begin{bmatrix} 0 & 0 & \dots & 0 & 1 \\ 1 & 0 & \dots & 0 & 0 \\ 0 & \ddots & \ddots & \vdots & \vdots \\ \vdots & \ddots & \ddots & 0 & 0 \\ 0 & \dots & 0 & 1 & 0 \end{bmatrix}.$$

As is the case in dictionary learning, the richness condition 3 is completely unrealistic for undersampled SAR. However, this condition is only sufficient and is likely to be very pessimistic. It should also be noted that recovering the unique solution involves solving Eq. (4.11) which requires combinatorial many operations to solve and is unsuitable for practical problems that involve noise.

4.5 Sparse Image Formation and Autofocus

In this section our goal is to design an algorithm which performs sparse image formation and autofocus and can be approximately solved in a polynomial time. To this end, motivated by convex relaxation techniques, the non-convex function $\|\mathbf{X}\|_0$ in Eq. (4.11) is replaced with its closest convex function $\|\mathbf{X}\|_1$ and the equality constraint is replaced with an inequality constraint that accommodates noise. This results in

$$\begin{aligned} & \underset{\mathbf{X}, \mathbf{d}}{\text{minimise}} \quad \|\mathbf{X}\|_1 \\ & \text{subject to} \quad \|\text{diag}\{\mathbf{d}\}\mathbf{Y} - h(\mathbf{X})\|_{\text{F}} \leq \epsilon \\ & \quad d_m^* d_m = 1, \quad m = 1, \dots, M. \end{aligned} \tag{4.12}$$

Even though our objective function is now convex, Eq. (4.12) is still non-convex because the inequality constraint is not linear and does not define a convex feasible set.

In order to use gradient based methods, which are usually used in large scale problems such as SAR image formation, the objective must be smooth. Therefore, it is convenient to exchange the inequality constraint and the objective in Eq. (4.12) to form the equivalent program

$$\begin{aligned} & \underset{\mathbf{X}, \mathbf{d}}{\text{minimise}} \quad \|\text{diag}\{\mathbf{d}\}\mathbf{Y} - h(\mathbf{X})\|_{\text{F}}^2 \\ & \text{subject to} \quad \|\mathbf{X}\|_1 \leq \tau \\ & \quad \quad \quad d_m^* d_m = 1, \quad m = 1, \dots, M. \end{aligned} \tag{4.13}$$

Even though this problem is still non-convex, importantly, in each set of variables \mathbf{X} and \mathbf{d} –with the other fixed– there is a unique solution. This observation allows us to use a block relaxation type method which can be used to approximate the solution and has been found to be effective in the related problem of dictionary learning [137].

4.5.1 Block Relaxation

Block relaxation is optimisation strategy which splits the optimisation parameters into blocks. The optimisation program is then solved by cycling through the blocks, solving based on a single parameter block at a time. Block relaxation can be used to approximately solve Eq. (4.13) by iteratively solving the problem based on a single parameter block, \mathbf{X} or \mathbf{d} , at a time. Therefore, we must consider the solution of Eq. (4.13) for each parameter block.

Minimisation based on \mathbf{X}

Consider Eq (4.13) when \mathbf{d} is fixed, i.e.

$$\begin{aligned} & \underset{\mathbf{X}}{\text{minimise}} \quad f(\mathbf{X}, \mathbf{d}) \\ & \text{subject to} \quad \|\mathbf{X}\|_1 \leq \tau, \end{aligned} \tag{4.14}$$

where,

$$f(\mathbf{X}, \mathbf{d}) = \|\text{diag}\{\mathbf{d}\}\mathbf{Y} - h(\mathbf{X})\|_{\text{F}}^2. \tag{4.15}$$

A method used for solving Eq. (4.14) is a technique known as “majorisation minimisation”. This technique replaces the objective function with a majorising surrogate function which is much easier to solve. A function g is said to majorise f if $f(\omega) \leq g(\omega, \xi)$ and $f(\omega) = g(\omega, \omega)$, $\forall \omega$ and $\xi \in \Upsilon$, where, Υ is the parameter space. A surrogate function can be derived for (4.15) by expanding it as a Taylor series and bounding its curvature ($d^2 f$) [137]. This surrogate function

is:

$$g(\mathbf{X}, \mathbf{X}^\dagger, \mathbf{d}) = \|\text{diag}\{\mathbf{d}\}\mathbf{Y} - h(\mathbf{X})\|_{\text{F}}^2 - \left\|h(\mathbf{X}) - h(\mathbf{X}^\dagger)\right\|_{\text{F}}^2 + L_X \left\|\mathbf{X} - \mathbf{X}^\dagger\right\|_{\text{F}}^2, \quad (4.16)$$

where, $L_X > \|h(\cdot)\|^2$. Replacing the objective function with its surrogate function, Eq. (4.14) becomes

$$\begin{aligned} & \underset{\mathbf{X}, \mathbf{X}^\dagger}{\text{minimise}} \ g(\mathbf{X}, \mathbf{X}^\dagger, \mathbf{d}) \\ & \text{subject to } \|\mathbf{X}\|_1 \leq \tau, \end{aligned} \quad (4.17)$$

which is a minimisation based on \mathbf{X} and a surrogate parameter vector \mathbf{X}^\dagger . In this program, if \mathbf{X} is fixed, the minimum of Eq. (4.17) occurs at $\mathbf{X}^\dagger = \mathbf{X}$ and if \mathbf{X}^\dagger is fixed the minimum occurs at

$$\begin{aligned} & \underset{\mathbf{X}}{\text{minimise}} \ \|\mathbf{X} - \mathbf{C}\|_{\text{F}} \\ & \text{subject to; } \|\mathbf{X}\|_1 \leq \tau, \end{aligned} \quad (4.18)$$

where, $\mathbf{C} = \mathbf{X}^\dagger + L_X^{-1} h^{\text{H}}(\text{diag}(\mathbf{d})\mathbf{Y} - h^{\text{H}}(\mathbf{X}^\dagger))$. The solution of Eq. (4.18) is the projection of \mathbf{C} onto an ℓ_1 ball with a radius of τ . There are efficient methods to exactly compute this projection [53].

By minimising Eq. (4.17) based on either \mathbf{X}^\dagger and \mathbf{X} in an alternating fashion, \mathbf{X}^\dagger and \mathbf{X} will converge to the solution of Eq. (4.14) [15]. To solve this problem we need to select a valid L_X , however in practice, a feasible L_X can be determined using a backtracking line search [12].

Minimisation based on \mathbf{d}

Consider Eq. (4.13) when \mathbf{X} is fixed, which (ignoring constant terms) is given by:

$$\begin{aligned} & \underset{\mathbf{d}}{\text{minimise}} \ \text{tr} \left(-2 \text{Re} \left\{ \text{diag} \left\{ \mathbf{d}^{\text{H}} \right\} h(\mathbf{X}) \mathbf{Y}^{\text{H}} \right\} \right) \\ & \text{subject to } d_m^* d_m = 1, \ m = 1, \dots, M. \end{aligned} \quad (4.19)$$

The unique solution of Eq. (4.19) can be found analytically by,

$$\mathbf{d} = \exp \left(j \angle \text{diag} \left\{ h(\mathbf{X}) \mathbf{Y}^{\text{H}} \right\} \right). \quad (4.20)$$

A block relaxation of Eq. (4.13) is produced by solving Eq. (4.14) and Eq. (4.19) in an alternating fashion which is described in Algorithm 3. Where, \mathcal{D} solves Eq. (4.14). The approaches used in [106], [105] and [81] are of this form. These types of methods are stable, assuming we can solve \mathcal{D} , i.e. we exactly solve Eq. (4.14) at each iteration. In practical algorithms where only an approximate solution at each iteration is obtained, no stability analysis exists.

Algorithm 3 $\mathcal{A}(\mathbf{X}, \mathbf{d})$

Output: \mathbf{X}, \mathbf{d}

```

repeat
   $\mathbf{X}^\dagger \leftarrow \mathbf{X}$ 
   $\mathbf{X} \leftarrow \mathcal{D}(\mathbf{X}, \mathbf{d})$ 
   $\mathbf{d}^\dagger \leftarrow \mathbf{d}$ 
   $\mathbf{d} \leftarrow \exp\left(j\angle \text{diag}\left\{h(\mathbf{X})\mathbf{Y}^H\right\}\right)$ 
until  $\left\|\mathbf{X} - \mathbf{X}^\dagger\right\|_F \left\|\mathbf{X}^\dagger\right\|_F^{-1} < \text{threshold} \wedge \left\|\mathbf{d} - \mathbf{d}^\dagger\right\|_2 \left\|\mathbf{d}^\dagger\right\|_2^{-1} < \text{threshold}$ 

```

Another way to create a block relaxation is to use the surrogate parameter \mathbf{X}^\dagger as an additional parameter block, i.e.

$$\begin{aligned}
& \underset{\mathbf{X}, \mathbf{X}^\dagger, \mathbf{d}}{\text{minimise}} \ g\left(\mathbf{X}, \mathbf{X}^\dagger, \mathbf{d}\right) \\
& \text{subject to; } \left\|\mathbf{X}\right\|_1 \leq \tau \\
& \quad d_m^* d_m = 1, \ m = 1, \dots, M.
\end{aligned} \tag{4.21}$$

For this relaxation, as long as Eq. (4.21) is always solved based on \mathbf{X}^\dagger after solving based on \mathbf{X} the solution for each sub-problem is easily computable and the complete algorithm is known to be stable and guaranteed to converge to an accumulation point or a connected set of accumulation points, see [137, Proposition B.3]. The pseudo code for this algorithm, when phase minimisation occurs at each iteration, is in Algorithm 4. Where, $\mathcal{P}_\tau(\mathbf{C})$ projects \mathbf{C} onto an ℓ_1 ball with a radius of τ .

Algorithm 4 $\mathcal{B}(\mathbf{X}, \mathbf{d})$

Input: $L_x > \left\|h\right\|_F^2$

Output: \mathbf{X}, \mathbf{d}

```

repeat
   $\mathbf{X}^\dagger \leftarrow \mathbf{X}$ 
   $\mathbf{C} \leftarrow \mathbf{X}^\dagger + L^{-1}h^H\left(\text{diag}\{\mathbf{d}\}\mathbf{Y} - h^H(\mathbf{X}^\dagger)\right)$ 
   $\mathbf{X} \leftarrow \mathcal{P}_\tau(\mathbf{C})$ 
   $\mathbf{d}^\dagger \leftarrow \mathbf{d}$ 
   $\mathbf{d} \leftarrow \exp\left(j\angle \text{diag}\left\{h(\mathbf{X})\mathbf{Y}^H\right\}\right)$ 
until  $\left\|\mathbf{X} - \mathbf{X}^\dagger\right\|_F \left\|\mathbf{X}^\dagger\right\|_F^{-1} < \text{threshold} \wedge \left\|\mathbf{d} - \mathbf{d}^\dagger\right\|_2 \left\|\mathbf{d}^\dagger\right\|_2^{-1} < \text{threshold}$ 

```

It is interesting to note that this algorithm can be seen as a generalisation of Algorithm 3.

Table 4.1: System parameters for synthetic experiments

parameter	value
carrier frequency ($\omega_0/2\pi$)	10 GHz
chirp bandwidth ($\alpha T/\pi$)	150 MHz
scene radius (L)	50 m
number of targets	20
signal to noise ratio	0 dB

An additional benefit of Algorithm 4 is that it tends to converge faster than Algorithm 3. This is because Algorithm 3 will oscillate around the optimum path.

4.6 Experimental Results

In these experiments we investigate the performance of the two different block relaxations, Algorithm 3 and Algorithm 4, using undersampled phase histories that contain phase errors.

4.6.1 Quantitative Performance

In the first experiment, we investigate the empirical convergence rate and reconstruction performance of Algorithm 3 and Algorithm 4. In order to easily compare with post-processing autofocus techniques, we considered the separable model in Eq. (4.5). In this experiment the scene consists of a small number of constant amplitude point targets randomly placed in the scene. The under-sampling consists of selecting a random subset of the fully-sampled synthetic aperture. Two different phase errors were considered: quadratic phase errors $\phi_m = \gamma((m-1)/M)^2$ which model platform velocity measurement errors and normally distributed phase errors $\phi_m = \mathcal{N}(0, \gamma^2)$. The parameters for the synthetic model are in Table. 4.1.

Convergence

In this experiment, we compare the number of iterations it takes Algorithm 3 and Algorithm 4 to reach the stopping criterion when the threshold is 10^{-6} . In order to fairly compare the two algorithms, we compute the operation \mathcal{D} in Algorithm 3 using the “majorisation minimisation” method from Section 4.5.1. We also define the number of iterations in each algorithm to be the total number of times the gradient of the objective function has to be computed with respect to \mathbf{X} . We select this definition because the main computational cost of both algorithms is consumed by computing this gradient, therefore, the iterations count will closely relate to the execution time of the algorithm. We choose to show the results for normally distributed phase errors with $\gamma = 10$. This is because the type and magnitude of phase errors was found to have only a minor effect on the results.

As expected, Fig. 4.1(a) shows that Algorithm 4 requires many less iterations than Algorithm 3. This is likely to be due to the minimisation path of Algorithm 3 oscillating around

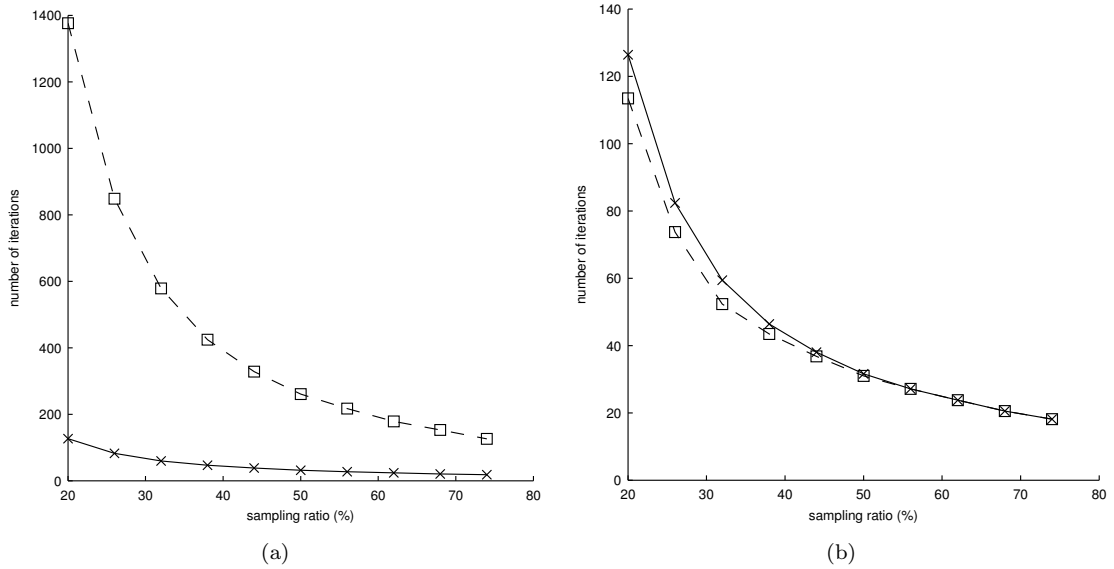


Figure 4.1: Comparison of empirical convergence rates. (a) ‘□’ Algorithm 3 and ‘×’ Algorithm 4. (b) ‘□’ Algorithm 4 with continuation and ‘×’ Algorithm 4.

Table 4.2: Continuation parameters

sampling ratio (%)	20	26	32	38	44	50	56	62	68	74
I	30	20	10	5	3	2	1	1	1	1

the optimal minimisation path.

A technique known as continuation has been found to be useful for increasing the numerical convergence rate of ℓ_1 sparse recovery algorithms when there is no phase errors [70]. Continuation involves varying the value of τ during the iterations of the algorithm. The motivation for this technique is based on the observation that the convergence rate depends on τ . The smaller the value of τ , the faster the algorithm will converge. Therefore, we can start with a small value of τ and increase its value in the following iterations until it reaches the desired final value.

In order to further improve the convergence rate of our algorithm we experimented with such a continuation scheme. Although we did not see any singularity in the modified algorithm with this setting, the convergence and stability would need to be proved in the future.

In this simulation we used a continuation scheme that involved changing τ during the first I iterations by the empirical rule $\tau_i = i\tau/I$ for $i = 1, \dots, I$. The selection of a “good” I depends on the undersampling so we used the values of I in Table 4.2, which were selected empirically for each undersampling percentage.

Fig. 4.1(b) shows a small improvement in performance when continuation is used. Another method for reducing the required number of iterations would be to use a more aggressive step size [9], similar to that used in other iterative ℓ_1 sparse recovery algorithms [129, 63]. Using this

type of step size, the stability of the algorithm cannot be guaranteed, but in practise it may also be useful.

Reconstruction Error

In order to assess the image reconstruction performance of the autofocus methods we define an image quality metric. Since the autofocus problem is ambiguous to scalar multiplication by $\beta \in \{\beta \in \mathbb{C} : |\beta| = 1\}$ and cyclic permutation, we define a metric that is immune to these ambiguities. We will refer to this metric as relative SNR and define it as

$$\underset{\beta, n}{\text{minimise}} \left\{ 10 \log_{10} \left(\frac{\|\tilde{\mathbf{X}}\|_{\text{F}}^2}{\|\tilde{\mathbf{X}} - \beta \mathbf{P}^m \mathbf{X}\|_{\text{F}}^2} \right) \right\},$$

Fig. 4.3 shows the performance of the sparse image formation with post-processing autofocus and Algorithm 4 with different phase errors. We do not show the results of Algorithm 3 because the results are virtually identical to that of Algorithm 4. The magnitude of the corresponding filters for each of the phase errors, the rows of Ψ , are shown in Fig. 4.2.

To provide an empirical upper-bound, we also show the image formation performance that can be achieved with oracle knowledge of the phase errors and also the locations of the targets, we refer to this as the oracle image formation. The oracle image formation recovers an image as follows: it first corrects the phase errors in the phase history such that it has no phase errors. It then uses the known location of the targets to perform a LS estimate of the target reflectivities. This problem is overdetermined since there are K reflectivities and MN , $MN > K$, measurements.

The sparse image formation with post-processing autofocus is performed as is described in Section 4.3. Firstly, an ℓ_1 -norm spectral projected gradient (SPG) method [15] is used to recover the filtered image $\tilde{\Psi} \mathbf{X}$ then the image is recovered from the filtered image using the reference phase errors $\tilde{\phi}$.

These reference phase errors are selected slightly differently for the two different types of phase errors. When the phase errors are quadratic, $\tilde{\phi}$ is selected to be equal to the true phase errors, even for the phases associated with unobserved measurements. This is because the CS reconstruction tends to approximate the blurred image. However, when the phase errors are random, $\tilde{\phi}$ is selected to be equal to the true phase error at the M indices corresponding to the observed aperture measurements and 0 at all indices corresponding to unobserved aperture measurements. The reason for this difference is because for the random phase errors, unlike quadratic phase errors, each of the phase errors is independent. This means that the phase errors associated with the unobserved measurements have no effect on the sparse image formation algorithm, therefore, it does not make sense to use them in $\tilde{\Psi}^{-1}$. In comparison, setting the unobserved phase errors to zero slightly increases the reconstruction performance.

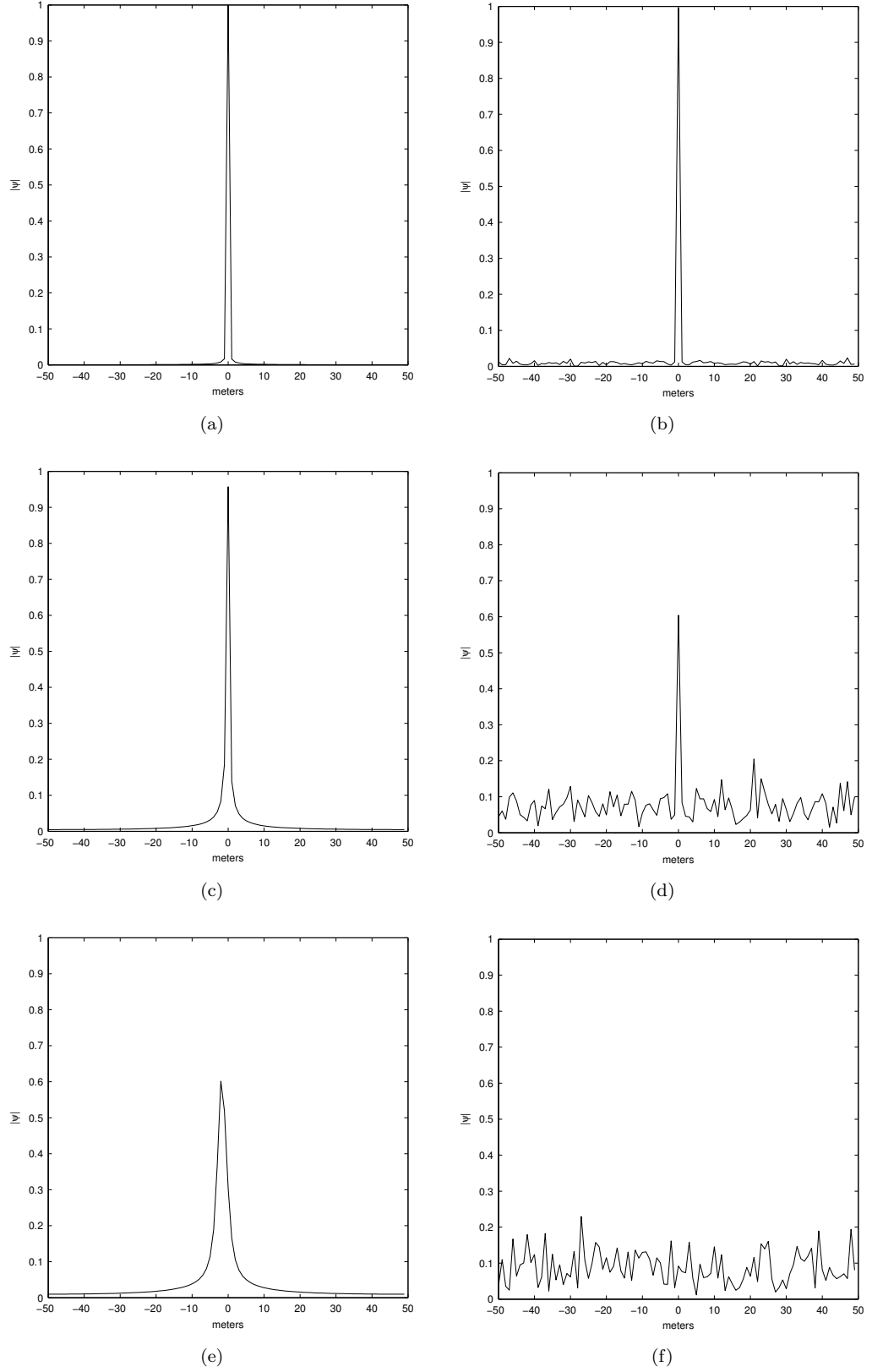


Figure 4.2: Phase error induced filters (the rows of Ψ for quadratic and random phase errors with different γ). Quadratic: (a) $\gamma = 0.1$ (c) $\gamma = 1$ (e) $\gamma = 10$. Random: (b) $\gamma = 0.1$ (d) $\gamma = 1$ (f) $\gamma = 10$.

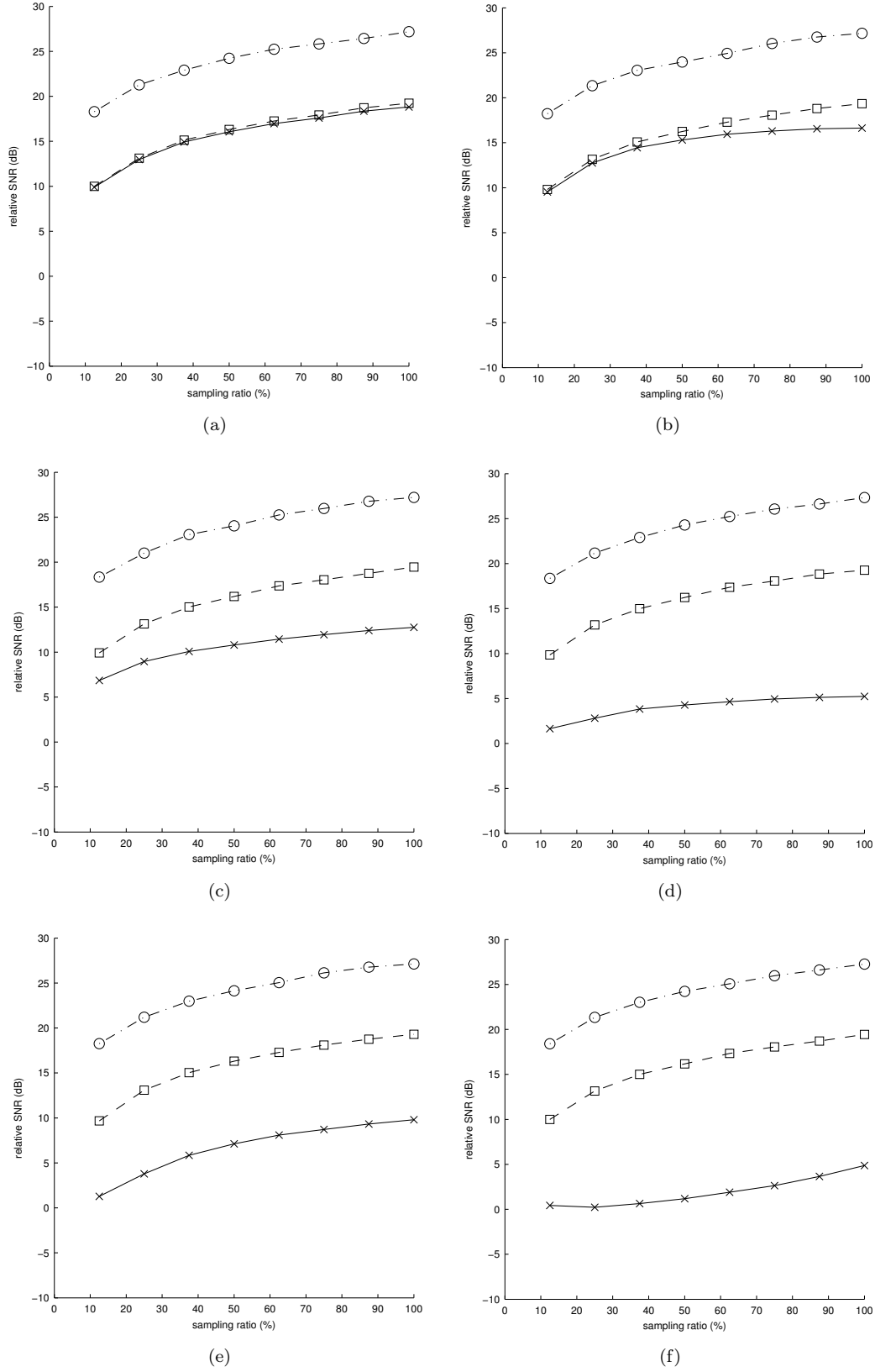


Figure 4.3: Image formation performance performance versus undersampling ratio: ‘o’ oracle image formation, ‘□’ Algorithm 4 and ‘×’ sparse image formation and post-processing autofocus with reference phase errors. Quadratic: (a) $\gamma = 0.1$ (c) $\gamma = 1$ (e) $\gamma = 10$. Random: (b) $\gamma = 0.1$ (d) $\gamma = 1$ (f) $\gamma = 10$.

To understand the results of Fig. 4.3, the sources of errors in the reconstructed image should be considered. The three sources of errors in a reconstructed image are the additive noise, the undersampling and the phase errors. For the oracle reconstruction the only source of error is due to the additive noise. The performance degrades with the sampling ratio because the denoising effect of the LS estimate degrades as the ratio MN/K decreases. For the sparse image formation with autofocus, the sparse image formation will try to minimise the errors associated with the undersampling and also will implicitly denoise. This process will be more successful if the filtered image is approximately sparse. The post-processing autofocus will then try to reduce the errors associated with the phase errors. Algorithm 4 also minimises the effect of undersampling and phase errors and implicitly denoises.

As predicted in Section 4.3, as the phase errors increase, the performance of sparse image formation with post-processing autofocus decreases. It is also interesting to note that this method's performance is better for quadratic phase errors than for random phase errors. This is because the filter corresponding to the quadratic phase errors is approximately sparse while than the filter corresponding to the random phase errors is not. Hence, the sparse image formation for quadratic phase errors is more effective at reducing the errors associated with the undersampling and the additive noise.

The performance of Algorithm 4, which is in contrast to the performance of sparse image formation with post-processing autofocus, is consistently good for both types of phase errors. In fact, it achieves a performance, even with large phase errors, that is similar to a sparse image formation without phase errors. The SNR gap between the performance of Algorithm 4 and the oracle image formation is primarily due to the shrinkage effects of ℓ_1 -minimisation. This gap could potential be reduced by an additional procedure known as “debiasing” [63].

4.6.2 Qualitative Performance

In these experiments we wish to show that the presented algorithm works on realistic simulations of our two motivating scenarios, i.e. multifunction and UWB SAR. The scene used in both simulated scenarios consists of four point targets which reflect back an equal amount of energy.

UWB SAR

As mentioned previously, under sampling occurs in a UWB SAR system when notches are introduced into the transmitted chirp in order to avoid interference with other users. In this simulation, we used a notched linear frequency chirp, which had a spectral density that is given in Fig. 4.4. The chirp contains five notches which equate to a nulling of approximately 20% of the chirp spectrum. The other parameters of the simulation are given in Table 4.3.

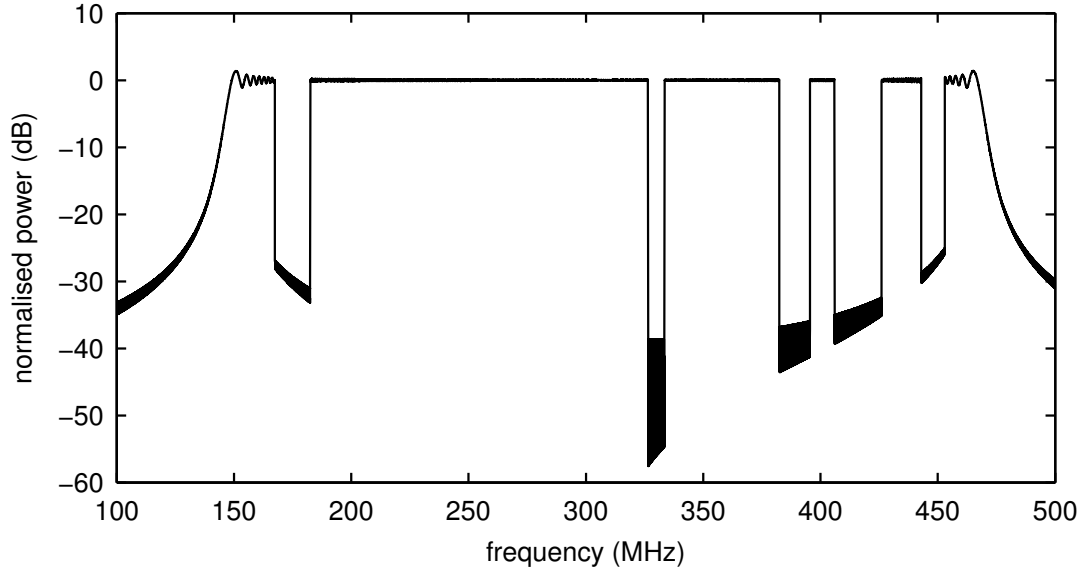


Figure 4.4: Power spectral density of notched linear frequency chirp.

Table 4.3: System parameters for simulated UWB SAR

parameter	value
carrier frequency ($\omega_0/2\pi$)	308 MHz
chirp bandwidth ($\alpha T/\pi$)	324 MHz
IF bandwidth	20 MHz
altitude	7000 m
stand-off distance	7000 m
aperture length	7000 m
number of aperture samples	200
scene radius (L)	75 m
number of targets	4
signal to noise ratio	0 dB
timing errors	$\mathcal{N}(0, 0.8)$ ns

Table 4.4: System parameters for simulated multifunction SAR

parameter	value
carrier frequency ($\omega_0/2\pi$)	10 GHz
chirp bandwidth ($\alpha T/\pi$)	600 MHz
IF bandwidth	30 MHz
altitude	7000 m
stand-off distance	7000 m
aperture length	250 m
number of aperture samples	300
scene radius (L)	75 m
number of targets	4
signal to noise ratio	0 dB
timing errors	$\mathcal{N}(0, 25)$ ps

Multifunction SAR

In this simulation a randomly undersampled aperture of an X-band SAR system is used to simulate a multifunction SAR system. The phase history contains a 50% random subset of the fully-sampled aperture. The other parameters of the simulation are given in Table 4.4.

For both scenarios, three SAR images were formed using different image formation methods. One image in each scenarios was generated using filtered fast decimation-in-image BP algorithm without any form of autofocus. Another was generated using 20 iterations of an ℓ_1 -norm SPG method again without any form of autofocus. The last image was created using 20 iterations of the modified Algorithm 4 which uses continuation with $I = 15$. The final value of τ was selected to be the sum of the absolute values of the target reflectivities. However, the reconstruction performance was found to be not particularly dependent on this parameter. In a real system a suitable τ could be selected with only a coarse degree of parameter tuning. In the iterative reconstruction algorithms both the observation model and its adjoint ($h(\cdot)$ and $h^H(\cdot)$) are computed using the fast decimation-in-image BP and RP algorithms.

The resulting images from both simulation scenarios are contained in Fig. 4.5 and Fig. 4.6. Fig. 4.5(a) and Fig.4.6(a) demonstrate the adverse effects of phase errors and undersampling. The sidelobes of the four targets contain a large amount of energy which deteriorates the SAR image quality. The images in Fig. 4.5(c) and Fig.4.6(c), which were produced using an ℓ_1 -norm SPG method, have an improved visual quality over the previous images due to the sparsity promoting algorithm. However, due to the model inaccuracies there are a large number of non-zeros pixels that may be mistaken for additional targets. Finally, Fig. 4.5(e) and Fig.4.6(e) show the results of Algorithm 4. In these images the energy from each target is highly concentrated around the target locations. It is clear that in these scenarios Algorithm 4 can produce a visually improved SAR image, with a sparse number of point targets, from a phase history that is undersampled and contains model inaccuracies.

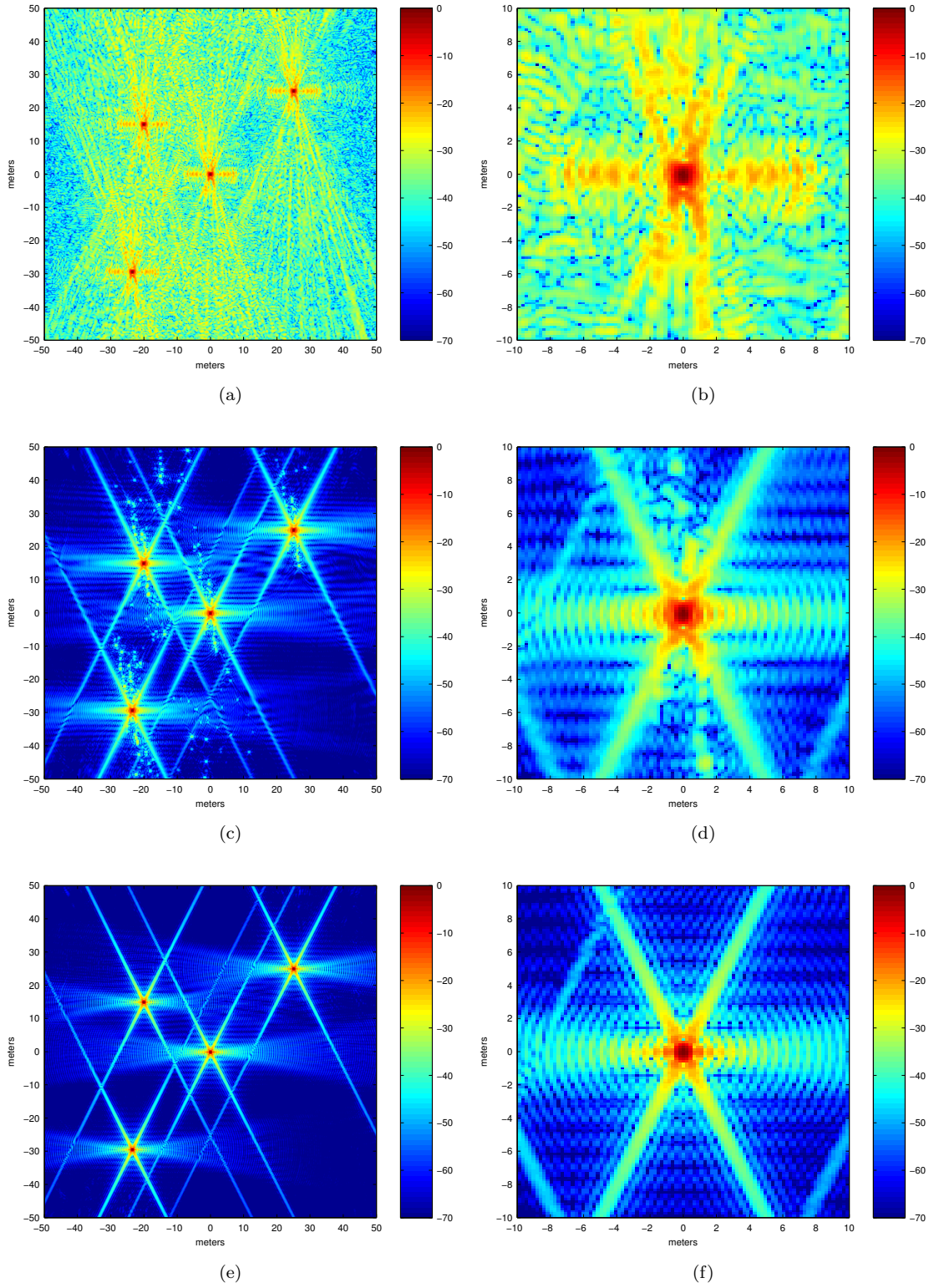


Figure 4.5: UWB SAR image formations: (a) was formed using filtered BP algorithm, (c) was formed using an ℓ_1 -norm SPG method and (e) was formed using Algorithm 4. (b), (d) and (f) are a zoomed in view of (a), (c) and (e) around the origin, respectively.

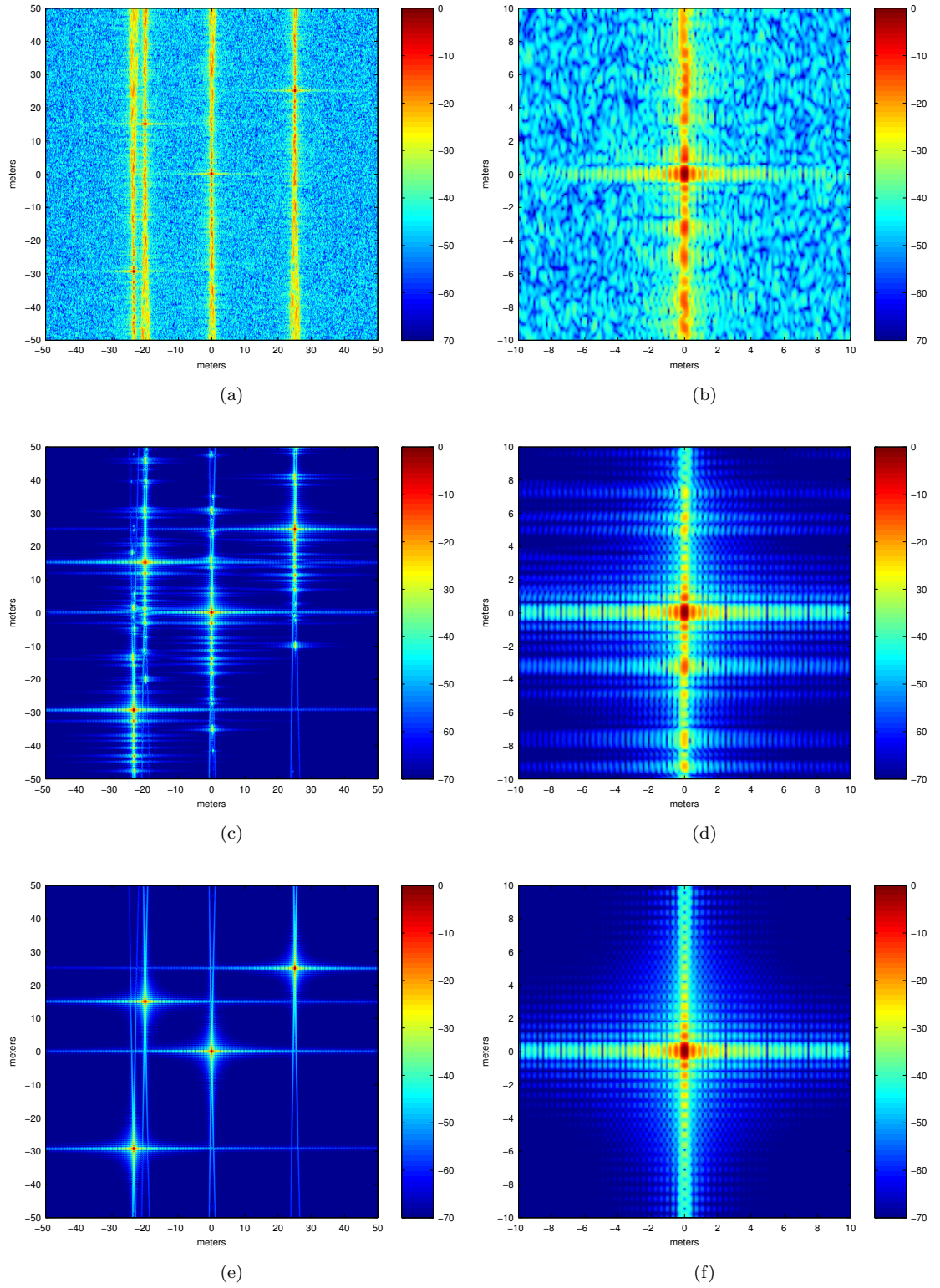


Figure 4.6: Multifunction SAR image formations: (a) was formed using filtered BP algorithm, (c) was formed using an ℓ_1 -norm SPG method and (e) was formed using Algorithm 4. (b), (d) and (f) are a zoomed in view of (a), (c) and (e) around the origin, respectively.

4.7 Summary

We have investigated the effects of phase errors on an undersampled SAR system. We have shown that post-processing autofocus algorithms are typically unsuitable when there is undersampling and a sparse image formation method is employed. Instead, phase errors should be corrected during the image formation.

We have proposed a new algorithm that corrects phase errors within the image formation algorithm. Algorithm 4, which is an algorithmically stable generalisation of a recently proposed non-convex sparsity based autofocus method, performs consistently well for a variety of phase errors and undersampling ratios and was found empirically to converge in a much smaller number of iterations.

We have also demonstrated through additional realistic simulations that Algorithm 4 could be used in practical non-standard SAR image formation systems to produce sparse SAR images from undersampled phase histories which contain model inaccuracies.

Although we have concluded that post-processing autofocus algorithms are typically unsuitable for undersampled SAR, there may be some instances where they may warrant further consideration. In the scenario where the undersampling is only in the range dimension, for example the UWB scenario, a sparsity based algorithm could be used to perform range compression and then a standard image formation algorithm could be used to form the final image which could then be autofocused using a standard post-processing algorithm. CS theory suggests that this will be sub-optimal, however, these types of methods may be justified as a means of reducing complexity. Further research into autofocus and image formation algorithms for undersampled data, where there are specific system constraints, could be an avenue for future research.

Chapter 5

Ultra-Wideband Synthetic Aperture Radar

5.1 Introduction

UWB SAR systems that use the VHF/UHF bands find civilian and military applications primarily due to the foliage penetration property of large wavelength RF waves [98]. A major problem for VHF/UHF SAR systems are radio, television and communications systems. The presence of these systems can produce two types of RFI. One occurs when the SAR system interferes with other users. The second occurs when other users interfere with the SAR system. The first type of RFI is strictly regulated and therefore certain specified bands must be avoided. The second type of interference occurs within the bands where transmission is allowed. Strong interference from other users within these bands, particularly from narrowband (AM and FM) transmitters, can deteriorate the dynamic range of the resulting SAR image.

In most areas of the world it is not possible to get a license to operate a UWB radar unless it satisfies the relevant guidelines on spectrum compliance. Critical frequencies must be avoided to prevent interference to civilian and governmental communications systems. To avoid these critical frequencies, two main strategies exist. These strategies are *frequency jump burst* and *notched LFM chirp* waveforms. A frequency jump burst system uses narrowband pulses to jump from one frequency sub-band to the next avoiding the proscribed frequencies. The Swedish CARABAS UWB SAR system uses this type of waveform [72]. For a notched LFM chirp waveform the standard LFM chirp is used with spectral notches added. The centre and width of these notches are selected such that the system meets the power spectral requirements at the proscribed frequencies. A notched LFM chirp is used for systems that require fine range resolution. An example of a system that uses this waveform is the ERIM P-3 UWB SAR [117].

The effect of the missing frequencies in the transmit waveform is to increase the sidelobes

levels in the formed image. There have been a number of methods proposed to decrease these introduced sidelobes. These include windowing based methods [48] and sparsity based algorithms [34, 102].

To achieve a reasonable level of performance, a VHF/UHF SAR system must include a method of RFI removal/suppression. RFI suppression is usually achieved by estimating and subtracting the RFI [92, 66] or linearly filtering each radar return, e.g. [86, 1, 123, 91]. Estimate-and-subtract methods assume that the RFI consists of a small number of very narrow-band signals which can each be well approximated by a sine wave. These methods estimate each signals amplitude, frequency and phase and then subtract them from the radar return. The effectiveness of these methods depend heavily on the narrow-band approximation of the interferers. They also have a large computational complexity if the RFI is dense and made up of a large number of interferers. For this reason it is often preferable to use linear filtering. One problem with a filtering based approach is that the filtering can produce large range sidelobes in the formed image. This is due to the large signal suppression that occurs within the spectral regions where the signal is dominated by RFI. To avoid these negative effects, sidelobe suppression methods are proposed in [86] and [1].

In this chapter we propose a new SAR image formation algorithm which simultaneously suppresses RFI and produces a SAR image without introducing large range side lobes. The method is tailored for SAR systems that use dechirp-on-receive. Dechirp-on-receive is primarily used to reduce the required sample rate of the receiver's ADC but also has the advantage that it removes a large proportion of the RFI [66]. The proposed method achieves the desired outcomes by leveraging the approximate sparsity of SAR images (where sparsity implies only a small number of image pixels have a magnitude which is significant). The method is therefore most similar to the method proposed in [1] which uses a greedy algorithm to leverage the image sparsity. The approximate sparsity of a SAR image is a valid assumption if the scene is made up of point-like targets in clutter. Image sparsity based methods have previously been applied to SAR systems without RFI [34, 102]. The algorithm can also be used to minimise the effects of transmit notching. Therefore, our method can be seen to be an extension of these sparsity based methods to include RFI suppression.

5.2 Ultra-wideband Observational Model

5.2.1 Notched Linear Frequency Modulated Chirp on Transmit

When designing a notched LFM chirp signal for the transmitted signal of a UWB SAR system, the centre frequencies of the notches and their notch bandwidth, that are required to avoid interference, will be known. The design of the transmitted waveform, therefore, can be generated deterministically and be synthesised for transmission using a digital waveform generator.

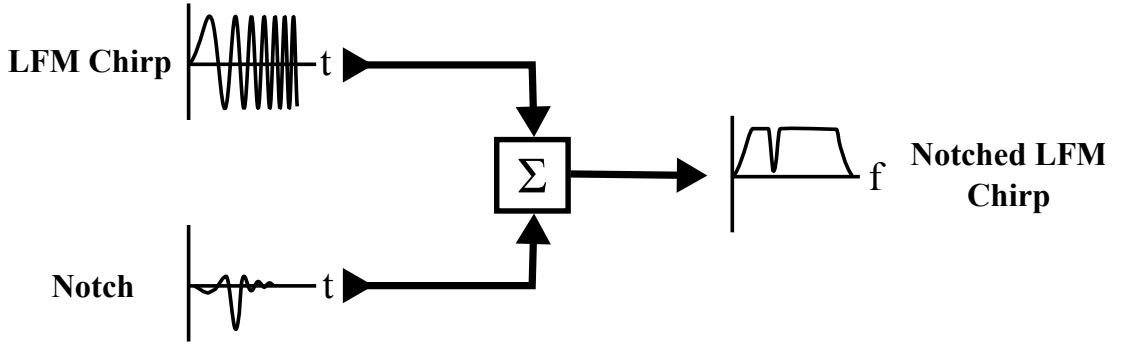


Figure 5.1: Transmitter notching of LFM chirp.

The spectrum of a standard complex LFM chirped signal

$$s(t) = \text{rect}(t/T_s) \exp(j(\omega_0 t + \alpha t^2)), \quad (5.1)$$

where, T_s is the chirp period, ω_0 is the carrier frequency and 2α is the chirp rate, is given by

$$\begin{aligned} S(\omega) &= \left[\sqrt{\frac{j\pi}{\alpha}} \exp\left(-j\frac{(\omega - \omega_0)^2}{4\alpha}\right) \right] * \left[T_s \text{sinc}\left(\frac{T_s \omega}{2}\right) \right] \\ &\approx \sqrt{\frac{j\pi}{\alpha}} \text{rect}\left(\frac{\omega - \omega_0}{2\alpha T_s}\right) \exp\left(-j\frac{(\omega - \omega_0)^2}{4\alpha}\right). \end{aligned} \quad (5.2)$$

Therefore, to introduce a single notch into the spectrum of the chirp signal we can subtract the region of the spectrum that corresponds to the desired notch. This is written in the Fourier domain as

$$\tilde{S}(\omega) = S(\omega) - \sqrt{\frac{j\pi}{\alpha}} \text{rect}\left(\frac{\omega - \omega_1}{2\pi B_1}\right) \exp\left(-j\frac{(\omega - \omega_0)^2}{4\alpha}\right), \quad (5.3)$$

where, ω_1 is the centre frequency of the notch and B_1 is the bandwidth of the notch.

This procedure is illustrated visually in Fig. 5.1. The full LFM chirp signal is added to the negative of the notching signal to produce a LFM signal that contains a notch in its spectrum at the desired centre frequency and notch bandwidth. This process is repeated for each notch that is required.

Clearly, the adding of notches to the transmitted LFM chirp will effect the range sidelobes in the SAR image if it formed using standard image formation algorithms. This is demonstrated in Fig. 5.2. Five notches were added to a LFM chirp to produce a notched LFM chirp. The result of these notches is that the range ambiguity function of the notched LFM chirp has much larger sidelobes than the range ambiguity function of the original LFM chirp. This effect will increase with an increasing size and number of notches.

In a dechirp-on-receive SAR system, the received signal undergoes a process of dechirping and sometimes deskewing before the phase history is stored or sent to the image formation

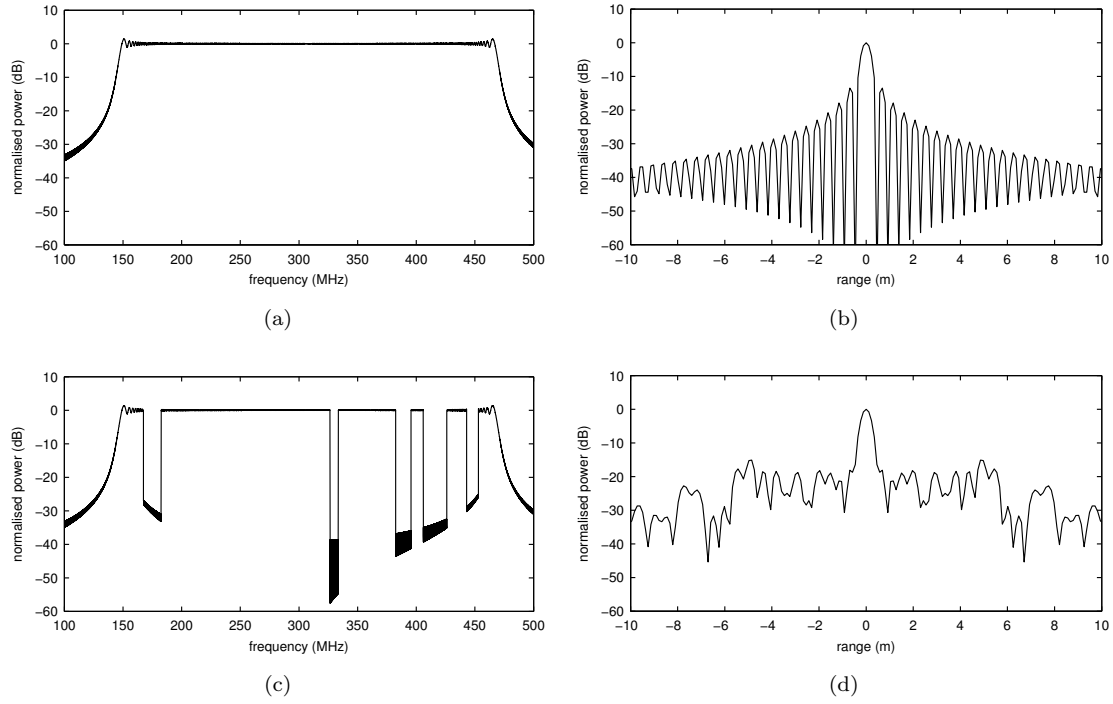


Figure 5.2: Spectrum and range ambiguity function of LFM and notched LFM chirp. The parameter for the LFM chirp are: centre frequency is 308 MHz, the chirp bandwidth is 324 MHz, the chirp period is $10 \mu\text{s}$. The parameters for the notches are: the notch centre frequencies of the notches are 175, 330, 389, 416 and 448 MHz, the notch bandwidths are 15, 7, 13, 20 and 10 MHz. (a) is the spectrum of the LFM chirp signal. (b) is the range ambiguity function of the LFM chirp signal. (c) is the spectrum of the notch LFM chirp signal. (d) is the range ambiguity function of the notched LFM chirp signal.

processor. The effect of the notches on the received signal, using the model developed in Chapter 2 for a dechirp-on-receive SAR system, is approximately given by

$$\tilde{y}(t) \approx |S(\omega_0 + 2\alpha t)| y(t), \quad (5.4)$$

where, $y(t)$ is the signal that would have been received if there were no notches. This effect is demonstrated visually in Fig. 5.3, where the received signal contains returns from three targets. The spectral notches in the transmitted signal appear as notches in the fast-time of the received signal.

Using a model for the transmit notching, a discrete observation model for a notched LFM chirp SAR system, after it has been dechirped and deskewed, is given by

$$\mathbf{Y} = \text{diag}(\mathbf{s})h(\mathbf{X}), \quad (5.5)$$

where,

$$s_m = \left| S\left(\omega_0 + 2\alpha\left(\frac{m-1}{f_t} - \frac{T_t}{2}\right)\right) \right| \quad (5.6)$$

models the effect of the transmit notching.

5.2.2 Radio Frequency Interference

A further refinement of the observation model for UWB SAR is to include additive components of the phase history that are not a result of reflections from the scene. These components include RFI and other forms of additive noise. The model then becomes

$$\mathbf{Y} = \text{diag}(\mathbf{s})h(\mathbf{X}) + \mathbf{N}, \quad (5.7)$$

where, $\mathbf{N} \in \mathbb{C}^{M \times N}$ models the dechirped and deskewed RFI and noise.

To understand how RFI appears in \mathbf{N} , consider a single deterministic RFI tone

$$s_{\text{rfi}}(t) = A \exp(j\omega_{\text{rfi}}t), \quad (5.8)$$

where, A is the complex magnitude and ω_{rfi} is the frequency of the tone. After dechirping and deskewing the signal resulting from the RFI tone is approximately given by

$$s_{\text{rfi}}(t) \approx A \sqrt{\frac{\pi}{j\alpha}} \frac{\omega_{\text{if}}}{2\pi} \exp\left(j\frac{(\omega_{\text{rfi}} - \omega_0)^2}{4\alpha}\right) \text{sinc}\left(\frac{\omega_{\text{if}}\left(t - \frac{(\omega_{\text{rfi}} - \omega_0)}{2\alpha}\right)}{2}\right), \quad (5.9)$$

where, ω_{if} is bandwidth of the intermediate frequency filtered which occurs after the dechirping [66]. The effect of the intermediate frequency bandwidth is two fold, the larger the bandwidth the closer the RFI tone is to an impulse and the smaller the bandwidth the less the

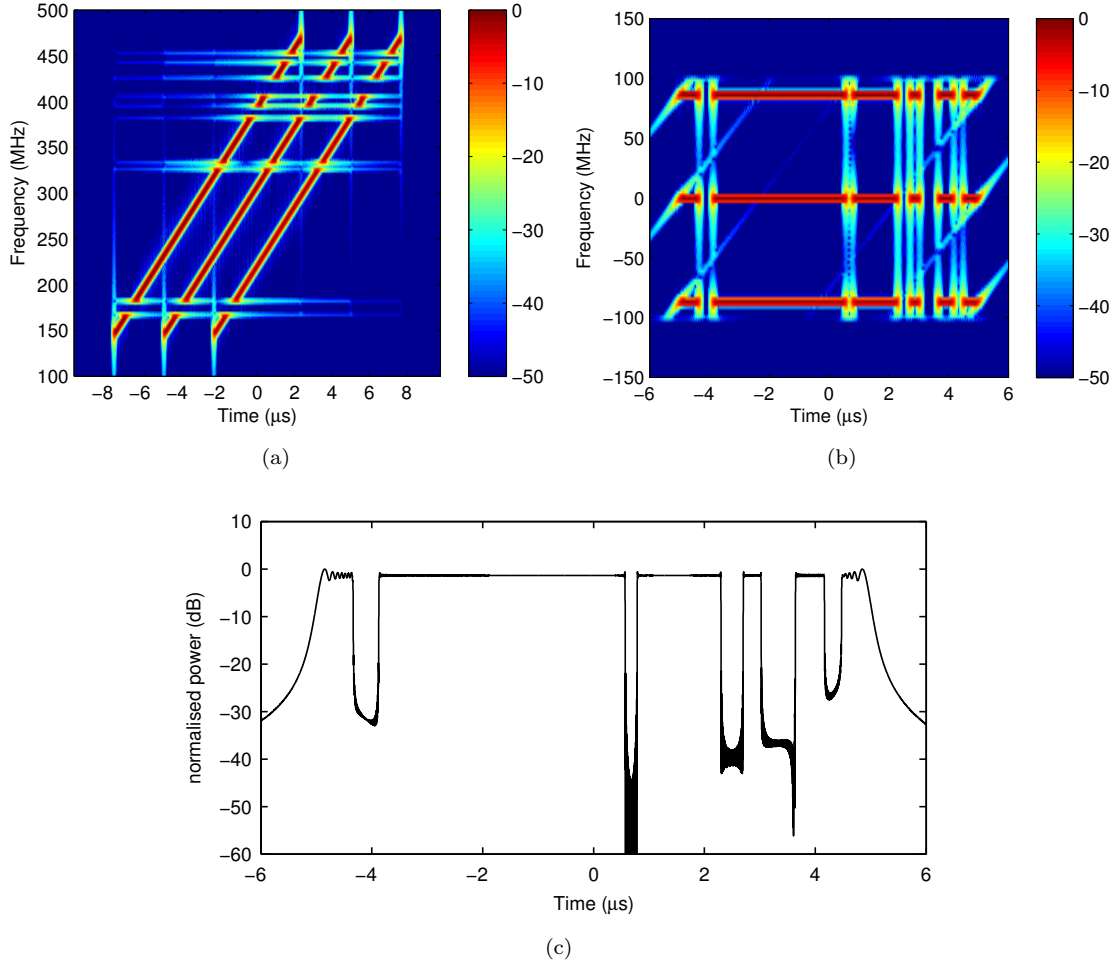


Figure 5.3: Range returns from three targets with a notched LFM chirp before and after dechirping and deskewing. The parameter for the LFM chirp are: centre frequency is 308 MHz, the chirp bandwidth is 324 MHz, the chirp period is 10 μ s. The parameters for the notches are: the notch centre frequencies of the notches are 175, 330, 389, 416 and 448 MHz, the notch bandwidths are 15, 7, 13, 20 and 10 MHz. Targets are located at 0, +400 and -400 m (relative to the centre of the scene). (a) is a spectrogram of the received signal before dechirping and deskewing. (b) is a spectrogram of the received signal after dechirping and deskewing. (c) is the spectrum of the received signal from just the target at 0 m after dechirping and deskewing.

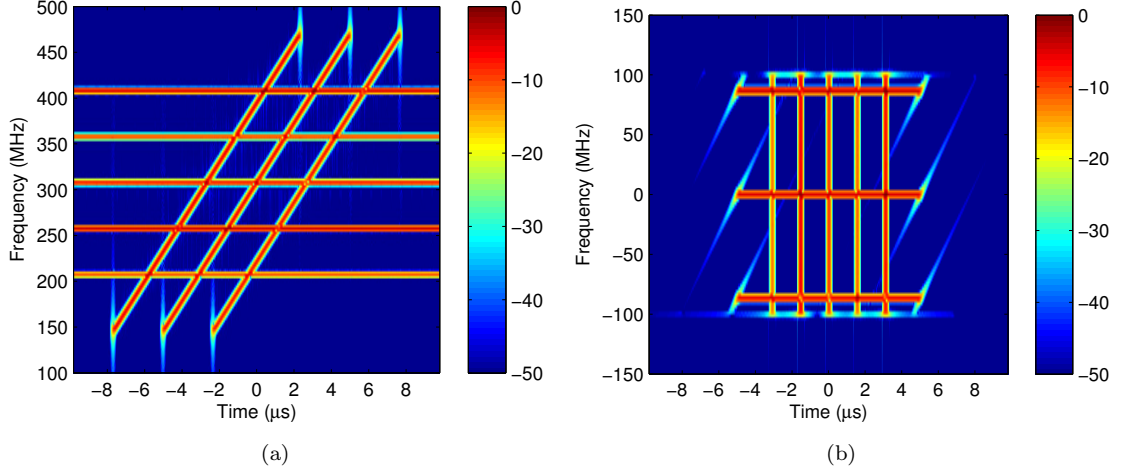


Figure 5.4: Range returns from three targets with a LFM chirp and five RF interferers, before and after dechirping and deskewing. The parameter for the LFM chirp are: centre frequency is 308 MHz, the chirp bandwidth is 324 MHz, the chirp period is 10 μ s. Targets are located at 0, +400 and -400 m (relative to the centre of the scene). RF interferers at 208, 258, 308, 358 and 408 MHz. (a) is a spectrogram of the received signal before dechirping and deskewing. (b) is a spectrogram of the received signal after dechirping and deskewing.

amplitude of the RFI tone. If the $s_{\text{rfi}}(t)$ is the total RFI and its Fourier transform is given by $S_{\text{rfi}}(\omega)$, then the RFI signal after dechirping and deskewing is approximately given by

$$\tilde{s}_{\text{rfi}}(t) \approx \left[\frac{1}{2\pi} S_{\text{rfi}}(\omega_0 + 2\alpha t) \exp(j\alpha t^2) \right] * \left[\sqrt{\frac{\pi}{j\alpha}} \frac{\omega_{\text{if}}}{2\pi} \text{sinc}\left(\frac{\omega_{\text{if}} t}{2}\right) \right], \quad (5.10)$$

If $s_{\text{rfi}}(t)$ is a random signal then the $\mathbb{E}\left(|\tilde{s}_{\text{rfi}}(t)|^2\right)$ will be the PSD of $s_{\text{rfi}}(t)$ convolved with a squared sinc function.

The effect of dechirping and deskewing on the RFI is demonstrated visually in Fig.5.4. In this example the received signal contains returns from three targets and the PSD of the RFI contains three impulses at five different frequencies. Before dechirping the RFI consists of five discrete frequencies. After dechirping and deskewing, the RFI is concentrated into five discrete time instances. It is also clear that the IF filter has also removed some of the RFI.

5.3 Linear Filter based RFI Suppression

A linear filter based RFI suppression algorithm applies a filter to each radar return. The filter is selected such that the phase history is as close to the true phase history, without RFI, as possible. After filtering, the image is formed using a standard image formation algorithm. This can be written as

$$\hat{\mathbf{X}} = g(\mathbf{H} \text{vec}(\mathbf{Y})), \quad (5.11)$$

where, $\mathbf{H} = \text{diag}([\mathbf{H}_1, \dots, \mathbf{H}_N])$ is a block diagonal matrix which contains the N filters for each radar return and $g(\cdot)$ is a standard image formation algorithm. If the entries of each \mathbf{n}_n and \mathbf{y}_n are stationary then the optimal filter in the minimum mean squared error (MMSE) sense will be the Wiener filter $\mathbf{H}_n = \mathbf{I} - \mathbf{Q}_{\mathbf{n}n} (\mathbf{Q}_{\mathbf{y}n} + \mathbf{Q}_{\mathbf{n}n})^{-1}$, where, $\mathbf{Q}_{\mathbf{n}n}$ and $\mathbf{Q}_{\mathbf{y}n}$ are the covariance matrices of each column of \mathbf{N} and \mathbf{Y} , respectively.

In practise, an approximation of the Wiener filter can be computed using estimated statistics of the RFI which are obtained during the receiver “dead-time” (when there is no energy from radar signal being received, only RFI). Due to the properties of the dechirping and deskewing operations analysed in previous section, the RFI in each fast-time sample is approximately independent (this approximation depends on the IF bandwidth). Therefore, the RFI covariance matrices are approximately diagonal and can be estimated from the squared magnitudes of the samples of the dead-time returns. Multiple dead-time measurements can also be combined to improve the variance of these estimates. As has been suggested in other work, many methods can also be used to improve the RFI covariance estimates such as methods that use prior information or a parametric model [1].

For simplicity, if we consider an idealised problem where there is no transmit notching and the image formation algorithm is the pseudoinverse, then we can define an error bound on the image formation error due to the RFI. If an image is formed as $\hat{\mathbf{X}} = h^\dagger (\mathbf{H} \text{vec}(\mathbf{Y}))$ then

$$\left\| \mathbf{X} - \hat{\mathbf{X}} \right\|_{\text{F}} \leq \|h^\dagger(\cdot)\| (\|(\mathbf{I} - \mathbf{H}) \text{vec}(h(\mathbf{X}))\|_{\text{F}} + \|\mathbf{H} \text{vec}(\mathbf{N})\|_{\text{F}}), \quad (5.12)$$

where, \mathbf{X} is the true image. This can be compared with a bound for an image formed without linear filtering. If an image is formed as $\hat{\mathbf{X}} = h^\dagger(\mathbf{Y})$ then

$$\left\| \mathbf{X} - \hat{\mathbf{X}} \right\|_{\text{F}} \leq \|h^\dagger(\cdot)\| \|\mathbf{N}\|_{\text{F}}. \quad (5.13)$$

If we compare the two error bounds we can observe the effect of the linear filter. The filter \mathbf{H} reduces the error term which is dependent on \mathbf{N} but also introduces an error term which is dependent on the SAR image \mathbf{X} . This error is seen in the image as sidelobes.

5.4 RFI-aware Sparse Image Formation

Ideally, we want an image formation algorithm for UWB SAR to minimise the effect of the RFI without introducing errors which are dependent on the image (sidelobes). Therefore, we propose solving a modified BPDN optimisation program. The BPDN is modified such that it makes use of the RFI covariance estimate. This modified program is given by

$$\begin{aligned}\hat{\mathbf{X}} &= \underset{\mathbf{X}}{\text{minimise}} \|\mathbf{X}\|_1 \\ \text{subject to } &\|\mathbf{Y} - \text{diag}(\mathbf{s})h(\mathbf{X})\|_{\mathbf{Q}_N^{-1}} \leq \epsilon,\end{aligned}\tag{5.14}$$

where,

$$\|\mathbf{R}\|_{\mathbf{Q}_N^{-1}} = \langle \text{vec}(\mathbf{R}), \mathbf{Q}_N^{-1} \text{vec}(\mathbf{R}) \rangle\tag{5.15}$$

is a weighted Frobenius norm, $\mathbf{Q}_N = \text{diag}\left(\left[\mathbf{Q}_{\mathbf{n}_1}, \dots, \mathbf{Q}_{\mathbf{n}_{N'}}\right]\right)$ is a diagonal matrix whose elements contain an estimate of the RFI covariance, and $\epsilon \geq \|\mathbf{N}\|_{\mathbf{Q}_N^{-1}}$.

The motivation for Eq. 5.14 comes from two main factors. The ℓ_1 -norm objective is used because we want to promote sparse images and the weighted Frobenius norm constraint is used because we want the estimated image to match the measurements in a metric that takes into account the knowledge of the RFI. An equivalent optimisation program to Eq. 5.14 is

$$\begin{aligned}\hat{\mathbf{X}} &= \underset{\mathbf{X}}{\text{minimise}} \|\mathbf{X}\|_1 \\ \text{subject to } &\|\mathbf{Q}_N^{-1} \text{vec}(\mathbf{Y} - \text{diag}(\mathbf{s})h(\mathbf{X}))\|_2 \leq \epsilon,\end{aligned}\tag{5.16}$$

The solution of which can be obtained using any of the iterative algorithms which are used to solve the BPDN or any of its equivalent formulations.

Like in the previously proposed sparse image formation algorithms, the super resolution effects in the formed image $\hat{\mathbf{X}}$ can be removed by computing

$$\hat{\mathbf{X}} \leftarrow g\left(h\left(\hat{\mathbf{X}}\right)\right).\tag{5.17}$$

In order to define an error bound for the proposed algorithm, again we will ignore transmit notching. Additionally, an assumption on $h(\cdot)$ is also made. It is assumed that $h(\cdot)$ satisfies a modified RIP which we define as

$$C(1 - \delta_{2K})\|\mathbf{X}_{2K}\|_{\mathbb{F}}^2 \leq \|h(\mathbf{X}_{2K})\|_{\mathbf{Q}_N}^2 \leq C(1 + \delta_{2K})\|\mathbf{X}_{2K}\|_{\mathbb{F}}^2,\tag{5.18}$$

for all $\|\mathbf{X}_{2K}\|_0 \leq 2K$, where, $0 < \delta_{2K} < 3/(4 + \sqrt{6})$ and C is a positive constant [64]. It can be deduced from the theory of partial Fourier sampling that this property holds asymptotically with overwhelming probability if $h(\cdot)$ is a two-dimensional Fourier transform and there are $I = \mathcal{O}(MN - S \log^5(MN))$ randomly positioned point interferers [115]. Although these two conditions will not hold for a real SAR system, the conditions will likely be close enough to the real system as to provide a motivating theory. With this assumption an error bound for the RFI-aware sparse image formation (the solution to Eq. 5.16) is given by

$$\left\| \mathbf{X} - \hat{\mathbf{X}} \right\|_{\text{F}} \leq C_1 \|\mathbf{N}\|_{\mathbf{Q}_{\mathbf{N}}^{-1}} + C_2 K^{-1/2} \|\mathbf{X} - \mathbf{X}_K\|_1, \quad (5.19)$$

where, C_1 and C_2 are constants that depend only on δ_{2K} and C . Also, \mathbf{X}_K is \mathbf{X} restricted to its largest K elements. This error bound shows that if the SAR image is well-approximated by a sparse number of non zeros elements, the second term will be small and the image formation error will be almost optimally dependent on \mathbf{N} up to a constant C_1 .

5.5 Experiments

In this section we wish to demonstrate the effectiveness of the proposed algorithm on a simulated UWB SAR system with transmitter notching and receiver RFI. The simulation models a system which transmits a notched LFM chirp with five notches. The simulated scene consists of twenty randomly located targets which reflect back an equal amount of energy. Before the dechirp operation, RFI and white noise was added to each of the simulated radar returns. The RFI contains 80 randomly located narrowband interferers. The narrowband interferers are model as random signals with PSDs given by

$$\text{sinc}^2 \left(\pi \left(40 \cdot 10^{-6} \right) \left(\omega - 2\pi f_{\text{intf}} \right) \right) \quad (5.20)$$

where, f_{intf} is the centre frequency of the interferer. A detailed set of parameters used in the simulation are listed in Table. 5.1.

Using the simulated phase history, images were formed using three different image formation methods. The first method used the fast decimation-in-image BP algorithm without RFI suppression. The second method used linear filtering with a Wiener filter followed by the fast decimation-in-image BP algorithm. Finally we used two variants of our proposed RFI-aware sparse image formation method. The first variant is the algorithm proposed in Section. 5.4. The second variant is a modified version of the first variant but promotes sparsity in the range compressed signal rather than in the final image. Existing RFI suppression algorithms work in this domain, including a recently proposed sparsity based method [103]. Solutions of Eq. (5.16) where approximated using the FISTA algorithm [12] using the fast decimation-in-image RP and BP algorithms. Also, each RFI covariance matrix was estimated using the average of ten simulated dead-time measurements.

Fig. 5.5 shows the resulting four images. The image formed without RFI suppression is heavily contaminated with RFI and the targets are barely visible. The image formed using Wiener filtering is substantially better, however, the filtering has introduced sidelobes which could potentially be misinterpreted as additional targets. The image formed using the range compression based RFI-aware sparse image formation is again a further improvement. However, there is still image dependent errors. Finally, the RFI-aware sparse image formation image has

Table 5.1: System parameters for simulated UWB SAR

parameter	value
carrier frequency ($\omega_0/2\pi$)	308 MHz
altitude	7000 m
number of targets	20
chirp bandwidth ($\alpha T/\pi$)	324 MHz
stand-off distance	7000 m
number of interferes	80
IF bandwidth	60 MHz
aperture length	7000 m
signal to noise ratio (SNR)	60 dB
scene radius (L)	75 m
number of aperture samples	300
signal to interference ratio (SIR)	-30 dB
transmit notch centre frequencies	175, 330, 389, 416 and 448 MHz
transmit notch bandwidths	15, 7, 13, 20 and 10 MHz

the best visual image quality. The transmit notching and receiver RFI seems to have almost no visual impact on the formed image.

To quantitatively assess the quality of each SAR image a constant false alarm rate (CFAR) target detector was used on each image with a constant probability of false alarm rate of 0.0001%. For each dimension, the cell under test was selected to be four pixels with 20 guard pixels and two background pixels to estimate the detection threshold. The CFAR sliding window was moved across the image and the corresponding detection results are shown in Fig. 5.6. The RFI-aware sparse image formation algorithm had the best detection performance, detecting all twenty targets. For the range compression RFI-aware sparse image formation algorithm, however, six targets were missed. The Wiener filtering method missed nine targets and finally the fast BP algorithm with no RFI suppression missed all the targets.

5.6 Summary

In this Chapter we considered image formation for UWB SAR. We proposed a novel algorithm to address the two main issues that arise in UWB SAR. These issues are transmitter notching and RFI at the receiver. The proposed RFI-aware sparse image formation algorithm is an iterative algorithm which is based on techniques from CS. However, the proposed algorithm makes use of the estimated statistics of the RFI to improve the suppression of the interference. When the images are sparse, this algorithm will have close to optimal performance. Like linear filtering based methods, the RFI-aware sparse image formation algorithm does not assume that the RFI is very narrow band and therefore is applicable to many sources of RFI. The performance of the proposed algorithm was demonstrated to visually improve the image quality over linear filter based RFI suppression strategies and was also shown to produce images that had better target detection rates. It was also shown that sparsity based range compression algorithms will have

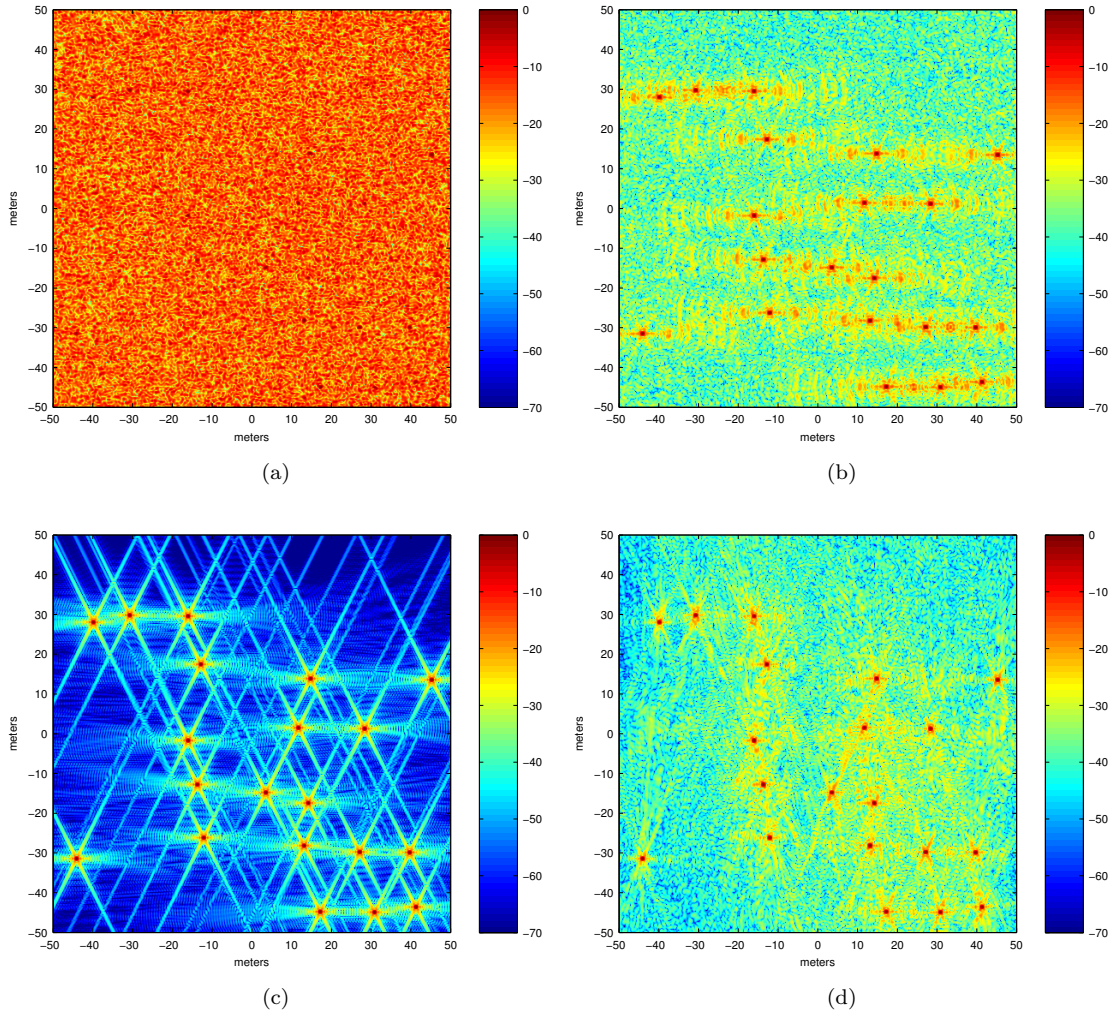


Figure 5.5: SAR images formed from simulated phase histories with RFI: (a) fast BP algorithm with no RFI suppression, (b) Wiener filtered followed by the BP algorithm, (c) RFI-aware sparse image formation and (d) range compression RFI-aware sparse image formation.

an inferior performance.

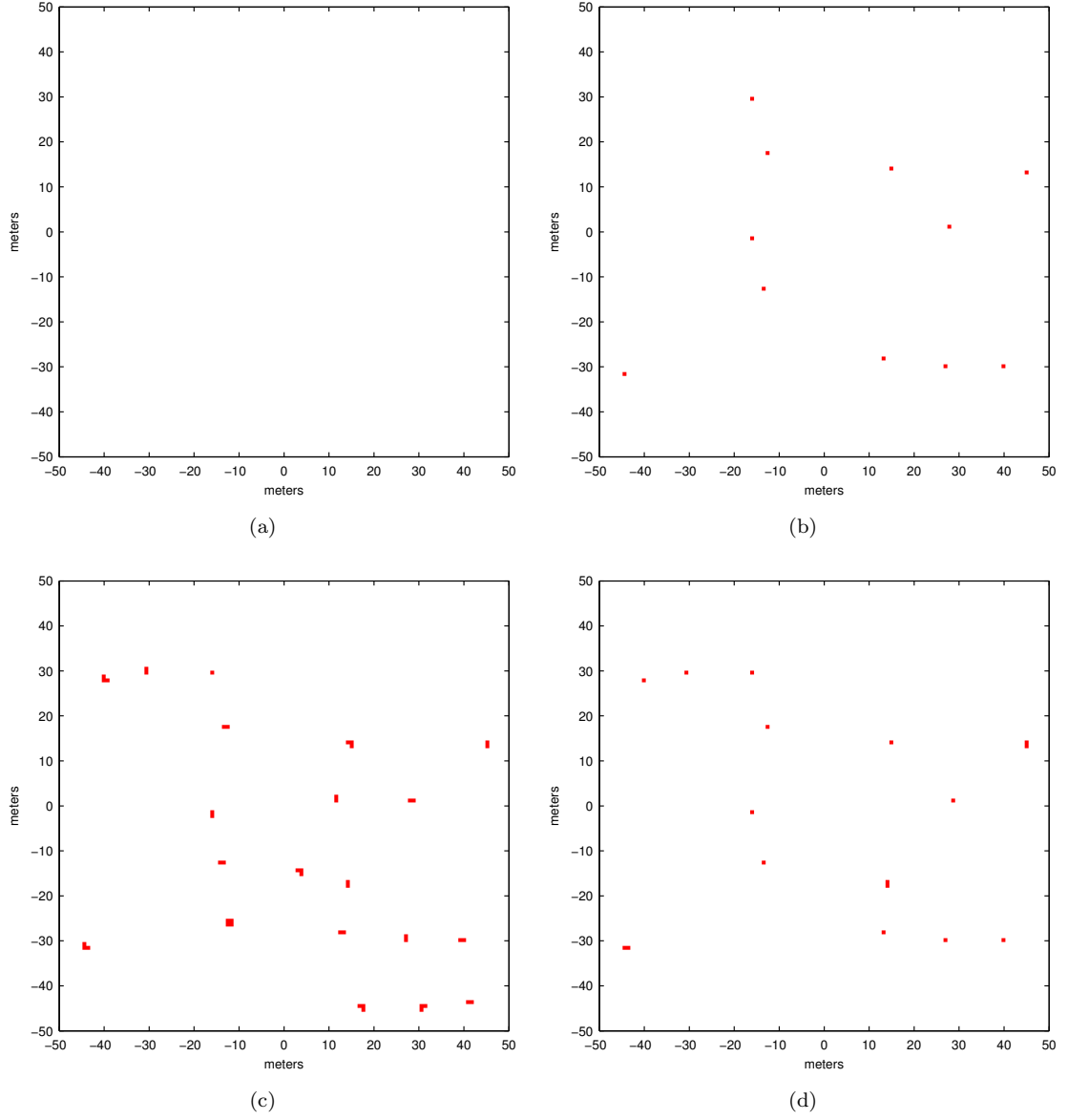


Figure 5.6: CFAR detections in red: (a) BP with no RFI suppression, (b) Wiener filtered followed BP, (c) RFI-aware sparse image formation, (d) range compression RFI-aware sparse image formation.

Chapter 6

Conclusion and Future Work

In this thesis we have investigated iterative image formation algorithms for SAR. Iterative algorithms approach SAR image formation as an inversion problem. This is in contrast with standard image formation algorithms, which approach the same problem from a matched filter perspective, which is not optimal.

Previous work on iterative algorithms have tended to use simplified observation models, in particular, models that make the far-field approximation. This is done to make their algorithms computationally feasible. However, to fully utilise the potential of iterative algorithms for real SAR systems, the observational models should be as close to the physical system as possible. Towards this goal, in Chap. 2 we developed a SAR model, starting from Maxwell's equations.

To incorporate the developed observation model into an iterative image formation framework, reduced complexity algorithms were used. These algorithms were based on the recently developed fast BP algorithms, including the fast decimation-in-image BP algorithm which was proposed in Chap. 2 of this thesis. These algorithms can be used to compute the observation model and its adjoint, which are required in an iterative algorithm, in an accurate manner with the same order of complexity as far-field algorithms. Unlike most other algorithms, these algorithms can incorporate many model features that are not normally included in iterative algorithms, they include: near-field scenes, non-linear apertures and non-flat scene terrain.

The developed fast RP and BP algorithms were used in Chap. 3 to create a versatile framework for iterative SAR image formation. This framework was used as a basis to address specific SAR imaging problems in the remainder of the thesis. The problems which were considered were selected because in these particular scenarios, standard image formation algorithms perform inadequately. The scenarios considered were: phase history undersampling, irregular sampling of a synthetic aperture, observational model errors and UWB SAR. All of the algorithms proposed, except for the algorithm proposed for irregular sampling, are developed by viewing SAR image formation as a SR problem. This essentially assumes that the SAR image is made up of sparse number of bright image elements and the rest of the image is lower amplitude

background image elements. By viewing the problem as a SR problem, many of the tools of CS can be used. These tools are based around iterative algorithms.

In Chap. 3, we solved a LS problem using a conjugate gradient algorithm to improve the image formation when the synthetic aperture is fully but irregularly sampled. We also consider image formation when there is undersampling in fast and slow time. To minimise the effects of the undersampling, we proposed forming the image in two parts. The first part, which contains the bright image elements, that are a result of specular reflection. The second part, which contains the background image elements. The background elements are the image elements that contain significant speckle noise. The image formation for the first image part was approached as a SR problem. Therefore, algorithms from the CS literature were used. Two algorithms were used for comparison, a greedy algorithm, IHT, and a convex relaxation algorithm FISTA. For the second part of the image, the fast BP algorithm was used. Using a publicly available SAR data set it was shown that the images formed using the proposed algorithms improved the visual image quality of the resulting images.

In Chap. 4, we considered the problem of errors in the observation model, in particular when there is phase history undersampling. In this scenario, the standard approach of applying an autofocus algorithm on the formed image was inappropriate. We instead proposed an iterative algorithm which approximated the solution to a non-convex ℓ_1 -norm regularised LS optimisation program. This algorithm, unlike standard methods, corrects model errors during image formation. Although non-convex, the algorithm is provably stable and convergent with a rate that is faster than existing algorithms.

In Chap. 5 we addressed the issues of RFI in UWB SAR. The two main issues, which occur due to RFI, are transmit notching and RFI at the receiver. Transmit notching occurs because spectral notches must be added to the chirp signal so the SAR system does not interfere with other users of the UWB spectrum. RFI at the receiver occurs because there are many other users in the UWB spectrum that will produce RFI at the receiver of the SAR system. We considered the transmit notching as undersampling of the phase history, while, the RFI at the receiver was treated as shaped noise. Using our model for both issues we proposed using an iterative algorithm which approximated the solution to a weighted LS with ℓ_1 -norm regularisation. The weighting was used to account for the spectral density of the RFI and the ℓ_1 -norm regularisation was added to improve the condition of the inversion problem which was deteriorated by the notching and RFI. The proposed algorithm was shown to have an improved image quality compared to existing linear filter based algorithms.

6.1 Recommendations and Future Work

With the increase in computing power and the development of fast algorithms for increasingly accurate SAR observation models, iterative algorithms will soon become feasible for image

formation in practical SAR systems. Using an iterative framework opens up the possibility of using SAR techniques for radar imaging in new and useful scenarios which could form the focus of future work. These scenarios include: three dimensional SAR imaging [20], long aperture SAR [130, 35, 95] and bistatic and multistatic SAR [47, 78, 121]. In these scenarios, standard image formation algorithms cannot address the particular peculiarity of the systems.

Three dimensional SAR imaging is challenging because a two dimensional synthetic aperture must be formed. Typically it is very hard to meet the sampling requirements of the second vertical dimension of the aperture. Iterative sparsity-based have been shown to resolve some of the issues but the research in this subject is still young [140].

When the synthetic aperture is long, the scattering response of a target is not constant over the entire aperture. This reduces the effective magnitude of a target formed using standard image formation methods. Iterative algorithms have been proposed which use a simplified model for the observation model and target scattering [130, 35]. A detailed study with more realistic models, would be of great interest.

In this thesis we only consider monostatic SAR, however, the proposed algorithms could be extended to the more general bistatic and multistatic cases. In these more general configurations, iterative algorithms may improve the image quality compared to standard image formation methods, in much the same way that iterative algorithms improved the image formation from irregularly sampled apertures in this thesis.

In this thesis we did not address the effects of undersampling on images effected by significant speckle. Some work has been undertaken to address a similar problem in holographic imaging [38]. The work involves taking a statistical perspective of the problem and aims to estimate the variance of the image elements effected by speckle. Statistical methods for estimating image elements effected by speckle has been consider for the fully sampled case [43].

There has been recent concern expressed in the radar community about modelling discrete SAR images as sparse [127]. This is because if we model the image as point targets, these points will not lie exactly on grid points. In the CS literature there has been work to devise algorithms that address this *off-the-grid* issue [122, 56]. Interestingly, in this thesis we have not found this to be a major issue. However, it is an area the surely warrants further research.

While this thesis has gone some of the way to reduce the complexity of iterative algorithms, there is further work to be done to develop these algorithms to a point were they can be used in practical system, potentially in real-time. One avenue of research towards this goal would be to consider speeding up the iteration of an algorithm as a whole rather than considering the observation model and its adjoint separately. For a model using a far-field approximation, a fast algorithm has been proposed which computes both at once [3]. A similar algorithm for the near-field would be extremely useful. Additionally, values that are repeatedly computed in the fast RP and BP algorithms could potential be computed once and stored in memory, which would trade redundant computation for an increased memory usage. Additional modification

to the fast RP and BP algorithms could be considered, which could provide similar speed ups but reduce errors due to the decimation. These algorithms could involve a mixed decimation-in-image and decimation-in-phase-history algorithm. Also, instead of using regular grids for decimation, alternative grids could be used such as Chebyshev grids, which were used in [44]. Additionally, parallel computing architectures such as Graphical Processing Units (GPU) could be used for additional speed up [113].

A related problem to SAR is synthetic aperture sonar (SAS). SAS is a relatively new technology, the first working system was only developed in the last ten years. SAS has adopted much of its techniques from SAR, including Fast BP algorithms [22, 74, 119]. Therefore, much of the work in this thesis could potentially be adopted for similar problems in SAS.

Appendix A

Synthetic Aperture Radar Simulator

In this appendix we will describe the simulator which was used extensively throughout this thesis to generate simulated phase histories. The simulator models a mono-static SAR system and can be used in most modes including spotlight, stripmap or scan. The simulator is based on the model of SAR developed in Chap. 2 and consists of two main components: a model of the SAR transmission and reception and a model of the SAR receiver.

A.1 Radio Frequency Transmission and Reception

The simulator models the relationship between the transmitted LFM chirp signal and the received back-scatter using a point target model. This relationship is parametrised by the values of the elements in Table A.1. Under this model, the transmitted signal is scattered isotropically by K point targets located in the scene. These K reflectors have an associated complex reflectivity. The reflected signal from each scatterer is model as a delayed version of the transmitted chirp, where the delay is given by $2 \|\vec{\mathbf{y}}_k - \vec{\mathbf{x}}_n\| / c_0$. In addition to this delay, the signal is also multiplied by the target reflectivity v_k and attenuated by $(4\pi \|\vec{\mathbf{y}}_k - \vec{\mathbf{x}}\|)^{-2}$. The model of the received signal is computed at the sample times t_m in fast-time, where,

$$t_m = F_t T_s (m - 1 - \lfloor M/2 \rfloor) / M, \quad (\text{A.1})$$

and $M = \lceil F_t F_f B T_s \rceil$. Therefore, the received signals at each of the specified positions along the synthetic aperture are computed as

Table A.1: Transmission and reception simulation parameters

parameter	description
f_0	carrier frequency
B	chirp bandwidth
T_s	chirp period
F_t	simulation time oversampling factor
F_f	simulation frequency oversampling factor
N	number of cross-range samples
$\{\bar{\mathbf{x}}_n\}_{n=1}^N$	cross-range locations
$\{\bar{\mathbf{y}}_{0n}\}_{n=1}^N$	dechirp centres
$\{\bar{\mathbf{y}}_{bn}\}_{n=1}^N$	antenna beam centres
Θ	antenna polar beamwidth
Φ	antenna azimuth beamwidth
K	number of targets
$\{\bar{\mathbf{y}}_k\}_{k=1}^K$	target locations
$\{v_k\}_{k=1}^K$	target reflectivities

Table A.2: Receiver simulation parameters

parameter	description
B_{IF}	intermediate frequency bandwidth
G_t	phase history time oversampling factor
G_f	phase history frequency oversampling factor

$$y_{mn} \leftarrow \sum_{k=1}^K \text{rect} \left(\frac{\phi(\bar{\mathbf{y}}_k - \bar{\mathbf{x}}_n) - \phi(y_b - \bar{\mathbf{x}}_n)}{\Phi/2} \right) \text{rect} \left(\frac{\theta(\bar{\mathbf{y}}_k - \bar{\mathbf{x}}_n) - \theta(y_b - \bar{\mathbf{x}}_n)}{\Theta/2} \right) \quad (\text{A.2})$$

$$(4\pi \|\bar{\mathbf{y}}_k - \bar{\mathbf{x}}_n\|)^{-2} \text{rect}((t_m - \tau_k)/T_s) s(t_m - \tau_k) v_k,$$

where, $\tau_{kn} = \frac{2u_{kn}}{c_0}$ is the delay to the scene centre and

$$s(t_m) = \text{rect}(t_m/T_s) \exp(j(2\pi f_0 t_m + \pi(B/T_s)t_m^2)) \quad (\text{A.3})$$

is the transmitted chirp.

A.2 Analogue Receiver

In the simulator we model an analogue dechirp-on-receive system. The system model of this type of receiver is parametrised by the values of three additional elements described in Table A.2. With these parameters specified, we can define the sample times t'_m in fast-time for the simulated phase histories as

$$t'_m = G_t T_s (m - 1 - \lfloor M'/2 \rfloor) / M', \quad (\text{A.4})$$

where, $M' = \lceil G_t G_f B T_s \rceil$. To model the dechirping that occurs in an analogue receiver, we

Table A.3: Notched LFM parameters

parameter	description
N_{notch}	number of notches
$\{f_{\text{notch } n}\}_{n=1}^{N_{\text{notch}}}$	notch centre frequencies
$\{B_{\text{notch } n}\}_{n=1}^{N_{\text{notch}}}$	notch bandwidths

compute

$$y_{mn} \leftarrow \text{Re} \left\{ y_{mn} \cos \left(-2\pi f_0 (t_m - \tau_{kn}) - \pi (B/T_s) (t_m - \tau_{kn})^2 \right) \right\} + j \text{Re} \left\{ y_{mn} \sin \left(-2\pi f_0 (t_m - \tau_{kn}) - \pi (B/T_s) (t_m - \tau_{kn})^2 \right) \right\}. \quad (\text{A.5})$$

The dechirped signals are then low-pass filtered in fast-time with the bandwidth specified by B_{IF} , to simulate an analog IF filter. The signal is also interpolated from the simulation fast-times t_m to the phase-history fast-times t'_m , which simulates a receiver ADC and produces the simulated sampled phase history.

Finally, the phase is deskewed by first taking a DFT of the phase history in the fast-time and then by multiplying by a quadratic phase term $\exp \left(-j \frac{\pi T_s f_m^2}{B} \right)$, where $f_m = (m - 1 - \lfloor M'/2 \rfloor) / G_t T_s$ and finally by taking a IDFT.

A.3 Timing Errors

In Chap. 4, timing errors in the SAR observational model are investigated. To model the timing errors in the simulator, specified timing errors τ_{en} are introduced into the simulated received signals in Eq. (A.2). This is achieved by defining $t_m = \tau_{en} + F_t T_s (m - 1 - \lfloor M/2 \rfloor) / M$ in Eq. (A.2).

A.4 Notched Linear Frequency Modulated Chirp

In Chap. 4 and Chap. 5 we investigate the image formation performance of algorithms when the transmitted signal is a notched LFM chirp. To simulate spectral notching of a transmitted LFM chirp, the model of the transmitted signal in Eq.(A.3) is modified. In the simulator, notching is parametrised by the value of the elements in Table A.3. Using these parameters the transmitted chirp is modelled as

$$s(t_m) = \text{rect}(t_m/T_s) \exp(j(2\pi f_0 t_m + \pi(B/T_s)t_m^2)) - \sum_{n=1}^{N_{\text{notch}}} N_n(t_m), \quad (\text{A.6})$$

where,

$$N_n(t) = \int \sqrt{\frac{j\pi}{\alpha}} \text{rect}\left(\frac{\omega - 2\pi f_{\text{notch } n}}{2\pi B_{\text{notch } n}}\right) \exp(j\omega t) d\omega \quad (\text{A.7})$$

Table A.4: RFI parameters

parameter	description
N_{intf}	number of interferers
$\{f_{\text{intf}_n}\}_{n=1}^{N_{\text{intf}}}$	interferers' centre frequencies
$\{T_{\text{intf}_n}\}_{n=1}^{N_{\text{intf}}}$	interferers' window length
$\{P_{\text{intf}_n}\}_{n=1}^{N_{\text{intf}}}$	interferers' power
P_n	white noise power

A.5 Radio Frequency Interference

In Chap. 5 we investigate RFI at the receiver of a SAR system. To simulate receiver RFI, we add RFI to the simulated received signal in Eq. (A.2). In the simulator, RFI is parametrised by the values of the elements in Table A.4. Using these parameters, we first computed the PSD of the simulated RFI. This PSD is computed by

$$S_{\text{intf}}(\omega) = \sum_{n=1}^{N_{\text{intf}}} P_{\text{intf}_n} \text{sinc}^2(\pi T_{\text{intf}_n}(\omega - 2\pi f_{\text{intf}_n})) + P_n. \quad (\text{A.8})$$

Each RFI signal is then simulated as

$$s_{\text{intf}}(t) = \int S_{\text{intf}}(\omega) W(\omega) \exp(j\omega t) d\omega \quad (\text{A.9})$$

where, $W(\omega)$ is a Fourier transform of an instance of a unit variance circularly-symmetric complex Gaussian time series.

A.6 Limitations of the Simulation

The simulator used within this thesis models a real SAR system with enough accuracy to provide interesting insight into the performance of the developed algorithm. However, it also has some obvious limitations. A list of the most important limitations are given below.

- *Point target simulator.* Targets are modelled as points and therefore more complex target models are not used.
- *Speckle Targets.* The simulator does not model speckle. Background image elements that are effected by speckle would usually makes up a large component of real SAR images.
- *Constant reflectivity targets.* The model of the targets does not model reflectivity fluctuation. Also, the reflectivity of a target is not dependent on frequency or viewing angle.
- *Antenna beam pattern.* The antenna is modelled as having an ideal constant gain directional beam pattern that does not change with frequency.

Bibliography

- [1] K. Abend and J.W. McCorkle, *Radio and TV interference extraction for ultrawideband radar*, Proc. SPIE, vol. 2487, Apr. 1995, pp. 119–129.
- [2] M. Aharon, M. Elad, and A.M. Bruckstein, *On the uniqueness of overcomplete dictionaries, and a practical way to retrieve them*, J. Linear Algebra Appl. **416** (2006), no. 1, 48–67.
- [3] R. Ahmad, C.D. Austin, and L.C. Potter, *Toeplitz embedding for fast iterative regularized imaging*, Proc. SPIE, vol. 8051, May 2011.
- [4] F. Andersson, R. Moses, and F. Natterer, *Fast Fourier methods for synthetic aperture radar imaging*, IEEE Trans. Aerosp. Electron. Syst. **48** (2012), no. 1, 215–229.
- [5] L.E. Andersson, *On the determination of a function from spherical averages*, SIAM J. Math. Anal. **19** (1988), no. 1, 214–232.
- [6] C.D. Austin, R.L. Moses, J.N. Ash, and E. Ertin, *On the relation between sparse reconstruction and parameter estimation with model order selection*, IEEE Trans. Signal Processing **4** (2010), no. 3, 560–570.
- [7] R. Baraniuk, M. Davenport, R. DeVore, and M. Wakin, *A simple proof of the restricted isometry property for random matrices*, Constr. Approx. **28** (2008), no. 3, 253–263.
- [8] R. Baraniuk and P. Steeghs, *Compressive radar imaging*, Proc. IEEE Radar Conf., Apr. 2007, pp. 128–133.
- [9] J. Barzilai and J.M. Borwein, *Two-point step size gradient methods*, IMA J. Numer. Anal. **8** (1988), no. 1, 141–148.
- [10] S. Basu and Y. Bresler, *$O(N^2 \log_2 N)$ filtered backprojection reconstruction algorithm for tomography*, IEEE Trans. Image Processing **9** (2000), no. 10, 1760–1773.
- [11] O. Batu and M. Cetin, *Parameter selection in sparsity-driven SAR imaging*, IEEE Trans. Aerosp. Electron. Syst. **47** (2011), no. 4, 3040–3050.

- [12] A. Beck and M. Teboulle, *A fast iterative shrinkage-thresholding algorithm for linear inverse problems*, SIAM J. Imag. Sci. **2** (2009), no. 1, 183–202.
- [13] S. Becker, J. Bobin, and E.J. Candes, *NESTA: A fast and accurate first-order method for sparse recovery*, SIAM J. Imag. Sci. **4** (2011), no. 1, 1–39.
- [14] S Bhattacharya, T Blumensath, B Mulgrew, and M Davies, *Fast encoding of synthetic aperture radar raw data using compressed sensing*, Proc. IEEE Workshop Stat. Signal Processing, Aug. 2007.
- [15] E.G. Birgin, J.M. Martinez, and M. Raydan, *Nonmonotone spectral projected gradient methods on convex sets*, SIAM J. Optim. **10** (2000), no. 4, 1196–1211.
- [16] T. Blumensath and M.E. Davies, *Iterative hard thresholding for compressed sensing*, Appl. Comp. Harm. Anal. **27** (2009), no. 3, 265–274.
- [17] ———, *Normalized iterative hard thresholding: Guaranteed stability and performance*, IEEE J. Select. Topics Signal Processing **4** (2010), no. 2, 298–309.
- [18] A. Boag, Y. Bresler, and E. Michielssen, *A multilevel domain decomposition algorithm for fast $O(N^2 \log N)$ reprojection of tomographic images*, IEEE Trans. Image Processing **9** (2000), no. 9, 1573–1582.
- [19] W.M. Brown and C.J. Palermo, *Theory of coherent systems*, IRE Trans. Mil. Electron. **MIL-6** (1962), no. 2, 187–196.
- [20] A. Budillon, A. Evangelista, and G. Schirinzi, *Three-dimensional SAR focusing from multipass signals using compressive sampling*, IEEE Trans. Geosci. Remote Sensing **49** (2011), no. 1, 488–499.
- [21] C. Cafforio, C. Prati, and F. Rocca, *SAR data focusing using seismic migration techniques*, IEEE Trans. Aerosp. Electron. Syst. **27** (1991), no. 2, 194–207.
- [22] H.J. Callow, R.E. Hansen, and T.O. Saeboe, *Effect of approximations in fast factorized backprojection in synthetic aperture imaging of spot regions*, Proc. Oceans Conf., Sept. 2006, pp. 1–6.
- [23] E.J. Candes, *The restricted isometry property and its implications for compressed sensing*, Theory Signals/Math. Anal. **346** (2008), no. 9–10, 589–592.
- [24] E.J. Candes, J.K. Romberg, and T. Tao, *Robust uncertainty principles: Exact signal reconstruction from highly incomplete frequency information*, IEEE Trans. Inform. Theory **52** (2006), no. 2, 489–509.
- [25] ———, *Stable signal recovery from incomplete and inaccurate measurements*, Commun. Pure Appl. Math. **59** (2006), no. 8, 1207–1223.

- [26] E.J. Candes, T. Strohmer, and V. Voroninski, *Phaselift: Exact and stable signal recovery from magnitude measurements via convex programming*, Commun. Pure, Applied Math. **66** (2013), no. 8, 1241–1274.
- [27] E.J. Candes and T. Tao, *Near-optimal signal recovery from random projections: Universal encoding strategies?*, IEEE Trans. Inform. Theory **52** (2006), no. 12, 5406–5425.
- [28] E.J. Candes and M.B. Wakin, *An introduction to compressive sampling*, IEEE Signal Processing Mag. **25** (2008), no. 2, 21–30.
- [29] W.G. Carrara, R.S. Goodman, and R.M. Majewski, *Spotlight-mode synthetic aperture radar: signal processing algorithms*, 1 ed., Artech House, 1995.
- [30] C.H. Casteel Jr, L.A. Gorham, M.J. Minardi, S.M. Scarborough, K.D. Naidu, and U.K. Majumder, *A challenge problem for 2D/3D imaging of targets from a volumetric data set in an urban environment*, Proc. SPIE, vol. 6568, Apr. 2007.
- [31] M. Cetin, *Feature-enhanced synthetic aperture radar imaging*, Ph.D. thesis, Boston University, College of Engineering, 2001.
- [32] M. Cetin and W.C. Karl, *Feature-enhanced synthetic aperture radar image formation based on nonquadratic regularization*, IEEE Trans. Image Processing **10** (2001), no. 4, 623–631.
- [33] M. Cetin, W.C. Karl, and D.A. Castanon, *Feature enhancement and ATR performance using nonquadratic optimization-based SAR imaging*, IEEE Trans. Aerosp. Electron. Syst. **39** (2003), no. 4, 1375–1395.
- [34] M. Cetin and R.L. Moses, *SAR imaging from partial-aperture data with frequency-band omissions*, Proc. SPIE, vol. 5805, Apr. 2005.
- [35] R.D. Chaney, A.S. Willsky, and L.M. Novak, *Coherent aspect-dependent SAR image formation*, Proc. SPIE, vol. 2230, Jun. 1994.
- [36] M. Cheney, *A mathematical tutorial on synteheic aperture radar*, SIAM Rev. **43** (2001), no. 2, 301–312.
- [37] M. Cheney and B. Borden, *Fundamentals of radar imaging*, vol. 79, SIAM, 2009.
- [38] K. Choi, R. Horisaki, J. Hahn, S. Lim, D.L. Marks, T.J. Schulz, and D.J. Brady, *Compressive holography of diffuse objects*, Appl. Opt. **49** (2010), no. 34, H1–H10.
- [39] A. Cohen, W. Dahmen, and R. DeVore, *Compressed sensing and best k -term approximation*, J. Amer. Math. Soc. **22** (2009), 211–231.

- [40] W. Dai and O. Milenkovic, *Subspace pursuit for compressive sensing signal reconstruction*, IEEE Trans. Inform. Theory **55** (2009), no. 5, 2230–2249.
- [41] I. Daubechies, M. Defrise, and C. De Mol, *An iterative thresholding algorithm for linear inverse problems with a sparsity constraint*, Commun. Pure Appl. Math. **57** (2004), no. 11, 1413–1457.
- [42] M.E. Davis, *Foliage penetration radar*, 1 ed., SciTech Publishing, 2011.
- [43] S.R. DeGraaf, *SAR imaging via modern 2-D spectral estimation methods*, IEEE Trans. Image Processing **7** (1998), no. 5, 729–761.
- [44] L. Demanet, M. Ferrara, N. Maxwell, J. Poulson, and L. Ying, *A butterfly algorithm for synthetic aperture radar imaging*, SIAM J. Imag. Sci. **5** (2012), no. 1, 203–243.
- [45] L Demanet and P. Hand, *Stable optimizationless recovery from phaseless linear measurements*, (2013), preprint, [arXiv:1208.1803\[math.NA\]](https://arxiv.org/abs/1208.1803).
- [46] R.A. DeVore, *Nonlinear approximation*, Acta Numer. **7** (1998), 51–150.
- [47] Y. Ding and D.C. Munson Jr., *A fast back-projection algorithm for bistatic SAR imaging*, Proc. IEEE Conf. Image Process., vol. 2, Sept. 2002, pp. 449–452.
- [48] A.W. Doerry, F.M. Dickey, and L.A. Romero, *Windowing functions for SAR data with spectral gaps*, Proc. SPIE, vol. 5095, Apr. 2003, pp. 54–65.
- [49] Y. Dong, B. Forster, and C. Ticehurst, *Radar backscatter analysis for urban environments*, Int. J. Remote Sensing **18** (1997), no. 6, 1351–1364.
- [50] D.L. Donoho, *Compressed sensing*, IEEE Trans. Inform. Theory **52** (2006), no. 4, 1289–1306.
- [51] D.L. Donoho and M. Elad, *Optimally sparse representation in general (nonorthogonal) dictionaries via ℓ_1 minimization*, Proc. Natl. Acad. Sci. **100** (2003), no. 5, 2197–2202.
- [52] D.L. Donoho, Y. Tsaig, I. Drori, and J.-L. Starck, *Sparse solution of underdetermined linear equations by stagewise orthogonal matching pursuit*, IEEE Trans. Inform. Theory **58** (2012), no. 2, 1094–1121.
- [53] J. Duchi, S. Shalev-Shwartz, Y. Singer, and T. Chandra, *Efficient projections onto the ℓ_1 -ball for learning in high dimensions*, Proc. ICML, Jul. 2008, pp. 272–279.
- [54] A. Dutt and V. Rokhlin, *Fast Fourier transforms for nonequispaced data*, SIAM J. Sci. Comput. **16** (1993), no. 6, 1368–1393.
- [55] ———, *Fast Fourier transforms for nonequispaced data, ii*, Appl. Comp. Harm. Anal. **2** (1995), no. 1, 85–100.

- [56] C. Ekanadham, D. Tranchina, and E.P. Simoncelli, *Recovery of sparse translation-invariant signals with continuous basis pursuit*, IEEE Trans. Signal Processing **59** (2011), no. 10, 4735–4744.
- [57] Y.C. Eldar and G. Kutyniok, *Compressed sensing: Theory and applications*, 1 ed., Cambridge University Press, 2012.
- [58] J. Ender, *A brief review of compressive sensing applied to radar*, Proc. Int. Radar Symposium, vol. 1, Jun. 2013, pp. 3–16.
- [59] J.H.G. Ender, *On compressive sensing applied to radar*, Signal Process. **90** (2010), no. 5, 1402–1414.
- [60] J.A. Fawcett, *Inversion of N-dimensional spherical averages*, SIAM J. Appl. Math. **45** (1985), no. 2, 336–341.
- [61] M. Ferrara, J.A. Jackson, and C. Austin, *Enhancement of multi-pass 3D circular SAR images using sparse reconstruction techniques*, Proc. SPIE, vol. 7337, Apr. 2009.
- [62] J.A. Fessler and B.P. Sutton, *Nonuniform fast Fourier transforms using min-max interpolation*, IEEE Trans. Signal Processing **51** (2003), no. 2, 560–574.
- [63] M.A.T. Figueiredo, R.D. Nowak, and S.J. Wright, *Gradient projection for sparse reconstruction: Application to compressed sensing and other inverse problems*, IEEE J. Sel. Topics Signal Process. **1** (2007), no. 4, 586–597.
- [64] S. Foucart, *Sparse recovery algorithms: sufficient conditions in terms of restricted isometry constants*, Springer Proc. Math., vol. 13, Mar. 2010, pp. 65–77.
- [65] P.-O. Frolind and L. M H Ulander, *Evaluation of angular interpolation kernels in fast back-projection SAR processing*, IEE Proc. Radar, Sonar, Navig. **153** (2006), no. 3, 243–249.
- [66] A. Golden Jr, S.A. Werness, M.A. Stuff, S.R. DeGraaf, and R.C. Sullivan Jr, *Radio frequency interference removal in a VHF/UHF deramp SAR*, Proc. SPIE, vol. 2487, Apr. 1995, pp. 84–95.
- [67] G.H. Golub and C.F. Van Loan, *Matrix computations*, 3 ed., The Johns Hopkins University Press, 1996.
- [68] L. Greengard and J-Y. Lee, *Accelerating the nonuniform fast Fourier transform*, SIAM Rev. **46** (2004), no. 3, 443–454.
- [69] L. Greengard and V. Rokhlin, *A fast algorithm for particle simulations*, J. Comput. Phys. **73** (1987), no. 2, 325–348.

- [70] E.T. Hale, W. Yin, and Y. Zhang, *Tr07-07: A fixed-point continuation method for ℓ_1 -regularized minimization with applications to compressed sensing*, Tech. report, Rice University, 2007.
- [71] H. Hellsten and L.E. Andersson, *An inverse method for the processing of synthetic aperture radar data*, Inverse Probl. **3** (1987), no. 1, 111–124.
- [72] H. Hellsten, L.M. Ulander, A. Gustavsson, and B. Larsson, *Development of VHF CARABAS II SAR*, Proc. SPIE, vol. 2747, Apr. 1996, pp. 48–60.
- [73] M.A. Herman and T. Strohmer, *High-resolution radar via compressed sensing*, IEEE Trans. Signal Processing **57** (2009), no. 6, 2275–2284.
- [74] A. J. Hunter, M. Hayes, and P. Gough, *A comparison of fast factorised back-projection and wavenumber algorithms for SAS image reconstruction*, Proc. World Congr. Ultrason., 2003, pp. 527–530.
- [75] C.V. Jakowatz Jr and D.E. Wahl, *Eigenvector method for maximum-likelihood estimation of phase errors in synthetic-aperture-radar imagery*, J. Opt. Soc. Am. A **10** (1993), no. 12, 2539–2546.
- [76] C.V. Jakowatz Jr, D.E. Wahl, P.H. Eichel, D.C. Ghiglia, and P.A. Thompson, *Spotlight-mode synthetic aperture radar: a signal processing approach*, 4 ed., Kluwer Academic Publishers, 1999.
- [77] C.V. Jakowatz Jr, D.E. Wahl, and D.A. Yocky, *Beamforming as a foundation for spotlight-mode SAR image formation by backprojection*, Proc. SPIE, vol. 6970, Apr. 2008.
- [78] ———, *A beamforming algorithm for bistatic SAR image formation*, Proc. SPIE, vol. 7699, Apr. 2010.
- [79] S.I. Kelly and M.E. Davies, *RFI suppression and sparse image formation for UWB SAR*, Proc. Int. Radar Symposium, vol. 2, Jun. 2013, pp. 655–660.
- [80] S.I. Kelly, C. Du, G. Rilling, and M.E. Davies, *Advanced image formation and processing of partial synthetic aperture radar data*, IET Signal Processing **6** (2012), no. 5, 511–520.
- [81] S.I. Kelly, G. Rilling, M.E. Davies, and B. Mulgrew, *Iterative image formation using fast (re/back)-projection for spotlight-mode SAR*, Proc. IEEE Radar Conf., May 2011, pp. 835–840.
- [82] S.I. Kelly, M. Yaghoobi, and M.E. Davies, *Sparsity-based autofocus for under-sampled synthetic aperture radar*, IEEE Trans. Aerosp. Electron. Syst. (2013), to appear.
- [83] T.J. Kragh and A.A. Kharbouch, *Monotonic iterative algorithms for SAR image restoration*, Proc. IEEE Conf. Image Process., Oct. 2011, pp. 645–648.

- [84] L. Kuang-Hung, A. Wiesel, and D.C. Munson Jr, *Synthetic aperture radar autofocus based on a bilinear model*, IEEE Trans. Image Processing **21** (2012), no. 5, 2735–2746.
- [85] X. Li and V. Voroninski, *Sparse signal recovery from quadratic measurements via convex programming*, (2012), preprint, [arXiv:1209.4785\[cs.IT\]](#).
- [86] R.T. Lord and M.R. Inggs, *Efficient RFI suppression in SAR using LMS adaptive filter integrated with range/doppler algorithm*, Electron. Lett. **35** (1999), no. 8, 629–630.
- [87] X. Luo, L.M.H. Ulander, J. Askne, G. Smith, and P.-O. Frolind, *RFI suppression in ultra-wideband SAR systems using LMS filters in frequency domain*, Electron. Lett. **37** (2001), no. 4, 241–243.
- [88] S.G. Mallat and Z. Zhang, *Matching pursuits with time-frequency dictionaries*, IEEE Trans. Signal Processing **41** (1993), no. 12, 3397–3415.
- [89] J.W. McCorkle and M. Rofheart, *Order $N^2 \log(N)$ backprojector algorithm for focusing wide-angle wide-bandwidth arbitrary-motion synthetic aperture radar*, Proc. SPIE, vol. 2747, Apr. 1996, pp. 25–36.
- [90] S. Mendelson, A. Pajor, and N. Tomczak-Jaegermann, *Uniform uncertainty principle for Bernoulli and subgaussian ensembles*, Constr. Approx. **28** (2008), no. 3, 277–289.
- [91] T. Miller and J. McCorkle, *RFI suppression for ultra wideband radar*, IEEE Trans. Aerosp. Electron. Syst. **33** (1997), no. 4, 1142–1156.
- [92] T.R. Miller, J.W. McCorkle, and L.C. Potter, *Near-least-squares radio frequency interference suppression*, Proc. SPIE, vol. 2487, Apr. 1995, pp. 72–83.
- [93] A.S. Milman, *SAR imaging by ω - k migration*, Int. J. Remote Sensing **14** (1993), no. 10, 1965–1979.
- [94] R.L. Morrison Jr, M.N. Do, and D.C. Munson Jr, *MCA: A multichannel approach to SAR autofocus*, IEEE Trans. Image Processing **18** (2009), no. 4, 840–853.
- [95] R.L. Moses, L.C. Potter, and M. Cetin, *Wide-angle SAR imaging*, Proc. SPIE, vol. 5427, Sept. 2004.
- [96] D.C. Munson Jr., J.D. O’Brien, and W. Jenkins, *A tomographic formulation of spotlight-mode synthetic aperture radar*, Proc. IEEE **71** (1983), no. 8, 917–925.
- [97] D.C. Munson Jr. and R.L. Visentin, *A signal processing view of strip-mapping synthetic aperture radar*, IEEE Trans. Acoust., Speech, Signal Processing **37** (1989), no. 12, 2131–2147.

- [98] Y. Na, H. Sun, Y.H. Lee, and L.C. Tai, *Performance evaluation of back-projection and range migration algorithms in foliage penetration radar imaging*, Proc. IEEE Conf. Image Process., vol. 1, Oct. 2004, pp. 21–24.
- [99] F. Natterer, *The mathematics of computerized tomography*, 1 ed., SIAM, 2001.
- [100] D. Needell and J.A. Tropp, *Cosamp: iterative signal recovery from incomplete and inaccurate samples*, Commun. ACM **53** (2010), no. 12, 93–100.
- [101] D. Needell and R. Vershynin, *Signal recovery from incomplete and inaccurate measurements via regularized orthogonal matching pursuit*, IEEE J. Select. Topics Signal Processing **4** (2010), no. 2, 310–316.
- [102] L. Nguyen and T. Do, *Recovery of missing spectral information in ultra-wideband synthetic aperture radar (SAR) data*, Proc. IEEE Radar Conf., May 2012, pp. 0253–0256.
- [103] L.H. Nguyen and T.D. Tran, *Robust and adaptive extraction of RFI signals from ultra-wideband radar data*, Proc. IEEE Geosci. Remote Sensing Conf., Jul. 2012, pp. 7137–7140.
- [104] S. Nilsson and L.E. Andersson, *Application of fast back-projection techniques for some inverse problems of synthetic aperture radar*, Proc. SPIE, vol. 3370, Apr. 1998, pp. 62–72.
- [105] M.O. Onhon and M. Cetin, *A nonquadratic regularization-based technique for joint SAR imaging and model error correction*, Proc. SPIE, vol. 7337, Apr. 2009.
- [106] N.O. Onhon and M. Cetin, *A sparsity-driven approach for joint SAR imaging and phase error correction*, IEEE Trans. Image Processing **21** (2012), no. 4, 2075–2088.
- [107] V.M. Patel, G. R. Easley, D.M. Healy, and R. Chellappa, *Compressed synthetic aperture radar*, IEEE J. Sel. Topics Signal Process. **4** (2010), no. 2, 244–254.
- [108] L.C. Potter, E. Ertin, J.T. Parker, and M. Cetin, *Sparsity and compressed sensing in radar imaging*, Proc. IEEE **98** (2010), no. 6, 1006–1020.
- [109] R.K. Raney, H. Runge, R. Bamler, I.G. Cumming, and F.H. Wong, *Precision SAR processing using chirp scaling*, IEEE Trans. Geosci. Remote Sensing **32** (1994), no. 4, 786–799.
- [110] G. Rilling, M.E. Davies, and B. Mulgrew, *Compressed sensing based compression of SAR raw data*, Proc. SPARS, Apr. 2009.
- [111] G. Rilling, C. Du, M.E. Davies, and B. Mulgrew, *Processing SAR data with gaps in the aperture: A compressed sensing perspective*, Proc. Inst. Acoust., vol. 32, Sept. 2010, pp. 62–67.
- [112] F. Rocca, C. Caffori, and C. Prati, *Synthetic aperture radar: A new application for wave equation techniques*, Geophys. Prospecting **37** (1989), no. 7, 809–830.

- [113] A. Rogan and R. Carande, *Improving the fast back projection algorithm through massive parallelizations*, Proc. SPIE, vol. 7669, Apr. 2010.
- [114] J. Romberg, *Imaging via compressive sampling*, IEEE Signal Processing Mag. **25** (2008), no. 2, 14–20.
- [115] M. Rudelson and R. Vershynin, *On sparse reconstruction from Fourier and Gaussian measurements*, Comm. Pure Appl. Math. **61** (2008), no. 8, 1025–1045.
- [116] J. Salzman, D. Akamine, R. Lefevre, and J.C. Kirk Jr., *Interrupted synthetic aperture radar (SAR)*, Proc. IEEE Radar Conf., May 2001, pp. 117–122.
- [117] D.R. Sheen, N.L. VandenBerg, S.J. Shackman, D.L. Wiseman, L.P. Elenbogen, and R.F. Rawson, *P-3 ultra-wideband SAR: description and examples*, IEEE Aerosp. Electron. Syst. Mag. **11** (1996), no. 11, 25–30.
- [118] C.W. Sherwin, J.P. Ruina, and R.D. Rawcliffe, *Some early developments in synthetic aperture radar systems*, IRE Trans. Mil. Electron. **MIL-6** (1962), no. 2, 111–115.
- [119] G. Shippey, S. Banks, and J. Pihl, *SAS image reconstruction using fast polar back projection: comparisons with fast factored back projection and Fourier-domain imaging*, Proc. Oceans Conf., vol. 1, Jun. 2005, pp. 96–101.
- [120] M. Soumekh, *Synthetic aperture radar signal processing with MATLAB algorithms*, 1 ed., John Wiley & Sons, 1999.
- [121] I. Stojanovic, W.C. Karl, and M Cetin, *Compressed sensing of mono-static and multi-static SAR*, Proc. SPIE, vol. 7337, Apr. 2009.
- [122] G. Tang, B.N. Bhaskar, P. Shah, and B. Recht, *Compressed sensing off the grid*, (2013), preprint, [arXiv:1207.6053\[cs.IT\]](https://arxiv.org/abs/1207.6053).
- [123] K. Theodore and L.A. Lovas, *RF interference suppression in ultrawideband radar receivers*, Proc. SPIE, vol. 2487, Apr. 1995, pp. 107–118.
- [124] R.J.A. Tough, K.D. Ward, and P.W. Shepherd, *Modelling and enhancement of interrupted synthetic aperture radar imagery*, Radar Sonar Navig. **1** (2007), no. 6, 407–413.
- [125] J.A. Tropp, *Greed is good: Algorithmic results for sparse approximation*, IEEE Trans. Inform. Theory **50** (2004), no. 10, 2231–2242.
- [126] J.A. Tropp and A.C. Gilbert, *Signal recovery from random measurements via orthogonal matching pursuit*, IEEE Trans. Inform. Theory **53** (2007), no. 12, 4655–4666.
- [127] S. Ugur, O. Arikan, and A.C. Gurbuz, *Off-grid sparse SAR image reconstruction by EMMP algorithm*, Proc. IEEE Radar Conf., May 2013, pp. 1–4.

- [128] L.M.H. Ulander, H. Hellsten, and G. Stenstrom, *Synthetic-aperture radar processing using fast factorized back-projection*, IEEE Trans. Aerosp. Electron. Syst. **39** (2003), no. 3, 760–776.
- [129] E. van den Berg and M. P. Friedlander, *Probing the Pareto frontier for basis pursuit solutions*, SIAM J. Sci. Comput. **31** (2008), no. 2, 890–912.
- [130] K.R. Varshney, M. Cetin, J.W. Fisher, and A.S. Willsky, *Sparse representation in structured dictionaries with application to synthetic aperture radar*, IEEE Trans. Signal Processing **56** (2008), no. 8, 3548–3561.
- [131] D. Vu, L. Xu, M. Xue, and J. Li, *Nonparametric missing sample spectral analysis and its applications to interrupted SAR*, IEEE J. Sel. Topics Signal Process. **6** (2012), no. 1, 1–14.
- [132] D.E. Wahl, P.H. Eichel, D.C. Ghiglia, and C.V. Jakowatz Jr, *Phase gradient autofocus – a robust tool for high resolution SAR phase correction*, IEEE Trans. Aerosp. Electron. Syst. **30** (1994), no. 3, 827–835.
- [133] D.E. Wahl, D.A. Yocky, and C.V. Jakowatz Jr, *An implementation of a fast backprojection image formation algorithm for spotlight-mode SAR*, Proc. SPIE, vol. 6970, Apr. 2008.
- [134] J.L. Walker, *Range-doppler imaging of rotating objects*, IEEE Trans. Aerosp. Electron. Syst. **AES-16** (1980), no. 1, 23–52.
- [135] L. Welch, *Lower bounds on the maximum cross correlation of signals*, IEEE Trans. Inform. Theory **20** (1974), no. 3, 397–399.
- [136] S. Xiao, D.C. Munson Jr, S. Basu, and Y. Bresler, *An $N^2 \log N$ back-projection algorithm for SAR image formation*, Proc. Asilomar Conf. Signals, Syst., Comp., vol. 1, Oct. 2000, pp. 3–7.
- [137] M. Yaghoobi, T. Blumensath, and M.E. Davies, *Dictionary learning for sparse approximations with the majorization method*, IEEE Trans. Signal Processing **57** (2009), no. 6, 2178–2191.
- [138] A.F. Yegulalp, *Fast backprojection algorithm for synthetic aperture radar*, Proc. IEEE Radar Conf., Apr. 1999, pp. 60–65.
- [139] W. Yin, S. Osher, D. Goldfarb, and J. Darbon, *Bregman iterative algorithms for ℓ_1 -minimization with applications to compressed sensing*, SIAM J. Imag. Sci. **1** (2008), no. 1, 143–168.

- [140] R. Zhu, X.X. Bamler, *Tomographic SAR inversion by ℓ_1 -norm regularization – the compressive sensing approach*, IEEE Trans. Geosci. Remote Sensing **48** (2010), no. 10, 3839–3846.